A FUNDAMENTAL STUDY OF HOT CORROSION AND INTERDIFFUSION OF CHROMIUM, ALUMINUM, AND SILICON COATINGS ON A NICKEL-201 SUBSTRATE

by

Zachery Edward Gill

A thesis submitted in partial fulfillment
of the requirements for the degree

of

Master of Science

in

Chemical Engineering

MONTANA STATE UNIVERSITY
Bozeman, Montana

May, 2014

TABLE OF CONTENTS

TABLE OF CONTENTS - CONTINUED

LIST OF TABLES

Table Page

LIST OF FIGURES

Figure Page

LIST OF FIGURES – CONTINUED

Figure Page

LIST OF FIGURES – CONTINUED

Figure Page

LIST OF FIGURES – CONTINUED

Figure Page

LIST OF FIGURES – CONTINUED

Figure Page

LIST OF FIGURES – CONTINUED

Figure Page

NOMENCLATURE

Kroger-Vink notation

Some departure from the typical Kroger-Vink notation is used in the document. The significant deviations are described in the following table.

Table 1: Deviations in notation from Kroger-Vink

Type of Defect	Kroger-Vink Notation Symbol	Alternative Used
Metal Vacancy	V_M''	V_M^{2+}
Oxygen Vacancy	$V_O^{\cdot\cdot}$	V_O^{2+}
Free Electon	e'	e^-
Hydronium Ion	$h^{\cdot}$	h^+

Sample Identification

Uncoated samples are described “as received” (AR) for example uncoated Ni-201 (Ni) is described: ARNi. Conversely, coated samples are described according to the convention of underlying metal + coating element. For example, a Ni-201 sample coupon coated with aluminum (Al) is described: Ni + Al.

ABSTRACT

Modern turbine engine systems require increased efficiency and durability. To achieve these goals, high-temperature materials with high-strength, low-cost and non-strategic compositions are needed. In advanced turbine applications, combustor liners, blades and vanes are exposed to corrosive combustion byproducts, such as alkali salts, at temperatures up to ~1700°C, with high gas velocities, entrained particulates, and other foreign objects at pressures of up to 3 MPa (30 atm). These extreme conditions can drive a dangerous phenomenon known as "hot corrosion", an accelerated form of oxidation that occurs when metals and metal alloys are heated in the temperature range 700–900°C in the presence of alkali salts. An increased understanding of the fundamental behaviors of common high temperature alloys and their degradation mechanisms is therefore critical for the production of reliable components.

In this study a model substrate, Nickel 201, was coated on one side with Cr, Al, or Si thin films (~1 μm) via magnetron sputtering physical vapor deposition (PVD). Uncoated and PVD coated samples were then exposed to laboratory air at 700°C and 900°C and to an environment similar in composition to atmospheres found in post combustion turbine systems, comprised of air/SO_2 gas mixture, at 700°C. The exposures were conducted over time intervals observing coating-substrate interactions and surface oxide development. Identical samples were subjected to the same exposures with addition of a deposit of sodium sulfate (Na_2SO_4), a model alkali salt. Sample mass gains were recorded and resulting oxide compositions assessed as a function of exposure time using microscopy techniques on sample surfaces and cross sections. The development of intermetallic species was determined by X-ray diffraction. At 700°C, coated and uncoated samples displayed different oxidation behaviors. Under laboratory air, no hot-corrosion occurred. While at 700°C in air/SO_2 exposures, evidence for hot corrosion on deposited samples was observed. When sodium sulfate was introduced at 900°C, coated and uncoated samples displayed rapid corrosion consistent with hot corrosion. The oxidation processes and coating/substrate inter-diffusion phenomena are presented and discussed in the context of establishing basic approaches to improve the fundamental understanding of hot corrosion, and the protection mechanisms of high temperature materials.

INTRODUCTION

1.1 Energy Conversion Systems:

Converting energy into useful forms is a crucial aspect of modern technology. A common type of energy conversion process is the generation of shaft work through the rotation of a turbine. With the exception of processes relying on photovoltaic cells and piston driven engines, the use of a rotating turbine is still the primary method for the generation of energy.

One of the earliest forms of energy conversion was the water wheel. The simplest form of water wheel involves a turbine capturing the motion of moving water, typically a river. The motion captured by the turbine rotates a shaft thereby generating work which can in turn be used to complete some task. The water wheel exemplifies one of the primary advantages of turbine technology; minimal moving parts with areas that are in contact. The absence of friction generating components means that turbine engines require significantly less lubrication than piston driven engines decreasing necessary maintenance[1].

Replacing flowing water steam at the beginning of the 20th century was one of the most important innovations in electrical generation[1]. While this process was largely responsible for the industrial revolution early examples were inefficient largely due to the low operating temperatures. This is because the work generated by an engine is proportional to the operating temperature[2].

Equation 1 describes the maximum theoretical work (ω_{max}) that can be obtained during operation[2].

$$\omega_{max} = \frac{T - T_0}{T} q \qquad \text{Equation 1}$$

In Equation 1 q represents the heat exchanged, T is the operating temperature, and T_0 is the ambient temperature[2]. If the operating temperature becomes large the first term becomes approximately equal to 1, and the theoretical work simply becomes equal to the heat exchanged. The efficiency (η) can also be related to the operating temperature as described in Equation 2[1].

$$\eta = \frac{c_p(T_3 - T_4) - c_p(T_2 - T_1)}{c_p(T_3 - T_2)} \qquad \text{Equation 2}$$

In Equation 2 c_p is the heat capacity of the process gas, T_1 is equal to the ambient temperature, T_2 is the temperature of the gas during compression, T_3 is the temperature of the gas during combustion, and T_4 is the temperature of the exhaust gas[1]. Equation 2 demonstrates that it is desirable to achieve large temperature differences between the gases within and outside of the turbine. Thanks to significantly improved materials modern steam turbines have efficiencies as high as 40 percent and are capable of producing shaft work in excess of 1000 MW[1]. The need for ever greater efficiencies and improved component lifespan continues to drive development of high temperature materials.

1.2 Modern Turbine Engine Cycle:

Figure 1 displays a cross section of a jet engine, a common type of gas turbine engine.

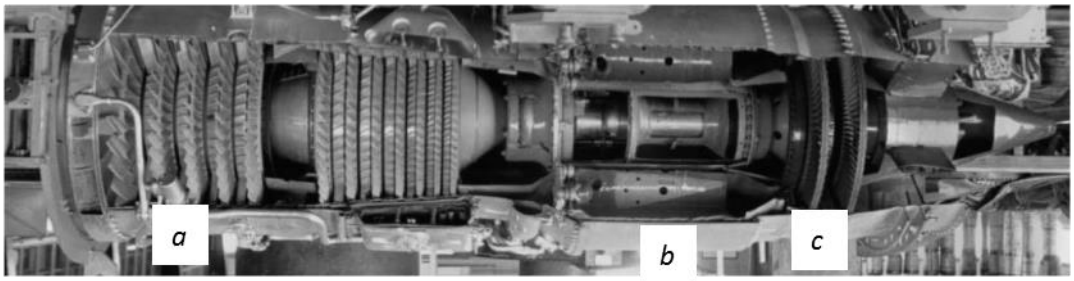

Figure 1: a jet engine with the compressor (a), combustor (b), and turbine (c) labeled[3]

Whether for generating electricity or as engines for propulsion, turbines operate in a series of steps known as the turbine cycle consisting of three steps: compression, combustion, and expansion[1]. During combustion, taking place within the combustion chamber *b* in Figure 1, the temperature of the process gas is raised before expansion, increasing the energy[1]. The hot gasses produced in the combustion chamber then flow over the angled turbine blades within the post combustion section of the engine, component *c* from Figure 1[2]. The flow of the process gas over the blades generates shaft work to run the engine's compressor (component *a*)[2]. In an idealized situation where no losses between components occurs, compression of the working fluid, most often air, and subsequent expansion in the turbine section would be sufficient to create the shaft work necessary to run the compressor[1]. In the specific case of turbine engines the excess energy generated by combustion is expelled in the form of exhaust gasses which rapidly flow out of the back of the engine and generate the thrust necessary for propulsion[1,2]. As mentioned previously, high temperatures are desirable in order to increase both the generated energy and the combustion efficiency. The high temperature and pressure conditions realized in modern turbines present unique challenges to material design.

1.3 High Temperature Materials:

The turbine combustion and post combustion sections are labeled *b* and *c* respectfully in Figure 1. Their components are exposed to oxidizing environments with temperatures up to about 1700°C and pressures as high as 30 MPa [1,3]. Figure 2 describes the temperatures, stresses, and unique challenges that engine components face during the turbine cycle[4].

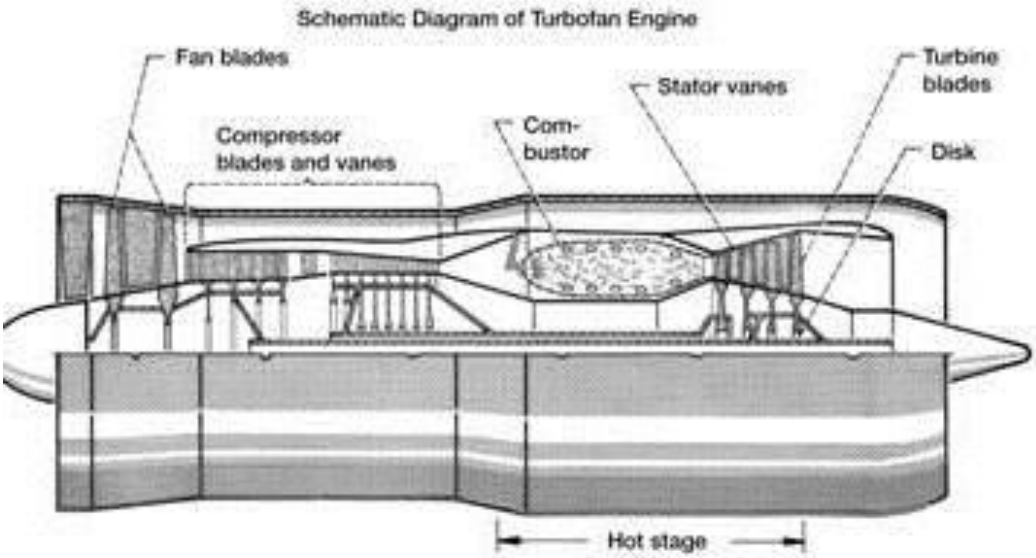

Component	Typical Operating Conditions			Critical Problems
	Temperature (°C)	Stress (MPa)	Life (hr)	
Blades	900 - 1050	140 - 210	5000	Creep strength, stability, oxidation, hot corrosion, thermal fatigue
Vanes	950 - 1100	35 - 70	5000	Thermal fatigue, oxidation, hot corrosion
Disks	400 - 650	420 - 1050	15 000	Low cycle fatigue
Combustors	850 - 1100	20 - 35	4000	Thermal fatigue, oxidation

Figure 2: Operating conditions and issues with various turbine components[4]

The advanced alloys used in turbine construction require specific traits such as low density, high creep and oxidation resistance, and damage tolerance. One category of materials able to satisfy the majority of these requirements is nickel superalloys; in particular, they offer exceptional creep resistance, a trait which prolongs component lifespan, thus improving reliability and reducing costs[5]. Commonly used alloying elements include aluminum (Al), chromium (Cr), and silicon (Si)[6,7]. The partial ternary phase diagram for Ni-Cr-Al alloys at 1000°C, that highlights the significance of Cr and Al in the design of Ni superalloys is presented in Figure 3[8].

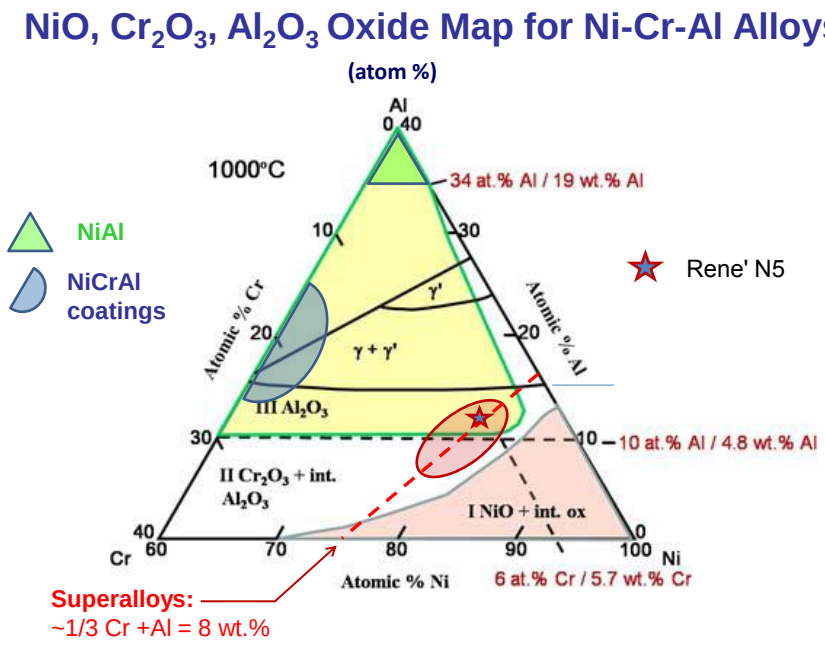

Figure 3: Phase diagram for Ni-Cr-Al alloys[9]

Cr and Al are suitable due to the ability, at high temperatures, to form superficial stable native oxide protective scales that prevent further oxidation. Due to the suitability of these alloys for high temperature applications they represent the majority of material used

in the construction of combustion chambers and turbine blades in modern turbine engines[3,7].

Protecting advanced alloys from the high temperature oxidizing environments realized in modern energy conversion systems, such as turbine engines, is a continual challenge for materials development[10]. In order to further improve the oxidation resistance of superalloys various coating strategies are employed [11–14]. Protective coatings consist of either oxides or elements, frequently Al, Cr, and Si, capable of forming well adhered protective oxides under the conditions specific to turbine engines, including high temperatures and thermal cycling[2,7,13,15–20]. Understanding the fundamental interactions of super-alloys and protective coatings enables more effective design, which can lead to increases in component lifespan.

Applied coatings are grouped into three categories: overlay, thermal barrier, and diffusion coatings [11]. Overlay coatings, which protect alloys from oxidation, typically consist of elements not found within the substrate and are often applied by physical vapor deposition (PVD) methods. Thermal barrier coatings are layered coatings consisting of top layers well suited to protecting and insulating the underlying substrate, through the formation of a temperature gradient, and bottom layers designed specifically for adhesion to the substrate. Typically, thermal barrier coatings are applied through PVD or other spray application methods. Finally, diffusion coatings rely on the ability of metals to inter-diffuse within the atomic lattice of other metals. The method of application for diffusion coatings is known as packed cementation and involves surrounding the substrate in a metal powder and heating. The resulting intermetallic species present

within the inter-diffusion zone can offer improved corrosion resistance through synergistic effects.

1.4 Physical Vapor Deposition:

Application of overlay protective coatings using PVD methods is a common strategy for high temperature materials. PVD involves the vaporization of material from either a solid or a liquid source and subsequent deposition onto a selected substrate[21]. For the purposes of this thesis the type of PVD to be discussed is sputter deposition. Sputter deposition involves the ejection of material from a solid surface or "target" by momentum transfer from an accelerated gaseous ion[21,22]. A summary of the sputtering PVD process is presented in Figure 4[23].

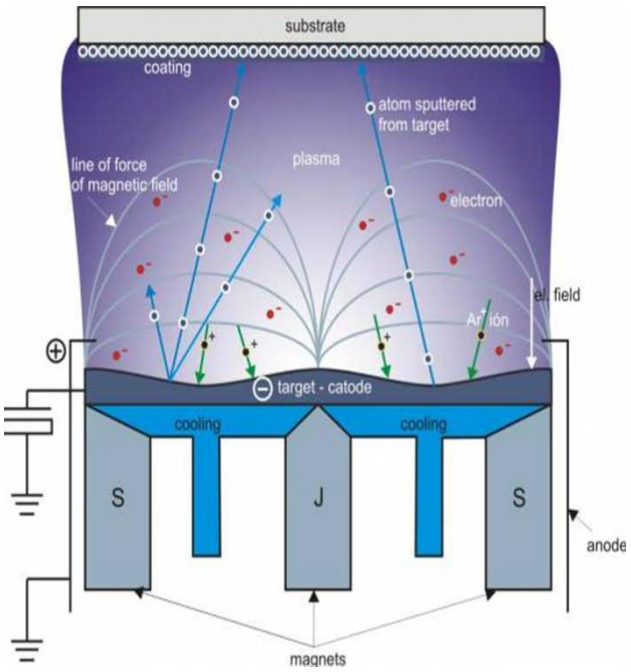

Figure 4: Summary of the PVD sputtering process[23].

Plasma is generated through the excitation of the valence electrons of an elemental process gas, typically argon, by either radio frequency (RF) or direct current (DC) electric fields [24]. The excitation of these electrons leads to collisions between electrons and atoms, generating a large quantity of ions and other charged particles without requiring high temperatures. In general, the positively charged gaseous ions from the plasma are accelerated toward a negatively charged target in a high vacuum environment[21]. The lack of gas molecules within the vacuum chamber, which if present would restrict movement through collision, allows for high speeds to be developed before the gas ion impacts the target surface. The impact energy of the accelerated ionic particles is then transferred to the target metal atoms; if the energy is sufficiently high this action causes ejection of atoms, or sputtering, from the target surface. This method of vaporization is a physical rather than a thermal process as had been previously proposed. The specific process by which sputtering is accomplished varies significantly depending on the type of electric field present.

In DC magnetron sputtering electrons ejected from the cathode are deflected using magnetic fields. The deflected electrons then circulate on a closed path confined to a region above the target surface[21]. The result is dense plasma capable of producing ions for sputtering of the target.

In the case of RF controlled sputtering, a large potential is alternated between positive and negative across the target surface[21]. Alternating the potential to positive at high frequency allows electrons to reach the surface and prevent charge build up and subsequent discharge, thus resulting in a more stable system. However, an externally

applied negative potential maintains a net negative charge on the target surface with respect to the positively charged plasma, resulting in positively charged gas ions accelerating towards the target surface. Very high bombardment energies can be achieved with this method due to a decrease in the required pressure of process gas.

While some of the energy is consumed as atoms sputtered from the target surface, the majority of the energy from the impacting particles becomes heat both on and below the target surface[21]. Since not all of the impacts lead to ejected atoms , the sputtering yield is defined as the ratio of atoms ejected to the number of charged particles that collide with the surface. This ratio provides information on the efficiency of process gasses for a selected metal target. The reason argon is so frequently used as a process gas is because it allows a high sputtering yield across a number of metal targets[25].

Following target vaporization the ejected atoms condense on the surface of the sample substrate[21]. The sputtered atoms condensation energy is in largely transferred to the sample substrate and causes heating. However, if particles, such as high energy reflected neutrals impact the growing coating with sufficient force, as may be the case in very high vacuum environments, they can cause re-sputtering of the condensed target material. If this is the case then re-sputtering may have the effect of lowering apparent deposition rates. To decrease the possibility of re-sputtering it is common to maintain the pressure at approximately 5 millitorr (mT).

Many possible target geometry configurations are available in magnetron sputtering systems; the specific configuration used in this work is described in Figure 5[21]. A photo of the system depositing two different elements simultaneously is also included.

The capability to use multiple targets in the same deposition process allows for rapid development of a wide range of substrate coatings.

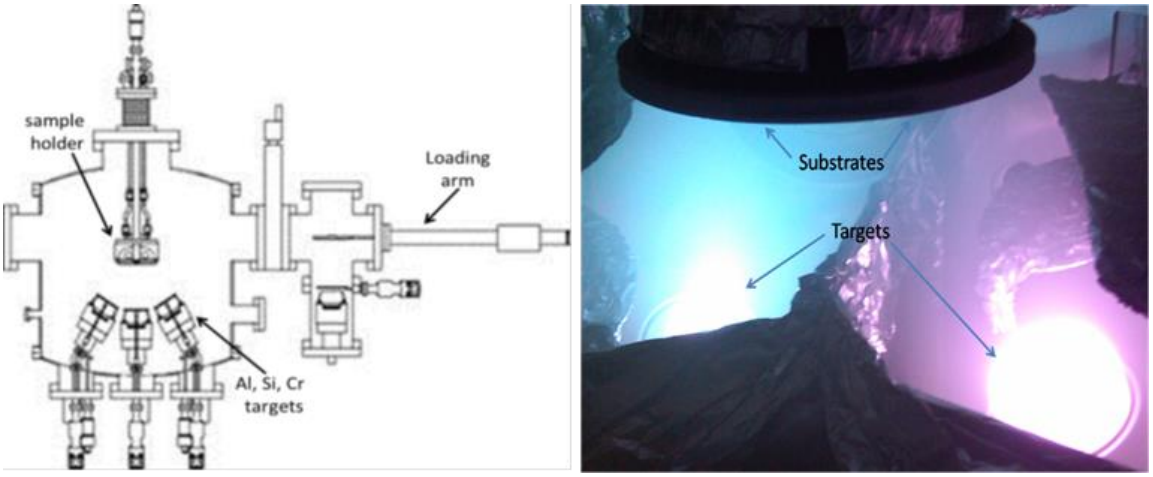

Figure 5: Schematic of the multi-source RF-magnetron sputtering system[26] (left) and photograph of the instrument during deposition (right)

1.5 High Temperature Oxidation:

Under high temperature conditions, 600°C-1200°C, alloys and pure metal surfaces form native oxide layers either through pre-oxidation treatments prior to use or while the system is being heated to operating temperatures[6]. The formation of these oxides through reaction with oxygen occurs so rapidly that the rate of ionic diffusion through the formed oxide layer, or scale, is the more important factor to the overall growth rate. If the ionic diffusion rates are low, and the formed oxide scale is continuous and well adhered to the surface at operational conditions, the oxide layer protects the underlying metal from further oxidation.

Equation 3 describes the generic reaction between metal cations, free electrons, and molecular oxygen.

$$M^{2+} + 2e^{-} + \frac{1}{2}O_2 = M_xO_y \qquad \text{Equation 3}$$

In Equation 1 M^{2+} represents the metal cation, e^{-} represents an electron, O_2 is molecular oxygen, and *MO* is metal oxide. The subscripted variables x and y are dependent upon the valiance state of the metal. In order to determine if an oxide will form it is necessary to consider the thermodynamic properties of the reaction for a given set of reactants.

The ability of particular metals to form oxides is determined by the second law of thermodynamics, which describes the tendency of systems towards equilibrium[27]. Given the operating conditions of energy conversion systems, specifically constant temperatures and pressures, the most useful form of the second law is Gibb's free energy given by G in Equation 4[6,27].

$$G = U + PV - TS \qquad \text{Equation 4}$$

$$Where: U = TS - PV + \sum_{i=1}^{n} \mu_i N_i$$

In Equation 4, U is the internal energy, T is the temperature, P is the pressure, V is the volume, μ is the chemical potential of a given species, N is the molar concentration of a given species, and S is the entropy of the system. Alternatively this relationship can be expressed in the form described by Equation 5[4,27].

$$G = H - TS \qquad \text{Equation 5}$$

$$Where: H = U + PV$$

Calculating the change in Gibbs free energy for a given reaction is an effective way to understand the likelihood of a reaction occurring. Equation 6 demonstrates a method commonly employed to determine a value for free energy change[4,27]

$$\Delta G = \Delta G° + RT \ln K_{eq} \quad \text{Equation 6}$$

In Equation 6, $\Delta G°$ is the standard state free energy change for all species present, R is the gas constant, and K_{eq} is the equilibrium constant. The equilibrium constant is the ratio of the activities of the reacting species[4,6]. Equation 7 describes how the value of the equilibrium constant is calculated in relation to the reaction presented in Equation 3[4].

$$K_{eq} = \frac{a_{M_xO_y}}{a_{M^+}(p_{O_2})_{eq}^{\frac{1}{2}}} \quad \text{Equation 7}$$

The activity of each species, a, in Equation 7, can be related back to the chemical potential by Equation 8, where μ_A° is the chemical potential of a species in its standard state[6].

$$\mu_A - \mu_A^{\circ} = RT \ln a_A \quad \text{Equation 8}$$

Equations 4-8 illustrate how the change in Gibb's free energy, ΔG, for a chemical reaction can be expressed as a function of temperature, T, and the thermodynamic activities of the species involved[4,6].

The value of ΔG predicts the formation and stability of oxide species. The values determined for a number of materials can then be graphed in order to predict the relative suitability for formation of protective oxide species. An example of a method for

presenting the relevant data, a Modified Ellingham/Richardson diagram, is presented in Figure 6[4].

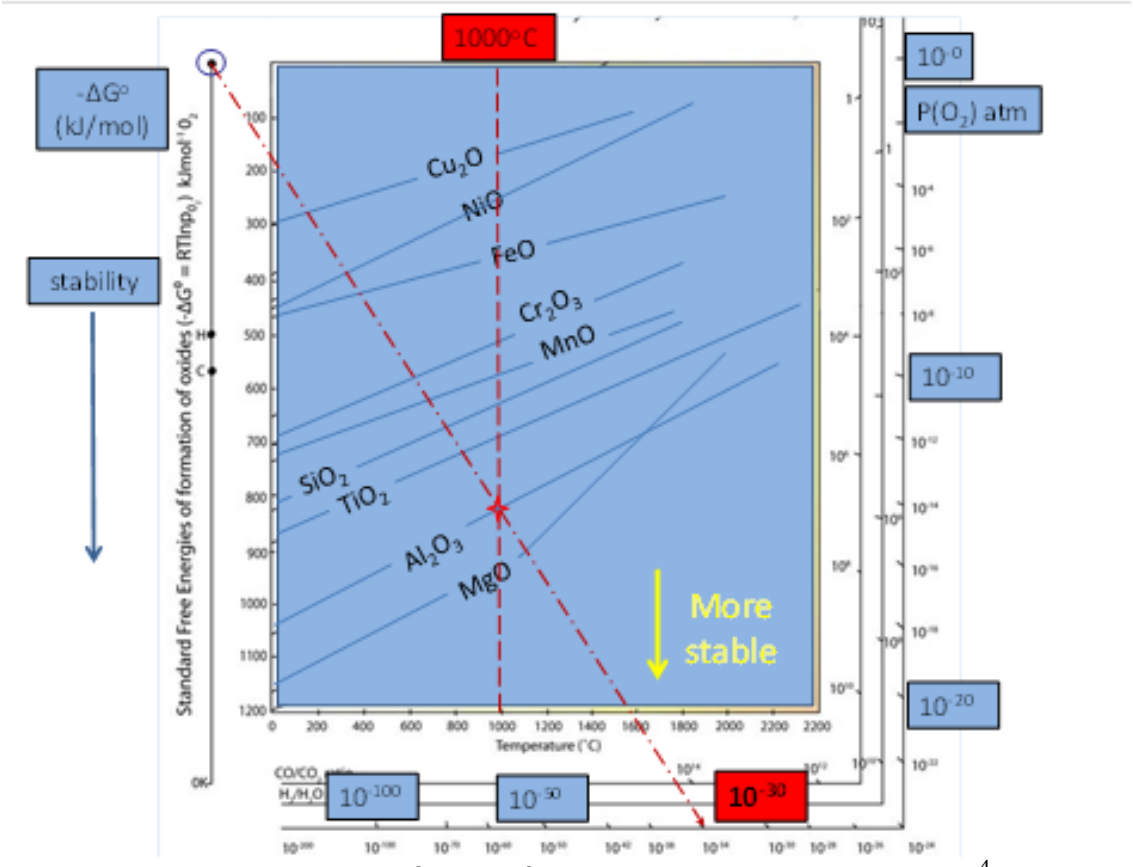

Figure 6: Example of a Modified Ellingham/Richardson diagram[4]

In Figure 6 the x-axis is temperature, y-axis is the standard free energy of formation, and the oxygen partial pressures at which the oxide formation takes place surrounds the outside of the figure. Ellingham/Richardson diagrams allow for comparison of expected oxide layer growth rates under a range of conditions. It will be shown later that the rate of oxide growth is an important indication of protective ability. Thermodynamic analysis such as this indicates why alloying elements are chosen to improve the fundamental resistance to oxidation of these base elements.

Formation of the oxide at the metal surface as described by Equation 3 results in a separation of reactants as described by Figure 7, where the scale-gas interface is labeled as *1* and the metal-scale interface is labeled as *2*.

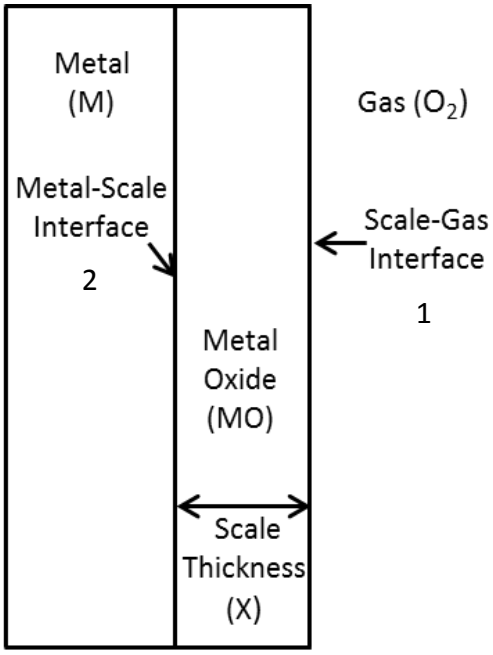

Figure 7: Separation of reactants from Equation 3 by metal oxide[6]

For the reaction to continue transport of the two reactants, oxygen and metal ions, through the metal oxide is necessary. The oxide layer depicted in Figure 6 consists of metal cations (M^{2+}) and oxygen anions (O^{2-}). Due to the described ionic nature of the oxide layer, reaction elements are transported in their ionic form[6].

In situations where an oxide layer has yet to form or is so thin that transport of reactants is not the rate limiting step oxidation proceeds as a first order linear reaction[2,6]. When this is the case the scale growth rate is described by Equation 9[2].

$$\frac{dX}{dt} = k_1 \qquad \text{Equation 9}$$

In Equation 9 X represents the scale thickness, t represents time, and k_1 is the linear rate constant[2]. Integrating Equation 9 with the boundary condition of $X = 0$ at $t = 0$ gives the familiar form presented in Equation 10[2].

$$X = k_1 t \qquad \text{Equation 10}$$

This process only dominates until an oxide scale has been developed at which point further oxidation is controlled by the rate of ionic transport though the growing scale[2,6].

To describe the ionic transport within a solid, two different categories based upon the composition of the solid have to be considered: stoichiometric crystals and non-stoichiometric crystals[6]. Many metals and metalloids including Ni, Al, Cr, and Si form native oxide scales which are non-stoichiometric in nature. For this reason the non-stoichiometric category of transportation will be described. This category can be divided in to negative, n-type, and positive, p-type, semiconductors based upon the type of charge that is transferred through the solid during defect formation[6]. The charges are propagated through formation of defects, also called holes. In n-type semiconductors this is due either the presence of excessive metal ions or a deficit of nonmetal ions. In p-type semiconductors the charge propagation is due to a deficit of metal ions within the solid ionic lattice.

In the case of deficit formation, also known as excess metal, the surplus metal ions are caused by the loss of an oxygen ion from the lattice as described by Equation 11[6].

$$MO = M^{2+} + 2e^- + \frac{1}{2}O_2 \qquad \text{Equation 11}$$

The free electrons generated in Equation 11 have suitable energy for entry into the conduction band of the solid while the metal cation enters into an interstitial site within the lattice. Another possibility is that only a singly charged interstitial metal will be formed as is described by Equation 12[6].

$$M^{2+} + e^{-} = M^{+} \qquad \text{Equation 12}$$

The total resulting vacancy volume described by Equations 11 and 12 is small in relation to the actual bulk of the material. The concentration of vacancies therefore falls within the Henry's law regime where equilibrium can be written as a function of concentration instead of activity as in Equation 13 for doubly charged defects[6].

$$K = C_{M^{2+}} C_{e^-} \left(p_{O_2}^{1/2} \right) \qquad \text{Equation 13}$$

Equation 13 can be further manipulated in order to determine the dependence of conduction electron band formation on the partial pressure of oxygen. This is accomplished by first setting the concentration of conduction band electrons (C_{e^-}), either one or two, equal to the concentration of metal cations (C_{M^+}). This method is described by Equations 14 and 15[6].

$$C_{M^{2+}} = 2C_{e^-} \qquad \text{Equation 14}$$

$$C_{M^{+}} = C_{e^-} \qquad \text{Equation 15}$$

Substituting Equation 14 into Equation 13 and solving for the concentration of electrons results in Equations 16 and 17 for doubly and singly charged deficits respectfully[6].

$$C_{e^-} = A * p_{O_2}^{-1/6} \qquad \text{Equation 16}$$

$$C_{e^-} = A * p_{O_2}^{-1/4}$$ Equation 17

In Equations 16 and 17, A is a constant related to the equilibrium constant. Equations 16 and 17 indicate that the formation of conduction band electrons is proportional to the partial pressure of oxygen in the system[6]. Using these proportionalities it should be possible to measure the conductivity of an oxide as a function of the oxygen partial pressure in order to determine which defect is dominating the solid[6]. Studies have shown that the conductivity in relation to oxygen partial pressure falls somewhere in between these two exponents, a result which demonstrates that oxides of this variety likely include both defects[28].

Another possibility upon evaporation of oxygen from an oxide layer is the formation of a non-metal deficit. In this case an oxygen anion evaporates and an oxygen vacancy is generated with no cationic metal interstitial being formed as described in Equation 18[6].

$$O^{2-} = {V_O}^{2+} + 2e^- + \frac{1}{2}O_2$$ Equation 18

Similarly to the reaction from Equations 11 and 12, the free electron or electrons generated by the process described in Equation 18 have sufficient energy to enter the conduction band. Due to the formation of the oxygen vacancy, which is highly positive in charge, it is possible for free electrons to enter the vacancy resulting in either a singly charged or neutral vacancy as described by Equations 19 and 20[6].

$${V_O}^{2+} + e^- = {V_O}^{+}$$ Equation 19

$$V_O{}^{+} + e^{-} = V_O \qquad \text{Equation 20}$$

The derivation of equations linking the concentration of conduction band electrons for the doubly and singly charged defects to the partial pressure of oxygen remains identical to that used to generate Equations 16 and 17[6]. Conversely, the occurrence of neutral oxygen vacancy sites is proportional to the concentration of conduction band electrons but is independent of the partial pressure of O_2[6].

The last type of defect formation, wherein vacancies in the cation lattice are formed by the transport of metal ions[6]. This p-type semi-conduction process is active in many metal oxides including Ni, Cr, and Al. The formation of low energy electron holes which are necessary for conduction is based upon the ability of the metal ions to exist in more than one valence state. In order to switch readily, the valence states of the cation must also be close energetically. Reaction with oxygen on the metal oxide surface further oxidizes metal cations within the lattice. This process ionizes the molecular oxygen bonding it to the surface. A second oxidation event then occurs resulting in two electron holes being generated. A non-oxidized metal cation then migrates to the surface to interact with the now fully ionized oxygen. The migration of this metal cation to the surface results in a cation vacancy within the lattice and more oxide formation at the surface. This reaction can be described by Equation 21[6].

$$\frac{1}{2}O_2 = O^{2-} + 2h^{+} + V_M^{2-} \qquad \text{Equation 21}$$

In Equation 21 h^{+} is the hydronium ion and represents metal cations while the other variables retain their definitions. Equation 21 is also subject to Henry's law due to the low concentration of vacancies within the lattice. An assumption that means the

equilibrium constant can be given a treatment similar to that from Equation 13 and be written as Equation 22[6].

$$K = \frac{(C_{h^+})(C_{V^{2-}})}{p_{O_2}^{1/6}} \qquad \text{Equation 22}$$

An additional possibility during the oxidation process described in Equation 21 is that an oxidized cation or electron hole occupies one of the metal vacancies within the lattice[6]. When this occurs it creates an effect similar to the singly charged oxygen vacancies described above as described by Equation 23.

$$\frac{1}{2}O_2 = O^{2-} + h^+ + V_{M^+}^- \qquad \text{Equation 23}$$

The equilibrium constant for Equation 23 can be described similarly to that for Equation 21[6]. This reveals that similarly to the concentration of conduction band electrons, the concentration of hydronium ions (C_{h^+}) is proportional to the oxygen partial pressure. The results are described for metal vacancies and those with bound cations as Equations 24 and 25 respectfully[2,6].

$$C_{h^+} = A * p_{O_2}^{1/6} \qquad \text{Equation 24}$$

$$C_{h^+} = A * p_{O_2}^{1/4} \qquad \text{Equation 25}$$

Studies on the conductivity of p-type semiconductors in relation to the oxygen partial pressure have shown that both types of vacancies are present[28]. Equations 16, 17, 24, and 25 demonstrate that an important difference between n-type and p-type

semiconductors is the sign of their proportionality to oxygen partial pressure. For n-type the dependence is negative and for p-type the dependence is positive[6].

Transport of ionized reactants across the boundary of reaction products as illustrated by Figure 6 is often the rate limiting step for oxidation reactions. The transport of reactant namely metal cations (M^{2+}) must additionally be equal and opposite to the flux of defects into the oxide layer. This process is described by Equation 26 for the situation arising when the defects within the lattice are metal vacancies ($V_{M^{2-}}$)[2,6].

$$j_{M^{2+}} = -j_{V_M{}^{2-}} = D_{V_M{}^{2-}} \frac{\left(C^1{}_{V_M{}^{2-}}\right) - \left(C^2{}_{V_M{}^{2-}}\right)}{X} \qquad \text{Equation 26}$$

In Equation 26, $D_{V_M{}^{2-}}$ represents the diffusion coefficient of metal vacancies, X is equal to the thickness of the oxide layer, $\left(C^1{}_{V_M{}^{2-}}\right)$ is the vacancies at the oxide scale-gas interface, and $\left(C^2{}_{V_M{}^{2-}}\right)$ is equal to the vacancies present at the oxide metal-scale interface[6]. Assuming that thermodynamic equilibrium holds at the metal-scale and scale-gas interfaces described in Figure 7, the value of $\left(C^1{}_{V_M{}^{2-}}\right) - \left(C^2{}_{V_M{}^{2-}}\right)$ from Equation 26 remains constant. If this is the case, the thickening of the oxide layer proceeds as described by Equation 27[6].

$$j_{M^{2+}} = \frac{1}{V_{ox}} \frac{dx}{dt} \qquad \text{Equation 27}$$

In Equation 27 V_{ox} is equal to the volume of the oxide. Substitution between Equations 26 and 27 and combining variables yields Equation 28[2,6].

$$\frac{dx}{dt} = \frac{k\prime}{x} \qquad \text{Equation 28}$$

$$k' = \left(D_{V_M{}^{2-}}\right)V_{ox}\left[\left(C^1{}_{V_M{}^{2-}}\right) - \left(C^2{}_{V_M{}^{2-}}\right)\right]$$

In Equation 28, k' represents the parabolic rate constant. Integrating Equation 28 with respect to time (t) and oxide layer thickness (X) results in the parabolic rate law, Equation 29[2,6].

$$x^2 = 2k't \qquad \text{Equation 29}$$

It is also possible to approximate the parabolic rate constant using the partial pressure of oxygen[6]. This is due to the number of cation vacancy sites being related to the partial pressure of oxygen similarly to Equations 16 and 17[6]. Equation 30 results from the combination of Equations 16 and 17.

$$k'\alpha \left[\left(p_{O_2}^{Ox-G}\right)^{1/n} - \left(p_{O_2}^{M-Ox}\right)^{1/n}\right] \qquad \text{Equation 30}$$

In Equation 30 $p_{O_2}^{Ox-G}$ represents the partial pressure of oxygen at the oxide-gas interface and $p_{O_2}^{M-Ox}$ represents the partial pressure at the metal-oxide interface. Typically the partial pressure at the oxide-gas layer dominates, meaning the $p_{O_2}^{M-Ox}$ term can be ignored[6]. In order to better conceptualize and calculate the value of the parabolic rate law Wagner's Theory must discussed.

1.6 Wagner's Theory:

Wagner developed a model to described lattice diffusion of ions and positive holes within oxide scales to predict the effects of changes in temperature and chemistry

on oxidation growth and to better understand the ionic process[2,6]. In order for this theory to accurately describe the diffusion process a number of conditions must be met:

- A dense well adhered oxide layer that prevents gas phase transfer within the scale[2,6].
- Migration of ions or electrons across the scale is the rate controlling process[2,6].
- Thermodynamic equilibrium at the metal-oxide interface, throughout the scale, and at oxide-gas interface must be established rapidly enough to not affect the rate[2,6].
- The oxide scale must be well ordered, meaning the scale contains minimal grain boundaries and dislocations, and have few deviations from stoichiometry. This condition is necessary so that diffusion rates do not vary significantly by position within the scale[2,6].
- The solubility of oxygen within the metal must be negligible[2,6].

If the conditions described are met, then due to the condition requiring thermodynamic equilibrium, activity gradients for both metal and non-metal are established across the scale[6]. The result of these gradients is that metal ions and oxide ions will migrate across the oxide scale in opposite directions. As the ions migrate they give rise to an electric field across the oxide scale. This field corresponds to electron transport across the scale, to the oxide-gas interface, and into the surrounding atmosphere. The result of the equal and opposite migrations of the cations, anions, and electrons is that no net charge is transferred across the oxide scale, a situation known as the condition of zero net electric current[2,6].

The two gradients that the ions are subject to are chemical-potential ($\frac{\partial \mu_i}{\partial x}$) and electrical-potential ($\frac{\partial \phi}{\partial x}$)[6]. Combining these two gradients it was determined that an ion with a charge, Z_i, is subject to a force described by Equation 31[6].

$$\frac{1}{N_A}\left(\frac{\partial \mu_i}{\partial x} + Z_i F \frac{\partial \phi}{\partial x}\right) J\ particle^{-1} cm^{-1} \qquad \text{Equation 31}$$

In Equation 31, N_A is Avogadro's number and F is the Faraday constant in coulombs equiv^{-1} [6]. The drift velocity (ν) is equal to the applied force multiplied by the average drift velocity per unit force, or particle mobility (B) as described by Equation 32[6].

$$\nu = -\frac{B_i}{N_A}\left(\frac{\partial \mu_i}{\partial x} + Z_i F \frac{\partial \phi}{\partial x}\right) \qquad \text{Equation 32}$$

In Equation 32, B is expressed in units of particle cm^2 J^{-1} s^{-1} [6]. The negative sign in Equation 32 is due to the drift occurring in the positive x direction and the negative direction for the chemical (μ_i) and electrical (ϕ) gradients. Multiplying the drift velocity by the concentration (C_i) yields the flux of particles as described in Equation 33[2,6].

$$j_i = -\frac{C_i B_i}{N_A}\left(\frac{\partial \mu_i}{\partial x} + Z_i F \frac{\partial \phi}{\partial x}\right) mol\ cm^{-2} s^{-1} \qquad \text{Equation 33}$$

In order to further simplify Equation 33 it is useful to relate the particle mobility to the diffusion coefficient (D) and the conductivity (κ) of the particle as described in Equation 34[6].

$$D_i = k_B T B_i = \frac{RT\kappa_i}{C_i (Z_i F)^2} \qquad \text{Equation 34}$$

The result of solving Equation 34 for B_i is Equation 35.

$$B_i = \frac{\kappa_i}{C_i(Z_iF)^2} \qquad \text{Equation 35}$$

Further simplification of Equation 33 is accomplished by substitution of Equation 35 yielding Equation 36[6].

$$j_i = -\frac{\kappa_i}{(Z_iF)^2}\left(\frac{\partial \mu_i}{\partial x} + Z_iF\frac{\partial \phi}{\partial x}\right) \qquad \text{Equation 36}$$

Equation 36 can then be used to describe the flux of the rapidly diffusing particles, electrons and cations, as described by Equations 37 and 38[2,6].

$$j_e = -\frac{\kappa_e}{(Z_eF)^2}\left(\frac{\partial \mu_e}{\partial x} + Z_iF\frac{\partial \phi}{\partial x}\right) \qquad \text{Equation 37}$$

$$j_c = -\frac{\kappa_c}{(Z_cF)^2}\left(\frac{\partial \mu_c}{\partial x} + Z_iF\frac{\partial \phi}{\partial x}\right) \qquad \text{Equation 38}$$

The condition of zero net electric current described previously can be written as Equation 39[6].

$$0 = Z_cj_c + Z_ej_e \qquad \text{Equation 39}$$

Solving for the electric gradient in Equations 36 and 37 results in Equation 40[6].

$$\frac{\partial \phi}{\partial x} = -\frac{\kappa_c\kappa_e}{F(\kappa_c+\kappa_e)}\left(\frac{\kappa_c}{Z_c}\frac{\partial \mu_c}{\partial x} + \frac{Z_c}{Z_e}\frac{\partial \mu_e}{\partial x}\right) \qquad \text{Equation 40}$$

Substitution of Equation 40 into Equation 38 eliminates the electric gradient term which is displayed as Equation 41[6].

$$j_c = -\frac{\kappa_c\kappa_e}{(Z_cF)^2(\kappa_c+\kappa_e)}\left(\frac{\partial \mu_c}{\partial x} - \frac{Z_c}{Z_e}\frac{\partial \mu_c}{\partial x}\right) \qquad \text{Equation 41}$$

Recognizing that the charge of an electron has a value of negative one, $Z_e = -1$, Equation 41 becomes Equation 42[6].

$$j_c = -\frac{\kappa_c \kappa_e}{(Z_c F)^2(\kappa_c+\kappa_e)}\left(\frac{\partial \mu_c}{\partial x} - Z_c \frac{\partial \mu_c}{\partial x}\right) \qquad \text{Equation 42}$$

Finally recognizing that the ionization of metal is equivalent to the chemical potential of the metal (μ_M). The chemical potential of the metal can then be written as Equation 43[6].

$$\mu_M = \mu_c + Z_e \mu_e \qquad \text{Equation 43}$$

Combining Equations 42 and 43 yields Equation 44, which is the expression for flux within the scale[6].

$$j_c = -\frac{\kappa_c \kappa_e}{(Z_c F)^2(\kappa_c+\kappa_e)}\frac{\partial \mu_M}{\partial x} \qquad \text{Equation 44}$$

Integrating Equation 44 over the thickness of the scale (X) and for the chemical potential of metal (μ_M) from the metal-oxide interface (μ^1) to the oxide-gas interface (μ^2) yields Equation 45[6].

$$j_c = -\frac{1}{(Z_c F)^2 x}\int_{\mu_M^1}^{\mu_M^2} \frac{\kappa_c \kappa_e}{(\kappa_c+\kappa_e)} d\mu_M \; mol\; cm^{-2} s^{-1} \qquad \text{Equation 45}$$

Extending the treatment given cationic flux, Equation 38, to electrons, Equation 37, the result is described in Equation 46[6].

$$j_e = -\frac{1}{Z_e F^2 x}\int_{\mu_M^1}^{\mu_M^2} \frac{\kappa_c \kappa_e}{(\kappa_c+\kappa_e)} d\mu_M \; mol\; cm^{-2} s^{-1} \qquad \text{Equation 46}$$

The process for cationic and anionic transport is summarized in Figure 7, where M^x represents a metal ion on the lattice and O^x represents an oxygen ion on the lattice.

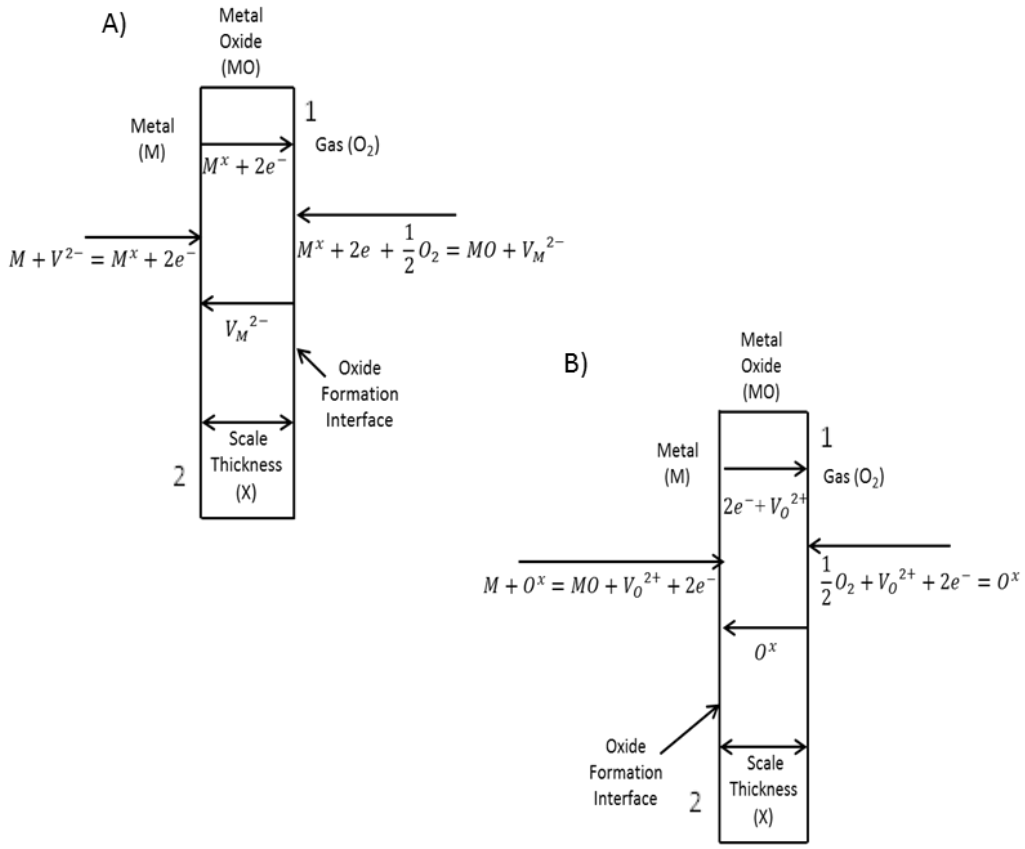

Figure 8: Summary of transport when metal cation transport dominates (A) and when oxygen anion transport dominates (B)[6].

This expression for flux can be simplified greatly if the concentration of metal within the oxide scale is expressed as C_M, having the units $mol\ cm^{-3}$, as described by Equation 47[6].

$$j_c = C_M \frac{dx}{dt} \qquad \text{Equation 47}$$

This result is important because it implies Equation 48, where Equations 45 and 46 are used to determine the parabolic rate constant from Equation 29, relating scale growth to flux[6].

$$k' = \frac{1}{(Z_c F)^2 C_M} \int_{\mu_M^2}^{\mu_M^1} \frac{\kappa_c \kappa_e}{(\kappa_c + \kappa_e)} d\mu_M \qquad \text{Equation 48}$$

In Equation 48 the negative sign is dropped and the integration is carried out from the oxide-gas interface to the metal-oxide interface. It is then possible to reintroduce the diffusion constant of metal (D_M) using Equation 35, resulting in Equation 49[6].

$$k' = \frac{1}{RT} \int_{\mu_M^2}^{\mu_M^1} D_M \, d\mu_M \; cm^2 s^{-1} \qquad \text{Equation 49}$$

Conversely, the parabolic rate constant for a non-metal moving through the oxide scale can be written as Equation 50[6].

$$k' = \frac{1}{RT} \int_{\mu_M^1}^{\mu_M^2} D_M \, d\mu_M \; cm^2 s^{-1} \qquad \text{Equation 50}$$

Wagner's theory predicts the rate constants of many systems within an order of magnitude[2]. Additionally, it requires significant modification to remain accurate in the likely event of impurities of different valence within the metal. This is due to their ability to change the defect concentration by altering the charge balance[2]. The primary value of the theory remains the ability to conceptually understand the process that is occurring during oxide scale formation[2]. There have been many experimentally determined values of k' which combined with knowledge of the significance as described by Wagner's theory provide useful information about the rate of oxide growth[4]. Figure 9 presents examples of measured parabolic rate constants in the form of an Arrhenius plot for a selection of metal oxides[4].

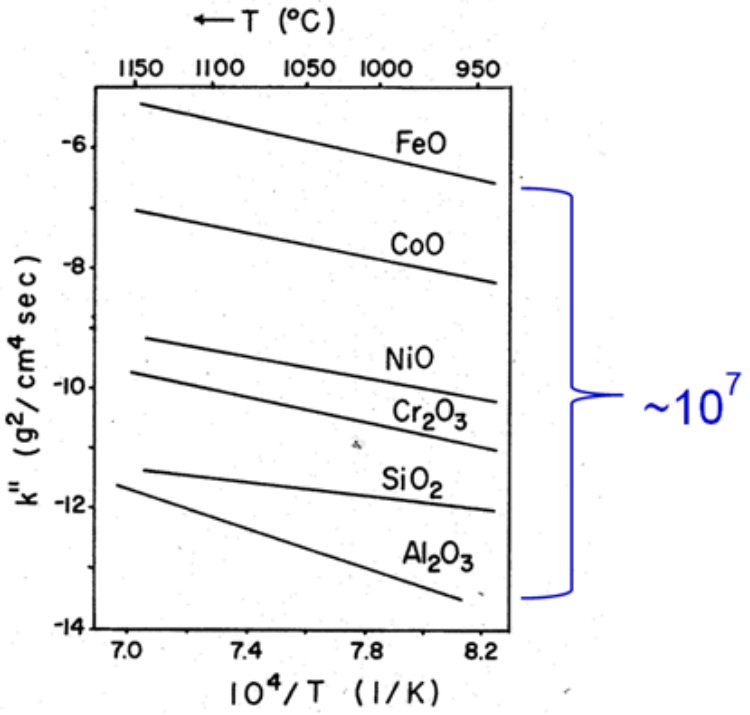

Figure 9: Arrhenius plot of measured parabolic rate constants for a selection of metal oxides[4].

Figure 9 illustrates the slow growing nature of the oxides of Al, Cr, and Si. Combining the measured rate constants from Figure 9 with the Gibbs free energy of formation for the same metal oxides, determined using Equation 6, a thermodynamic map presented as Figure 10 can be generated[4].

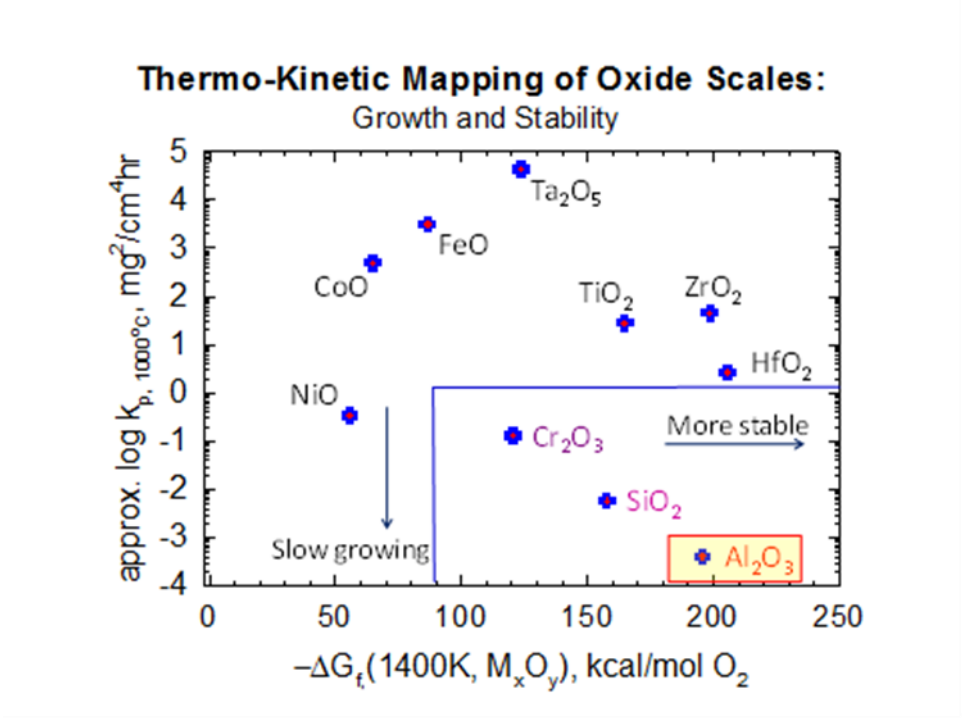

Figure 10: Map of parabolic rate versus free energy of formation[4]

The oxides present within the box in Figure 10, are the commonly used alloying and coating elements Al, Cr, and Si, able to form slow growing oxides, and which are more stable than oxides formed by base elements such as nickel and iron[4]. Combining this knowledge with the fundamental understanding of oxide formation presented in Wagner's theory illustrates why Al, Cr, and Si are so frequently used as alloying or coating elements for applications in high temperature oxidizing environments. Discussion of the specific oxidation characteristics for the pure metal species used in this study are addressed individually in the following sections.

1.7 Logarithmic Rate:

In some cases significant deviations from the parabolic rate law predicted by Wagner's Theory have been observed[6]. In particular, cases when the initial rate of oxidation is very rapid and then quickly reduces to a much lower rate are more accurately described by logarithmic rate laws. The logarithmic rate law function is presented as Equation 51.

$$X = k_{log} \log(t + t_0) + A \qquad \text{Equation 51}$$

In Equation 51, X is equal to the oxide thickness, k_{log} is the logarithmic rate constant, t is total time, t_0 is initial time, and A is a constant. Oxidation behavior best modeled by inverse logarithmic equations have also been observed, however they are beyond the scope of this study.

Logarithmic behavior is typically associated with oxidation at low temperatures, below 400°C[6]. Various theories have been developed to explain logarithmic behavior, however it remains the least-well understood oxidation behavior. The proposed theories include: absorption of reactive gas species, quantum-mechanical tunneling through thin oxide layers, and non-uniform transport across the oxide layer. These theories will be reviewed briefly.

Absorption of reactive gas species, such as $O_{2\,(g)}$, and subsequent nucleation of oxide has been investigated by Benard et al[29]. In this theory the fraction of oxygen absorbed on the surface is referred to as α, which is constant at a given temperature, predicting a constant reaction rate. Following absorbance however, the value of α

becomes greatly reduced in areas where a monolayer of oxide exists. The rate then decreases precipitously following complete coverage of the exposed surface. Alternatively, quantum mechanical tunneling can be used to describe the higher than expected conductivity of thin oxide films[30,31]. Assuming that the transport of electrons is the rate controlling step, the rate would be high as long as the conductivity remains high. The subsequent decrease in rate is attributed to an increase in the oxide layer to a thickness at which quantum tunneling no longer occurs. Non-uniform transport proposes that rapid ionic transport occurs at grain boundaries, dislocations, or pores. The rapid ionic transport is later quenched by grain recrystallization or development of stress which closes pores[32].

1.8 Oxidation of Nickel:

Nickel forms a single oxide, NiO, that is a p-type semiconductor with cation, or metal, deficit[2,6]. Oxidation proceeds by way of outward diffusion of electrons and cations[6]. When Ni is oxidized at temperatures above 900°C the rates are in close agreement with Wagner's theory, however the model performs very poorly for temperatures under 900°C[2]. The primary method of oxide diffusion below 900°C is grain boundary diffusion[2]. The smaller grain sizes of NiO present at lower temperatures result in grain boundary diffusion being the dominant mechanism in place of lattice diffusion[2]. As oxidation progresses NiO recrystallizes to form larger grains which may help to limit the effects of grain boundary diffusion[33]. In addition cold worked Ni, which has deformed (elongated or stretched) grains, has been observed to oxidize more rapidly[6]. The issues arising due to the effects of grain boundary oxidation is the reason many

modern blades in super-alloys are cast as single crystals[7]. At extremely high temperatures 1577-1627°C NiO has been observed to evaporate[34]. Temperatures within this range are beyond the conditions considered in this study.

1.9 Oxidation of Aluminum:

Oxidation of aluminum into thermodynamically stable alumina, specifically α-Al_2O_3, is a rapid process that initiates at room temperature[6]. Following initial scale formation, growth is a slow process which provides oxidation protection for many high temperature alloys[6]. The oxide growth also includes a number of metastable crystalline forms below the 660°C melting point of pure Al including; γ-Al_2O_3, δ-Al_2O_3, θ-Al_2O_3, and κ-Al_2O_3[6].

Progression of alumina oxide forms is rather complex but has been well reviewed[35]. The dominant high temperature form is α-Al_2O_3, however at lower temperatures, 600°C, formation of α-Al_2O_3 on Ni-Al alloys has been proceeded by formation of γ-Al_2O_3. Layers of δ-Al_2O_3 have been observed to form on top of established α-Al_2O_3 layers in Fe-Al and Pt-Al alloys. The θ-Al_2O_3 form has been identified as a potential transition form existing during conversion of γ-Al_2O_3 into α-Al_2O_3. In the presence of H_2O vapor, both the formation of alumina hydride species and depletion of alumina scale has been observed[4,35–37]. The lack of any H_2O within the gas mixture used in this study means hydride formation and volatility are unlikely to occur.

1.10 Oxidation of Chromium:

Oxidation of chromium results in the formation of a single oxide Cr_2O_3, which is an important protective oxide in many applications[6]. However, some issues with Cr_2O_3 as a protective oxide have been observed. Under the conditions of very high oxygen partial pressure Cr_2O_3 becomes volatile as CrO_3 gas[6]. High partial pressures of oxygen are unlikely to occur in post combustion environments like those considered in this study. Additionally Cr_2O_3 scales are known to more frequently deform, buckle, and form cracks from compressive stress than other protective scales[6]. This is because the scale growth is maintained by both inward diffusion of anions and outward diffusion of cations[6]. The inward movement of anions has been found to occur largely along grain boundaries[6].

1.11 Oxidation of Silicon:

Oxidation of elemental Si into SiO_2 is a slow process which results in stable amorphous scale[2]. Conversely to the situation observed with Cr_2O_3, SiO_2 is observed to exhibit volatility in the instance of low oxygen partial pressure[6]. Silicon volatility is observed to occur through the diffusion of SiO_2 gas which can deposit is nanofibers on the oxide surface or evaporate as smoke[6,38]. Oxidation studies of Si under oxygen partial pressures closer to ambient have found the rates to be in close agreement with predictions made by Wagner's theory[6].

1.12 Stress-strain:

Examination of formed oxide morphology often reveals the presence of stress relief phenomena such as cracking, buckling, and spallation[2].These stress relief

mechanisms break up the uniformity of oxide layers and expose the surface of the alloy or metal to further oxidation. Conceptually speaking compressive stress in oxide layers must be matched by tensile stress generated by the underlying substrate[2]. The stress present in these oxide-substrate systems are developed either during oxidation or temperature change[2].

During oxidation, changes in the oxide volume (V_{ox}) in relation to the changes in metal substrate (V_M) volume result in stress which must be relieved if the shape of the substrate remains fixed[2]. The Pilling-Bedworth ratio $\frac{V_{ox}}{V_m}$ developed in 1923 describes the relationship between these two volumes when considering the unrealistic scenario that a scale growth is driven only by the inward diffusion of oxygen[39]. Using this assumption Pilling and Bedworth developed Equations 52 and 53 to describe the strain (ε_{ox}) and stress (σ_{ox}) developed by oxide layer growth at the metal-oxide scale boundary.

$$\varepsilon_{ox} = \left[\left(\frac{V_{ox}}{V_M}\right)^{1/3} - 1\right] \qquad \text{Equation 52}$$

$$\sigma_{ox} = \frac{-E_{ox}}{1-\nu_P}\varepsilon_{ox} \qquad \text{Equation 53}$$

In Equation 53 E_{ox} is the elastic modulus and ν_P is Poisson's ratio[40]. If scale growth was to occur only at the metal-oxide scale boundary a compressive force would be generated on the oxide layer[2]. Conversely, if growth occurred only at the oxide-gas interface then no stress would be introduced to the oxide layer[2]. As previously discussed, however, scale growth occurs due to diffusion of both oxygen and metal ions, for this reason the

Pilling-Bedworth ratio is useful only for conceptual understanding of the origin of stress within the oxide layer[2,6].

In addition to the growth of the scale growth due to diffusion through the continuous oxide layer, grain boundaries and cracks allow access to scale forming gasses[2]. As scale growth occurs within the boundaries and cracks at differing rates it places a lateral stress on the oxide layer[2]. Restricting analysis to oxide growth at the boundary layers and assuming that the grain size is much smaller than the thickness and elastic behavior the stress produced is modeled by Equation 54[41].

$$\sigma_{ox} = \frac{4G_{ox}d_i}{2\delta(1-2\nu_P)} \qquad \text{Equation 54}$$

In Equation 53, G_{ox} is the shear modulus of the oxide and d_i is equal to the width of the oxide growth within the grain boundary[2]. If the stress is sufficiently large it could result in the development of stress relief mechanisms in the oxide such as buckling or delamination of the scale.

Stresses that develop during temperature change arise due to differences in the coefficients of thermal expansion (α) between metals and their corresponding oxides[2]. Thermal expansion coefficients for some relevant materials are listed in Table 2.

Table 2: A list of relevant coefficients of thermal expansion

Material	**10^{-6} α(K^{-1})**	**T(°C)**
Ni	17.6	0-1000[42]
NiO	17.1	20-1000[42]
Cr	9.5	0-1000[42]
Cr_2O_3	7.3	100-1000[42]
Cr_2O_3	8.5	400-800[43]
α-Al_2O_3 (single x1)	5.1-9.8	28-1165[44]
α-SiO_2	2.9-5.8	25-850[45]

If elastic behavior is assumed then the stress on the oxide scale can be described by Equation 55[2].

$$\sigma_{ox} = \frac{-E_{ox}\Delta T(\alpha_M - \alpha_{ox})}{[(E_{ox}/E_M)(X_{ox}/X_M)](1-\nu_P^M)+(1-\nu_P^{ox})} \qquad \text{Equation 55}$$

Equation 55 can be approximated for thin scales on thick substrates as Equation 56[2]

$$\sigma_{ox} \frac{=-E_{ox}\Delta T(\alpha_M - \alpha_{ox})}{1-\nu_P^{ox}} \qquad \text{Equation 56}$$

In most cases however the oxide layer does not follow an elastic behavior and various stress relief mechanisms are observed[2]. These mechanisms include low temperature elastic deformation by dislocation, and by high temperature creep[2]. In cases where stress becomes too large to be relieved by plastic deformation, delamination of the oxide scale, or separation and ejection of oxide scale, a process called spallation, can occur[2]. In the case of applied coatings, spallation can rapidly deplete coating elements and expose the underlying substrate to oxidation.

1.13 Hot Corrosion:

The atmosphere of post combustion turbine engines often contain corrosive contaminants generated during fuel combustion, such as ash, or ingested from the atmosphere, such as vanadium and sodium sulfate[2,46]. The formation of two well-known combustion products can be describe by Equation 57[1].

$$C_xH_y + nO_2 \rightarrow aCO_2 + bH_2O \qquad \text{Equation 57}$$
$$a = x; b = \left(\frac{y}{2}\right); n = x + \left(\frac{y}{4}\right)$$

Other pollutants present in the exhaust include; oxidized carbon and nitrogen species as well as some unburned fuel, also termed unburned hydrocarbons (UHC)[1]. Any sulfur present within the fuel will also be oxidized into SO_x species, the most common being sulfur dioxide (SO_2) gas. These contaminates can form molten alkali salts, such as sodium sulfate (Na_2SO_4),[6,7,46–49]. Sodium sulfate is supplied through oxidation of $SO_{2\,(g)}$ into sulfur trioxide ($SO_{3\,(g)}$) and subsequent reaction of $SO_{3\,(g)}$ with sodium and water[50]. The sodium for this reaction can be supplied by sodium chloride (NaCl) ingested by the compressor, The subsequent formation of Na_2SO_4 is described in Equation 58[2].

$$SO_{3\,(g)} + H_2O + 2NaCl = Na_2SO_4 + 2HCl \qquad \text{Equation 58}$$

Following formation, this compound often condenses on surfaces downstream of the combustion chamber[50]. Condensation of Na_2SO_4 on components such as turbine blades has been observed to alter the behavior and formation of oxide layers, resulting in rapid corrosion of exposed materials [50]. This observed surface deposit induced accelerated high temperature corrosion has been termed “hot corrosion” [6,7,47]. A

schematic presenting the effects on rate of hot corrosion phenomena relative to purely oxidation based corrosion is presented in Figure 11; reasons for the two distinct types of hot corrosion described in Figure 11 will be discussed at length later.

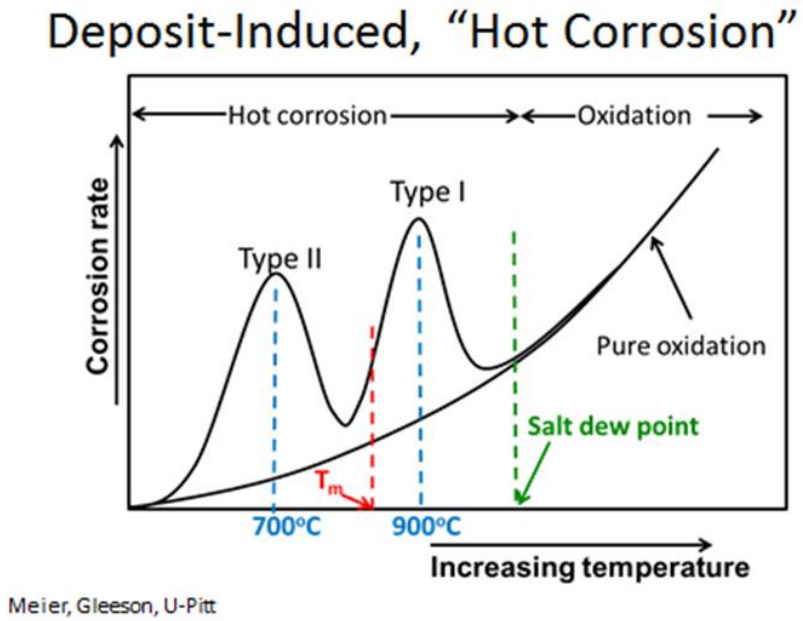

Figure 11: The rate enhancing effects of hot corrosion relative to purely oxidative corrosion effects.

Due to the high operating temperatures used in modern turbines, often in excess of the melting point of pure Na_2SO_4, the deposits frequently remain molten after condensation[2]. The molten salts then act as ionic melts leading to an anodic corrosion process similar to the corrosion of metal in aerated water, described for the general case in Equation 59[2].

$$M = M^{n+} + ne^- \qquad \text{Equation 59}$$

The reaction of the salt species is described by Equations 60 and 61.

$$S_2O_7^{2-} + e^- = SO_4^{2-} + SO_3^- \qquad \text{Equation 60}$$

$$SO_3^- + e^- = SO_2 + O^{2-}$$ Equation 61

Where disulfate ($S_2O_7^{2-}$) is produced through the dissolution of $SO_{3\,(g)}$ from the atmosphere as described by Equation 62[2].

$$SO_3 + SO_4^{2-} = S_2O_7^{2-}$$ Equation 62

Based upon the reactants described in Equations 59-62 it is possible to describe the necessary environment for hot corrosion to occur. Figure 12 displays the components which play a role in hot corrosion; a molten deposit of Na_2SO_4 on top of the developed protective oxide layer and the atmosphere containing oxygen and frequently gaseous sulfur dioxide and sulfur trioxide above the deposit[46].

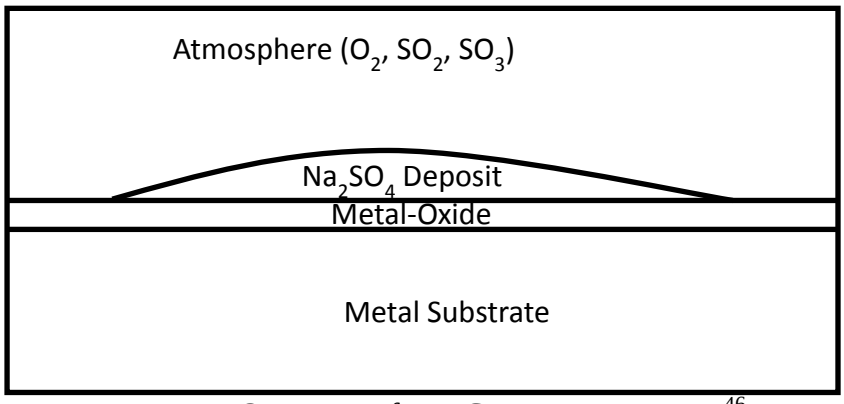

Figure 12: Overview of Hot Corrosion Reactants[46]

The reaction within the molten salt deposit from Figure 12 is typically written as Equation 63[2,46].

$$Na_2SO_4 = Na_2O + SO_{3(g)}$$ Equation 63

The equilibrium expression can be written, using the free energy of formation from Equation 63 ($-\Delta G^{\circ}_{63}$), as Equation 64[2].

$$\log a_{Na_2O} + \log p_{SO_3} = -\Delta G^{\circ}_{62}/2.303RT \qquad \text{Equation 64}$$

A clear analogy is comparing the reaction in Equation 63 to an acid base reaction where Na_2O is the base and SO_3 is the acid[6]. In this scenario the p_{OH} of an aqueous solutions is analogous to the $-\log a_{Na_2O}$ term from Equation 64 and is defined as the melt basicity[2].

The phase diagram for the Na-S-O system can be calculated using standard free energy data, as displayed in Figure 13 for the system at 900°C[51].

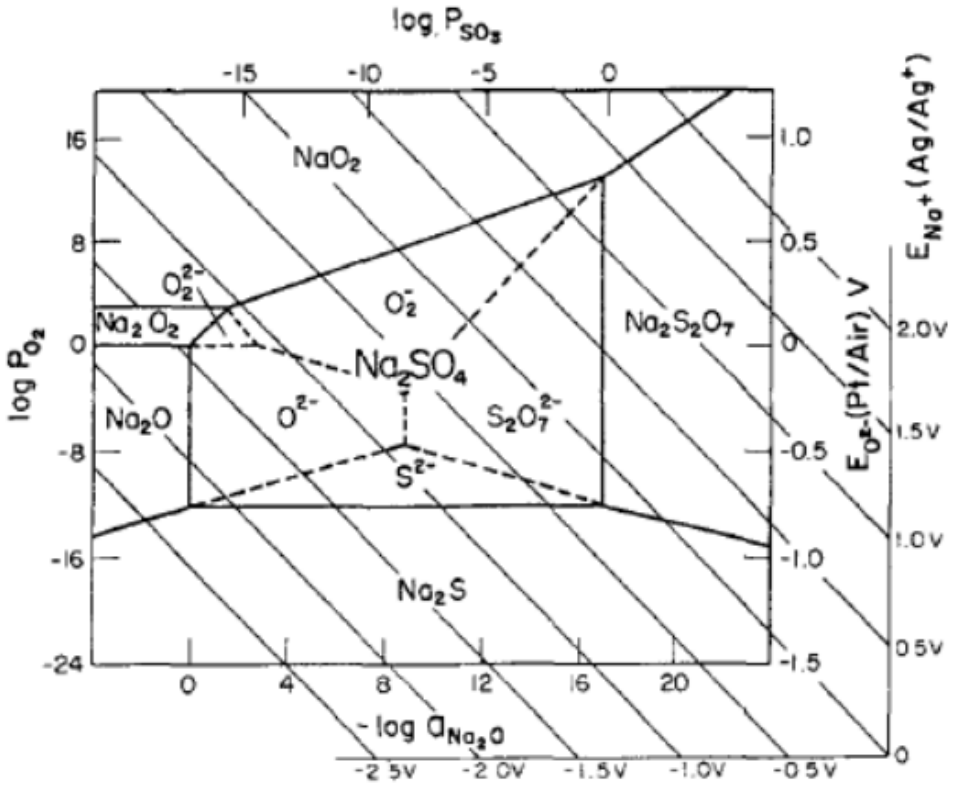

Figure 13: Phase diagram for Na-S-O system at 900°C with electrochemical data[52]

Figure 13 illustrates that there is a large stability zone in which liquid Na_2SO_4 can exist, allowing for the development of relatively large gradients in basicity[2]. The development of gradients will be demonstrated to be necessary for hot corrosion to occur[2,6].

The process by which dissolution of oxide species occurs depends on the previously defined melt basicity[2,6]. Two different types of oxide dissolution have been observed. The first, basic dissolution, occurs for Ni when Na_2O ionizes NiO through donation of electrons generating NiO_2^{2-} as described by Equations 65-67[6].

$$NiO + Na_2O = 2Na^+ + NiO_2^{2-} \quad \text{Equation 65}$$

$$NiO + O^{2-} = NiO_2^{2-} \quad \text{Equation 66}$$

$$NiO + Na_2SO_4 = 2Na^+ + NiO_2^{2-} + SO_3 \quad \text{Equation 67}$$

Conversely acidic dissolution occurs when SO_3 further oxidizes NiO to yield the soluble Ni cation Ni^{2+}, described by Equations 68-70[6].

$$NiO + SO_3 = Ni^{2+} + SO_4^{2-} \quad \text{Equation 68}$$

$$NiO = Ni^{2+} + O^{2-} \quad \text{Equation 69}$$

$$NiO + Na_2SO_4 = Ni^{2+} + SO_4^{2-} + Na_2O \quad \text{Equation 70}$$

The equilibrium expression to describe the dependence of the activity of nickel in solution during basic dissolution is described by Equation 71[2].

$$\frac{\partial \log a_{NiO_2^{2-}}}{-\partial \log a_{Na_2O}} \Big|_{p_{O_2}} = -\frac{1}{2} \quad \text{Equation 71}$$

The corresponding expression for acid dissolution is presented as Equation 72[2].

$$\frac{\partial \log a_{Ni^{2+}}}{-\partial \log a_{Na_2O}} \Big|_{p_{O_2}} = 1 \quad \text{Equation 72}$$

Mechanisms and rates of degradation for various elements during hot corrosion have been extensively studied[6,46,47,50,53]. Solubility curves and phase diagrams for NiO,

Al_2O_3, Cr_2O_3, and SiO_2 in Na_2SO_4 were developed by Rapp, et al, and Zhang relating oxide solubility to melt basicity at 900°C[54–57]. The findings of the solubility studies, along with a description of melt dependence on the partial pressure of $SO_{3(g)}$ are summarized in Figure 14[54–57].

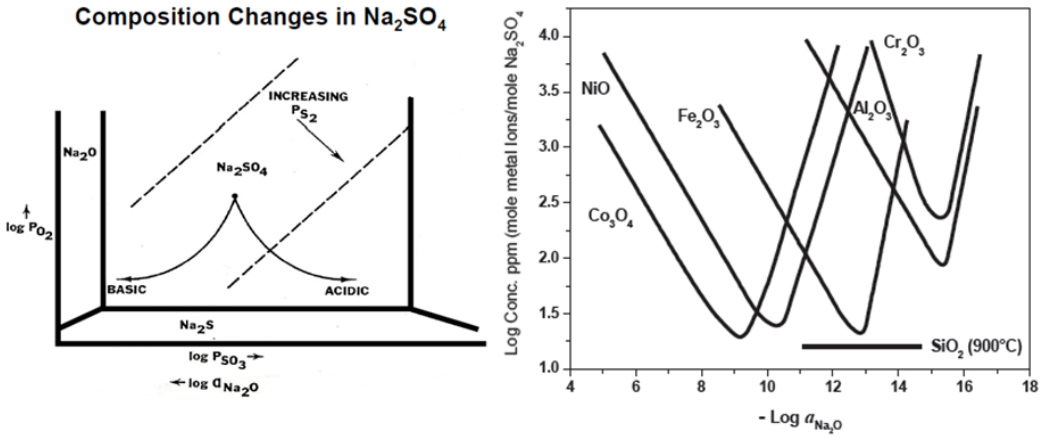

Figure 14: Summary of results from solubility studies carried out by Rapp et al and Zhang[54–57].

Results indicate that the dissolution of NiO, Al_2O_3, and Cr_2O_3 shows strong dependence upon melt basicity while SiO_2 does not[54–57]. This result was attributed to the observation that SiO_2 does not form a ternary solution, dissolution of SiO_2 instead proceeds through physical rather than chemical processes[57].

If dissolution of the oxide was the only step then saturation of the salt deposit at the oxide-deposit interface would occur limiting the effects of hot corrosion to a short time frame[2]. It has been determined that hot corrosion is largely due to the dissolution and re-deposition of the protective oxide layer in a non-protective fashion throughout the salt deposit as described by Figure 15[2,6,47].

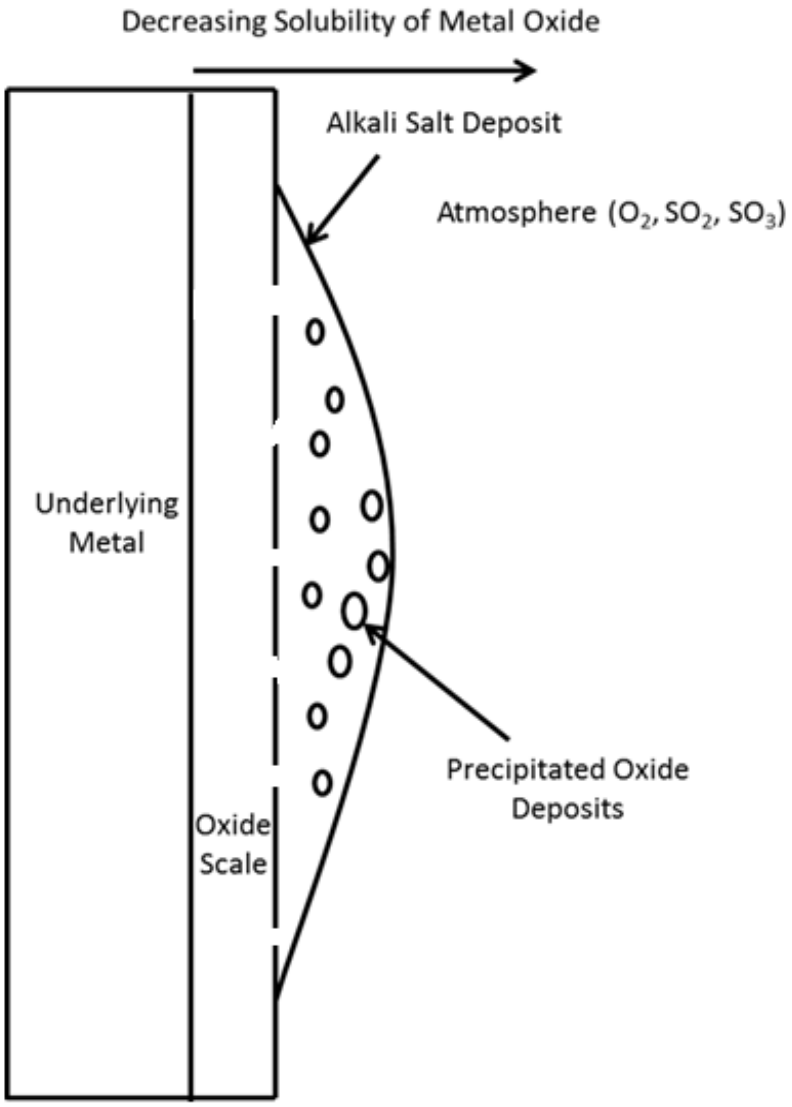

Figure 15: Dissolution and re-deposition of oxide through a molten alkali salt deposit[47]

In Figure 15 the spheres describe precipitated metal oxides which have diffused through the salt deposit and deposited in a non-continuous fashion, allowing increased access by gasses. Access of reactive gas means that ionic diffusion through the scale is no longer is the limiting factor for oxide formation, resulting in a further increased rate of oxidation[2,6].

Diffusion or fluxing of the dissolved oxide species occurs when an activity gradient is maintained throughout the melt. This is true if the solubility decreases only as the distance from the oxide-deposit interface increases[58]. Oxide continues precipitating as distance from the oxide-melt interface increases maintaining a negative gradient as described by Equation 73[2].

$$\frac{\partial C_{M^+}}{\partial x} < 0 \qquad \text{Equation 73}$$

The negative gradient is known as the Rapp-Goto Criterion and is a requirement for self-sustaining hot corrosion to occur[59].

Basic fluxing occurs when the melt comes into contact with the underlying substrate and exposes the metal to a liquid with low oxygen activity and a high sulfur activity[2]. The high sulfur activity of the melt at this metal-melt interface leads to sulfidation of the metal. The removal of sulfur from the melt increases the basicity as described by Equation 63[2]. At the melt-gas interface uptake of $SO_{3\,(g)}$ per Equation 64 leads to increased acidity[2]. The result is a negative gradient in Na_2O and therefore metal cations (C_{M^+}), satisfying the Rapp-Goto Criterion. Additionally the gradient in SO_3 can result in an inward diffusion and continued sulfidation[2]. Evidence of formed metal sulfides can indicate that such a process is occurring. This process has been actively observed for pure nickel through electrochemical monitoring[60].

Two distinct types of acidic flux are observed for hot corrosion[6]. The first is alloy induced acidic fluxing, which occurs when the melt is more acidic at the metal-melt interface than at the melt-gas interface[2]. This could be the case when dissolved species are strongly acidic, for example the common alloy components molybdenum and

tungsten produce strongly acidic oxides[2]. The Rapp-Goto criterion in this case is dependent upon low concentration of $SO_{3(g)}$ in the environment and evaporation of the acidic species at the melt-gas interface[2,6]. The second type is referred to as gas phase acidic flux, which occurs at high $SO_{3(g)}$ partial pressures[6]. Dissolution of $SO_{3(g)}$ into the salt melt occurs via the reaction described by Equation 10[6]. Flux of metal cations then occurs due to reaction of cationic species with gas at the melt-gas interface to form either oxides or sulfates[6]. The precipitation of these species at the melt-gas interface creates the negative gradient necessary to satisfy the Rapp-Goto criterion.

Both of the presented scenarios for the flux of material are highly idealized. It is unlikely that during operation that the deposit chemistry will remain within this idealized state. Also it is probable that as the molten salt progresses access to the atmosphere will become limited resulting in less $SO_{3(g)}$ being available for dissolution in the melt[2]. Finally, these models do not account for the formation of sulfide species which can significantly alter the stability of the substrate at the metal-melt interface[2].

1.14 Type I and Type II Hot Corrosion:

Temperature, composition of the gas phase, and $SO_{3(g)}$ content also play significant roles in hot corrosion. Specifically, two distinct types of hot corrosion have been identified, Figure 10, which are categorized by temperature range. Type I, or high temperature, hot corrosion (HTHC) occurs above the melting temperature of pure sodium sulfate (884°C) and proceeds by basic or acidic dissolution of oxide and subsequent flux of material as described above. Type II or low temperature hot corrosion (LTHC) occurs

between the temperatures of 620°C and 750°C and requires the presence of excess $SO_{2(g)}$ in the atmosphere[6,7,61]. In this case, the $SO_{2(g)} - SO_{3(g)}$ gas not only to provide the acidic component necessary for gas-phase acidic flux, but also induces the formation of transition metal sulfates (MSO_4)[6]. The formation of these sulfates occurs in significantly reduced partial pressures of $SO_{3(g)}$ at lower temperatures, as demonstrated for Al_2O_3 in Figure 16[53].

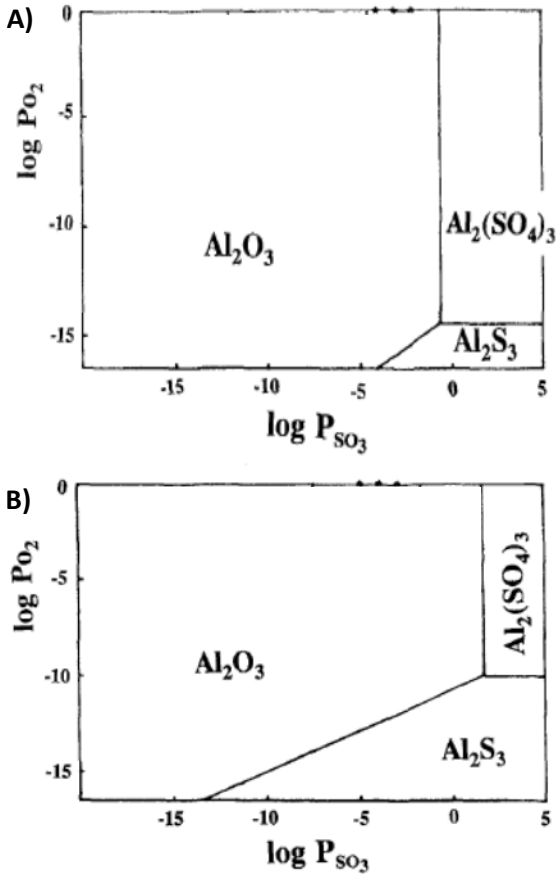

Figure 16: Stability diagram for alumina in SO_2-SO_3 atmosphere at 700°C (A) and at 900°C (B)[53]

As illustrated in Figure 16 the formation of $Al_2(SO_4)_2$ occurs at lower partial pressures of $SO_{3(g)}$ at 700°C than it does at 900°C. The observed accelerated corrosion at lower temperatures is unique to the chemistry of LTHC.

Formation of sulfates is requisite because LTHC depends largely on the ability of the salt deposit to form sodium sulfate-transition metal sulfate eutectics ($Na_2SO_4 - MSO_4$), or ternary melts, with the surface elements of an alloy[2,6,61]. In nickel based alloys a sodium sulfate-nickel sulfate eutectic with a melting temperature of 671°C has been observed, consistent with predictions from standard free energy data[61]. The phase diagram, originally developed by K.A. Bol'shakov and P.I. Fedorov, depicting a zone of stability for molten metal-metal sulfate for the $Na_2SO_4 - NiSO_4$ system is presented in Figure 17[62].

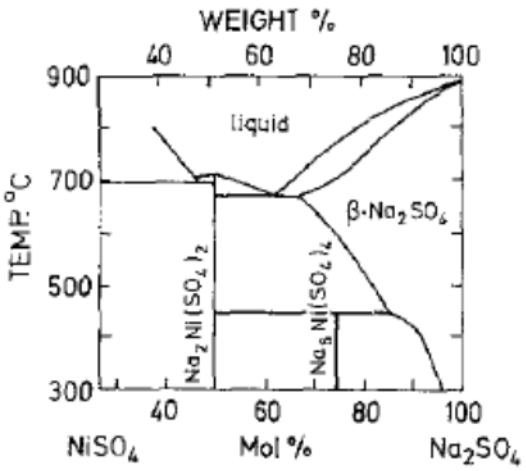

Figure 17: phase diagram for the $\boldsymbol{Na_2SO_4 - NiSO_4}$ system

It has also been observed that difficulties in forming Al_2O_3 and Cr_2O_3 protective coatings occur under hot corrosion inducting conditions, an effect attributed to the formation of

the described metal sulfides [2,6,48,53,63]. However, coatings containing high levels of Cr, Al, or both metals appear to offer corrosion protection to materials that are subject to hot corrosion[2]. A brief summary of the oxidation and hot corrosion characteristics for the coating metal oxides of interest to this thesis are presented in Table 3[4].

Table 3: Summary of oxidation and hot corrosion characteristics of relevant metal oxides[4]

	Alumina (Al_2O_3)	**Chromia (Cr_2O_3)**	**Silica (SiO_2)**
Rate controlling	Oxygen grain boundary dominates	Duplex, g.b. Cr and O	Neutral oxygen permeation
Rate dependence on oxygen pressure	None observed*	None observed *	$[P(O2)]^1$
Activation energy	380 kJ/mole for g.b. oxygen	244 kJ/mole for undoped 263 kJ/mole for Y-doped	Low—119 kJ/mol
Dopant/Impurity effects	Low for growth; high for adhesion	Growth reduced 10x by Y; high for adhesion	Very sensitive
Water vapor effects	Minor, transition aluminas transform faster	Major, volatility	Moderate, growth and volatility
Salt corrosion	Acidic fluxing to Al^{+3}; Basic fluxing to $Al_2O_4^{-2}$	Acidic fluxing to Cr^{+3}; Basic fluxing to $Cr_2O_4^{-2}$	Basic Fluxing to SiO_3^{-2}
	* predicted diffusivity dependence:	$P(O_2)^{-1/6}$ at metal interface (oxygen) $P(O_2)^{3/16}$ at gas surface (aluminum)	

Regardless of type, hot corrosion demonstrates two distinct stages of attack: an initiation stage during which the alloys are protected by an oxide scale and a propagation stage during which the oxide scale offers greatly reduced protection[6,46,61]. The initiation stage begins after the deposit either becomes molten or condenses on the surface. During

initiation, oxygen from the melt as well as that absorbed during the dissolution of $SO_{3(g)}$ causes formation of oxide which may behave similarly to that formed under normal conditions[6]. Melt basicity is then altered according to one or more mechanisms[6]. Following development of the negative gradient proposed by Rapp and Goto the propagation phase begins during which, metal corrosion is greatly enhanced[2,6,46].

1.15 Motivation:

Increased understanding of interactions between sulfur, reactive elements, and the metal oxide interface during hot corrosion are necessary[2]. Standard methods for evaluating materials in hot corrosion environments are currently being formalized, per ISO working draft 17224[64]. A novel approach to the study of alloy and coating components in high temperature environments may enhance fundamental understanding of component behavior in these environments. Additionally, the ability to replicate the behavior of super alloys in high temperature environments through application of thin overlay type coatings, on an inexpensive substrate, could lead to significant reductions in material costs. The described processes provide a foundation for the development of single element and combinatorial coatings as well as a high throughput analysis methodology for evaluating coating performance. Specifically, the methods provide a means for studying coating- substrate inter-diffusion, oxide formation, and intermetallic species formation occurring during high temperature oxidation and hot corrosion of coated substrates.

2.0 MATERIALS AND METHODS:

In this study, model systems of post combustion turbine engine components, most similar to overlay coatings on Ni based alloys, were created consisting of Ni-201 with single element one micron (1 μm) thick coatings of Al, Cr, or Si using magnetron sputtering process. These coated samples were then exposed to stagnant lab air and a flowing atmosphere consisting of 2 ppm SO_2/air at 700°C to model the conditions associated with high temperature oxidation corrosion and LTHC. Additionally, samples were exposed to temperatures of 900°C in stagnant lab air for comparison to investigate HTHC. Samples were then evaluated using mass gain analysis, surface morphology investigation, and various chemical analyses in order to evaluate the response of each model system to environment.

2.1 Coating Process:

The Ni-201 substrate used in this study consisted of sheet metal 0.08 cm thick with the weight percent composition presented in Table 4.

Table 4: Ni-201 composition by weight percent [65].

Element	Fe	Si	Mn	Cu	C	S	Ni
Weight Percent	0.05	0.05	0.02	0.02	0.02	0.002	Balance

The substrate sheet was laser cut into 2 x 1 cm specimen tabs. The cut sheets were then degreased and cleaned with isopropanol.

The cleaned substrate sheets were placed in an Angstrom Engineering Sputtering PVD System and sputter cleaned using $Ar_{(g)}$ at 100 W for 20 seconds under vacuum.

Thin film elemental coatings were deposited on one side of the sheets using a DC source for Al and RF sources for Cr and Si according to the parameters described in Table 5.

Table 5: Parameters for single element deposition of thickness 1 μm in Angstrom Engineering PVD sputter system.

Element	Power (watts)	Substrate Height (cm)	Pressure (mT)	Time (minutes)
Al	290	130	5	210
Cr	400	130	10	123
Si	400	130	5	180

Additional sheets were left uncoated for comparison. Following the coating process, bare Ni-201 samples are referred to as ARNi, Al coated samples as Ni + Al, Cr coated as Ni + Cr, and Si coated as Ni + Si.

2.2 Salt Deposition Process:

Sample tabs were removed from the sheet following coating, then heated to 100°C, cooled to ambient temperature, and weighed using a Sartorius Model LE26P balance with accuracy of $\pm 0.002\ mg$, Figure 18.

Figure 18: Sartorius Model LE26P balance

Samples which were to have a salt deposit added were then placed inside a glass beaker and heated to approximately 100°C on a hot plate. During heating 0.2 mL of a solution containing 1.8 grams of reagent grade Na_2SO_4 per 200 mL of deionized H_2O was added drop wise via syringe onto the sample surfaces. The water rapidly evaporated leaving behind a $\sim 1 \frac{mg}{cm^2}$ Na_2SO_4 deposit similarly to processes used in other studies[53,64]. A sample of the resultant salt deposit on a sample coupon is presented in Figure 19.

Figure 19: Photo of a sample coupon with a deposit of $\sim 1 \frac{\mathrm{mg}}{\mathrm{cm}^2}$ of Na_2SO_4.

2.3 Stagnant Air Oxidation:

Following the addition of the salt deposit, samples are once again heated and weighed. The samples were then placed coated side up on an alumina support and heated to 700°C or 900°C and held isothermally in Barnstead Thermolyne 47900 bench-top furnaces according to Figure 20. Samples were oxidized in this manner incrementally with gravimetric analysis carried out using the Sartorius balance at intervals of 1, 4, 10, 20, 50, and 100 hours. Three iterations of the experiments were carried out and the mean mass gain calculated for the three trials.

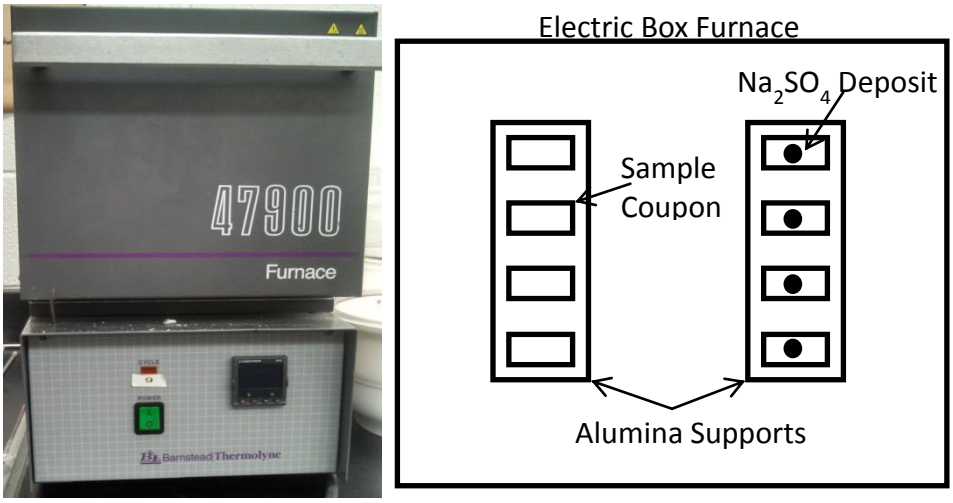

Figure 20: Image of the box furnaces (left) and Plan, top down, view of experimental apparatus (right).

2.4 Mixed Air/SO_2 Oxidation:

Samples to be oxidized in an atmosphere consisting of an Air/2 ppm SO_2 mixture were treated identically to those for stagnant air oxidation prior to exposure. The alumina supports were then placed in quartz glass crucibles and inserted into either the MTI Corporation GSL1100X or Thermo Scientific Lindberg Blue M tube furnace as illustrated by Figure 21. Platinum (Pt) mesh was sandwiched between quartz wool and added to a quartz crucible which was then slid into the quartz tube. The Pt catalyst catalyzes the conversion of sulfur dioxide ($SO_{2\,(g)}$) to sulfur trioxide ($SO_{3\,(g)}$), which is an active species in hot corrosion reactions[6]. An additional quartz wool flow restrictor was placed at the end of the quartz tube to promote turbulent flow and thermal insulation. Gravimetric analysis was carried out at time intervals identical to those described for stagnant atmosphere exposures.

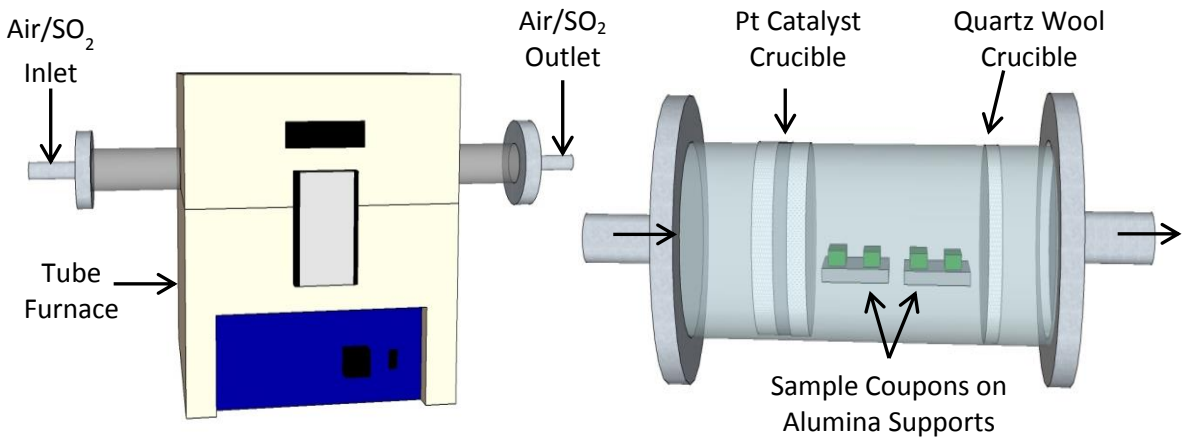

Figure 21: Schematic of the tube furnace with quartz tube in place (left) and the tube outside of the furnace including samples and Pt catalyst containing crucible (right).

As discussed previously a potential source of error for mass gain analysis is outgassing of oxide species. The experiments in this study were performed at ambient p_{O2}, with no introduced H_2O vapor, and at temperatures significantly below those known to generate these effects, therefore the negative bias generated by outgassing of coating materials is likely to be negligible.

2.5 Rate Constants:

Linearization of the gravimetric data provided a means to calculate parabolic rate constants for the coatings under experimental conditions. This was accomplished through the use of Equation 29. In this case the oxide thickness, x, from Equation 29 is estimated as the mass gain per surface area, $\frac{\Delta m}{cm^2}$. This value is calculated from the known dimensions and mass of samples prior to exposure. Equation 74 is produced by substituting the calculated mass gain per surface area values into Equation 29.

$$\left(\frac{\Delta m}{cm^2}\right)^2 = 2k't \qquad \text{Equation 74}$$

Plotting Equation 74 for each sample as $y = mx$ where m is equal to k' and time, t, is equal to x, and preforming a linear regression with the intercept set to the origin provides a simple means for calculating the value of k', with units of $\left[\frac{mg^2}{cm^4 hr}\right]$, over the course of oxidation.

In the case where a parabolic rate does not accurately reflect the progression of oxidation, a logarithmic regression can be used on the plot of mass gain per area, $\frac{\Delta m}{cm^2}$, vs time to generate Equation 75.

$$X = k_{log} \log(t + t_0) + A \qquad \text{Equation 75}$$

Using Equation 75 generated by regression, the logarithmic rate constant, with units of $\left[\frac{mg}{cm^2 \log hr}\right]$, is determined directly.

2.6 Surface Morphology and Energy Dispersive X-Ray Spectroscopy:

Sample surface morphology was assessed using a Zeiss SUPRA 55VP Field Emission Scanning Electron Microscope (FEM), Figure 22.

Figure 22: Zeiss SUPRA 55VP FEM[66]

Images were used to investigate differences in morphology between surface areas covered in Na_2SO_4 deposits and those without a deposit. Special attention was paid to areas that appeared to have undergone stress relief through spallation. Surface chemical analysis was undertaken using the energy dispersive x-ray spectroscopy (EDS) capability of the FEM. Data generated was used to evaluate oxide and intermetallic compound formation at the coating-deposit interface as well as access metal ion flux into the Na_2SO_4 deposits.

2.7 X-ray Diffraction:

Further surface phase composition analysis was undertaken using the SCINTAG X1 Diffraction Spectrometer (XRD) with a 2θ geometry, Figure 23.

Figure 23: SCINTAG X1 Diffraction Spectrometer[67]

Analysis was carried out using thin film techniques with a beam penetrating depth of between 1 and 5 microns. This allows for more accurate characterization of the phases present within the substrate inter-diffusion zone. The angle range used for this analysis was between 10 and 75 degrees. The peaks on the patterns generated were annotated, using the International Center for Diffraction Data (ICDD) database, to denote the present compounds.

2.8 Cross Sections:

Cross sections of Na_2SO_4 deposited and non-deposited samples exposed for 1 and 100 hours for all model environments were prepared using an Allied High Tech Products TECHCUT 4 Precision Sectioning Machine and TECHPREP MultiPrep Polishing System. Samples were then attached to a mount for polishing as displayed in Figure 24.

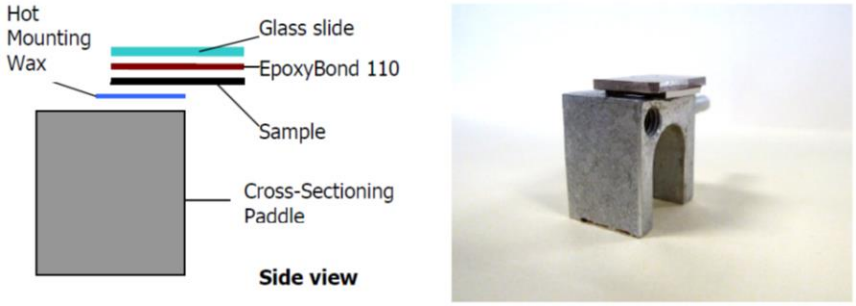

Figure 24: Schematic of the sample mounting process (left) and a photo of a prepared sample mount (right)

Deposited samples were polished using anhydrous lubricants and suspensions to avoid dissolution of Na_2SO_4. The methodology used for polishing was developed in a collaborative effort with Allied High Tech and is outlined in Figure 25[68].

	Step	1	2	3	4	5	6	7
Consumables	Abrasive	600 Grit (P-1200)	9 µm	6 µm	3 µm	1 µm	1 µm	0.25 µm
	Type	SiC	Diamond	Diamond	Diamond	Diamond	Diamond	Diamond
	Carrier	Abrasive Discs	Lapping Film	Lapping Film	Lapping Film	Lapping Film	Alcohol Suspension	Alcohol Suspension
	Polishing Cloth	-	-	-	-	-	White Label	Final A
	Coolant	RedLube	RedLube	RedLube	RedLube	RedLube	RedLube	RedLube
Settings	Platen Speed (RPM) / Direction	150/CCW	150/CCW	120/CCW	80/CCW	50/CCW	150/CCW	150/CCW
	Sample Oscillation	Center to Edge (Speed 1)	Center to Edge (Speed 1)	Center to Edge (Speed 1)	Center to Edge (Speed 1)	Center to Edge (Speed 1)	Center to Edge (Speed 1)	Center to Edge (Speed 1)
	Sample Rotation	Full (speed 1)	Full (speed 1)	Full (speed 1)	Full (speed 1)	Full (speed 1)	Full (speed 8)	Full (speed 8)
	Sample Load	Full	Full	Full	Full	Full	Full	Full
	Time *	As needed	5 min	5 min	5 min	5 min	5 min	3-5 min

* The glass microscope slide used to support the sample was 1.27 mm thick; if a thinner slide is used, it may reduce the grinding and polishing times.

Figure 25: The method used for the polishing of samples developed in collaboration with Allied High Tech[69]

These cross sections were evaluated using line-scan EDS analysis on the FEM. Areas of analysis were selected to focus on ionic diffusion occurring between substrate, coating, and deposit over the course of sample exposure.

2.9 Inductively Coupled Plasma Spectroscopy:

Three sets of samples were deposited with 3 $\frac{mg}{cm^2}$ of Na_2SO_4 and subjected to exposure in stagnant lab air at 700°C and 900°C and in flowing air/$SO_{2\,(g)}$ at 700°C for 10 hours. The larger deposits were used to ensure sufficiently large amounts of metal were present within the deposit to meet the detection limit of the instrument. The deposits were then removed from the coupon using a metal spatula, placed into a 15 mL centrifuge tube, and sent to Energy Laboratories Inc. for analysis by Inductively Coupled Plasma Mass Spectroscopy (ICP-MS) in order to quantitatively measure the flux of metal ions into the Na_2SO_4 deposits. Upon arrival those samples were prepared by Energy lab personal through dissolution in a carrying solution consisting of deionized H_2O and nitric acid. Those samples containing enough metal to make dissolution difficult were digested through heating and addition of hydrochloric acid (HCl).

3.0 RESULTS AND DISCUSSION

3.1 Gravimetric Analysis Data:

Mass gain data for the different gas compositions and temperatures examined in this study are presented and discussed in the following section. This data is presented as an estimate of the oxidation rates for the different sample coatings. Mass gain data for samples oxidized in stagnant lab air at 700°C are presented in Figure 26.

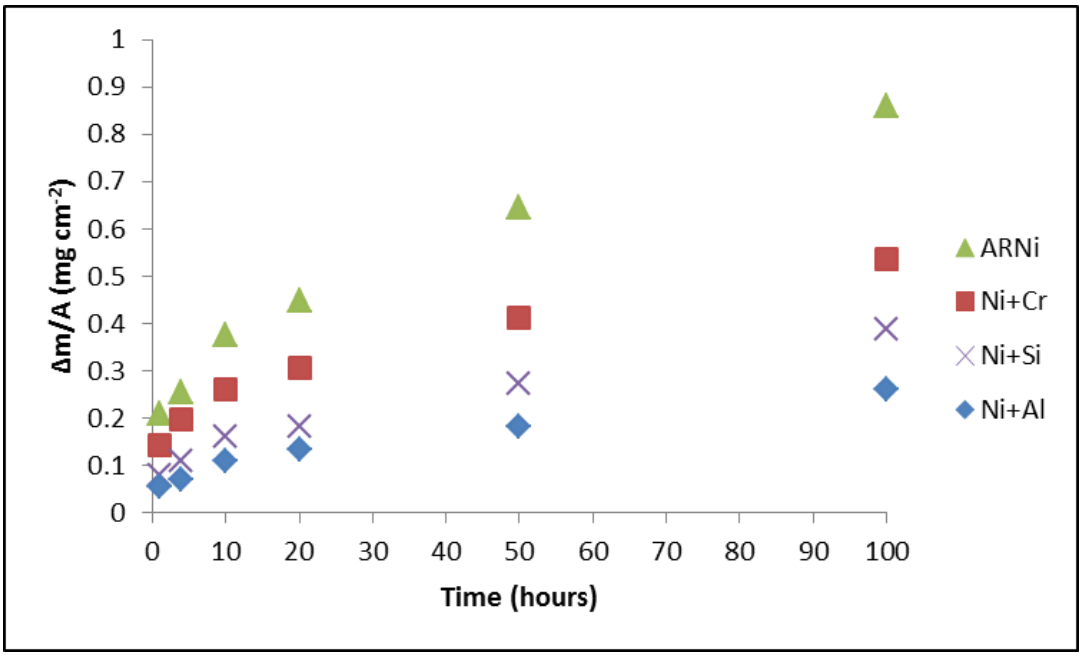

Figure 26: Mass gain per area for samples oxidized in stagnant lab air at 700°C

The mass gain data presented in Figure 26 indicate that the coatings oxidize at significantly different rates in stagnant lab air at 700°C. This data is consistent with the rates of oxidation predicted by kinetics as presented in Figures 9 and 10^4.

Mass gain data for the samples oxidized at 700°C in stagnant lab air with a deposit of Na_2SO_4 is presented in Figure 27.

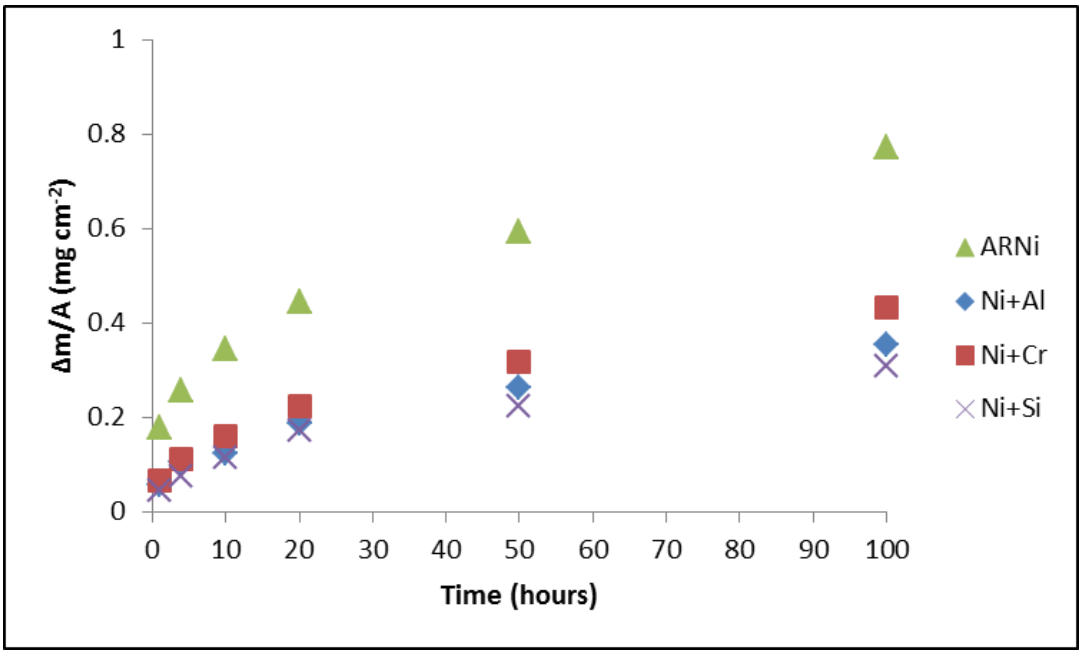

Figure 27: Mass gain data for samples oxidized in stagnant lab air at 700°C with a Na_2SO_4 deposit

The mass gain data indicate that rates of mass gain decreased for all samples in comparison to un-deposited samples at the same temperature. This suggests that the primary effect of the deposit was to limit the amount of oxygen available for the oxidation reaction described by Equation 3. A finding which is consistent with previous studies that indicated necessity of $SO_{3(g)}$ and the subsequent formation of metal sulfate species, for ternary melts to occur[2,6,46,51]. Without the formation of ternary melts gas diffusion is limited by the presence of the solid salt deposit on the surface, thus reducing oxidation rate.

Mass gain data for the samples oxidized in air/2 ppm $SO_{2\,(g)}$ mixture are presented in Figure 28.

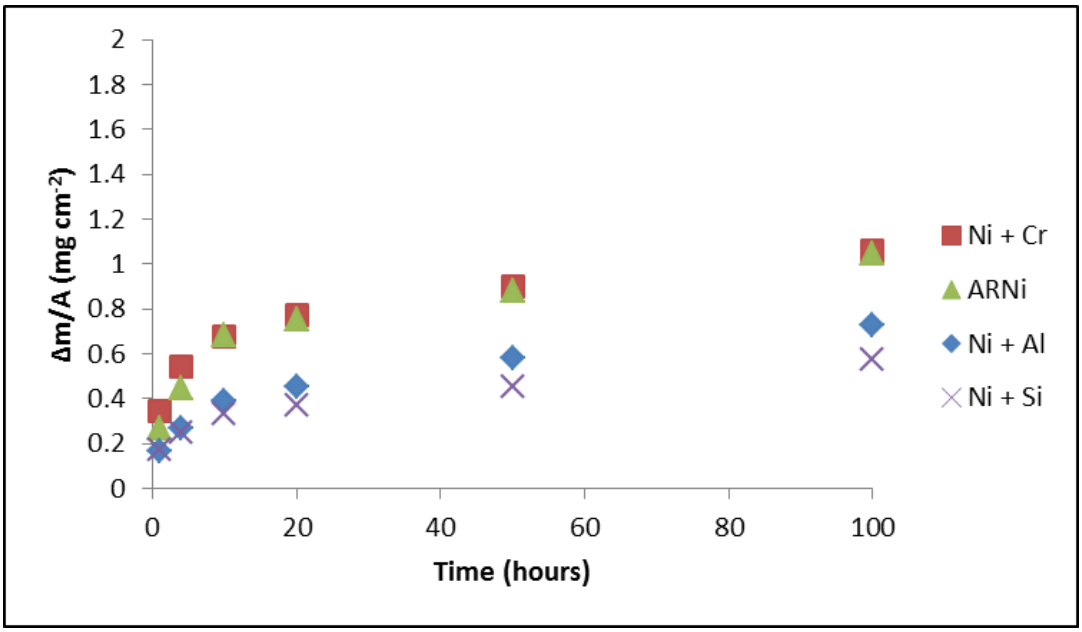

Figure 28: Mass gain data for samples oxidized in air/2 ppm $SO_{2\,(g)}$ at 700°C

Introduction of $SO_{2\,(g)}$ to the oxidation process increased the rate of mass gain for all of the samples. Additionally the results indicated a departure of the relative rates of oxidation for the coating materials from that predicted by kinetics in oxygen only atmosphere. Namely, the predicted order of mass gain seems to be lower than expected for Si in relation to Al. Also the differences between the rates of oxidation for Cr and bare Ni appear negligible, where oxidation kinetic predictions suggest they should be significant. This result suggests that when coupled with sulfidation reactions the characteristics of the coating materials are significantly altered. The presence of sulfur gas species could result in the formation of metal sulfide or sulfate species causing the increases in mass gain and altered order demonstrated in Figure 28. This also implies that the Al coating is particularly suceptible to this type of reaction.

The mass gain data for those samples oxidized in air/2 ppm $SO_{2\,(g)}$ with a deposit of Na_2SO_4 are presented in Figure 29.

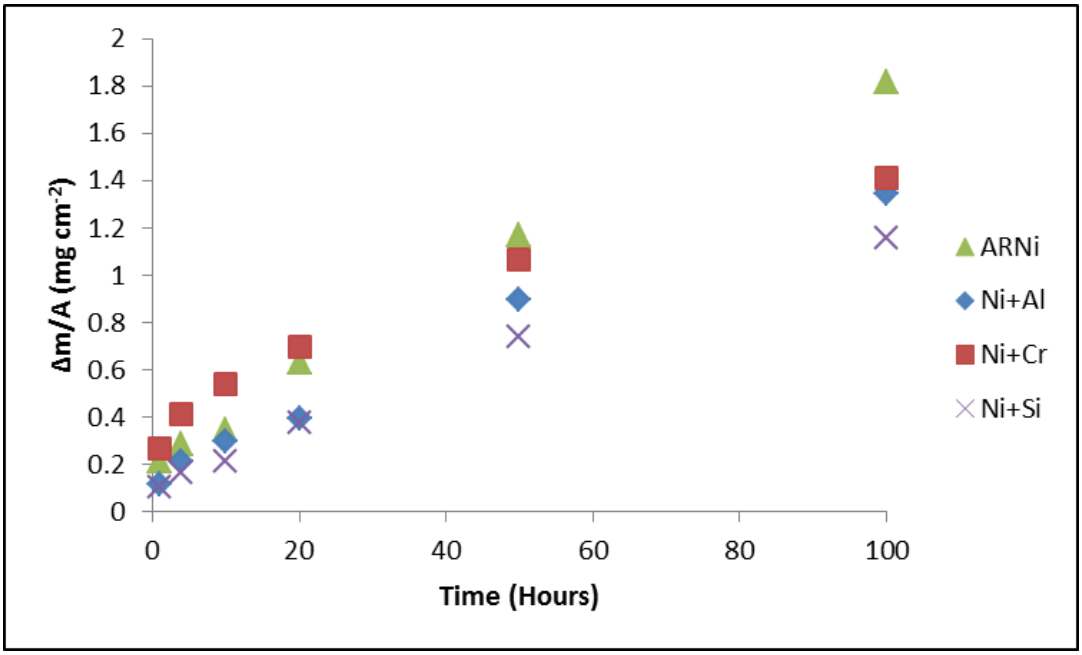

Figure 29: Mass gain data for samples oxidized in air/2 ppm $SO_{2\,(g)}$ at 700°C with a Na_2SO_4 deposit

Results indicate that mass gain again increases significantly in the presence of $SO_{2\,(g)}$. Figure 29 also confirms that the effect is more pronounced for the samples with Na_2SO_4 deposits. This is also consistent with previous findings indicating the necessity of the presence of $SO_{2\,(g)}$ and $SO_{3\,(g)}$ for hot corrosion at 700°C [2,6,20,46,47,53]. The increase in mass gain suggests that the chemistry associated with hot corrosion is occurring. However, further analysis was necessary to confirm the formation of the ternary salt melts that initiate hot corrosion. If these melts are present, $SO_{3\,(g)}$ from the flowing atmosphere is likely to be incorporated into the melt resulting in acidic dissolution and fluxing of metal ions being the dominant reaction occurring[2]. Additonally, reaction of

metal ions with $SO_{3\,(g)}$ and $O_{2\,(g)}$ at the melt-gas interface could maintain the Rapp-Goto concentration gradient necessary for the metal ion flux associated with hot corrosion[2,6,47].

Figure 30 displays the mass gain data for those samples oxidized in stagnant lab air at 900°C.

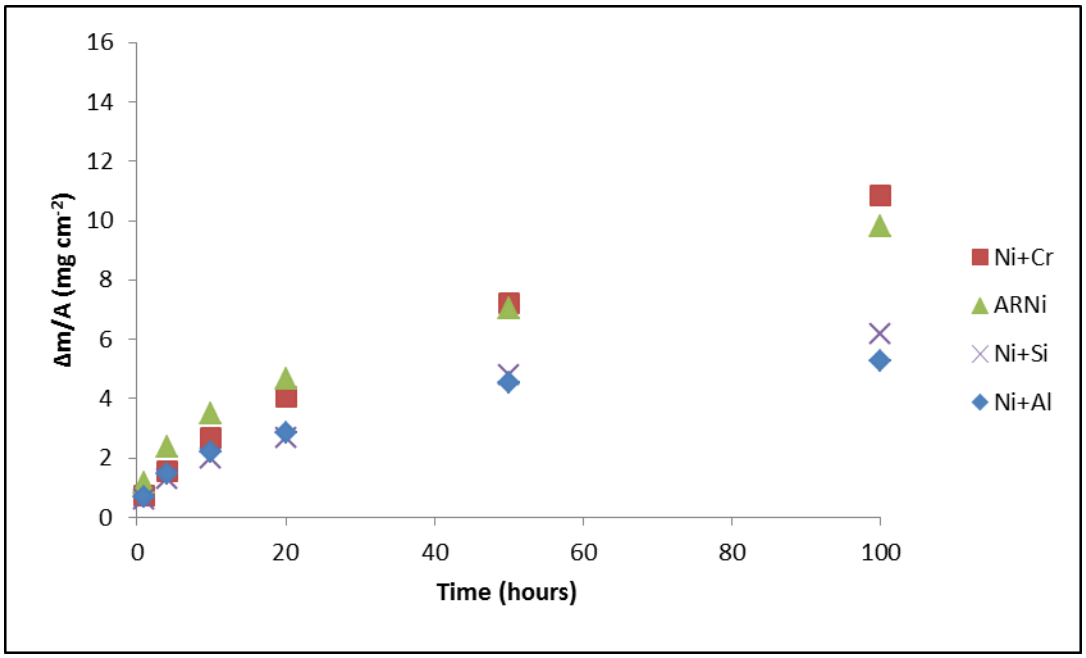

Figure 30: Mass gain per area for samples oxidized in stagnant lab air at 900°C

The data presented in Figure 30 shows accelerated mass gain occurred for sample oxidized at 900°C in comparison to those oxidized at 700°C. Additionally the data shows agreement with the relative oxidation rates predicted by Figures 9 and 10[4].

Mass gain data for the samples oxidized at 900°C with a deposit of Na_2SO_4 is presented in Figure 31.

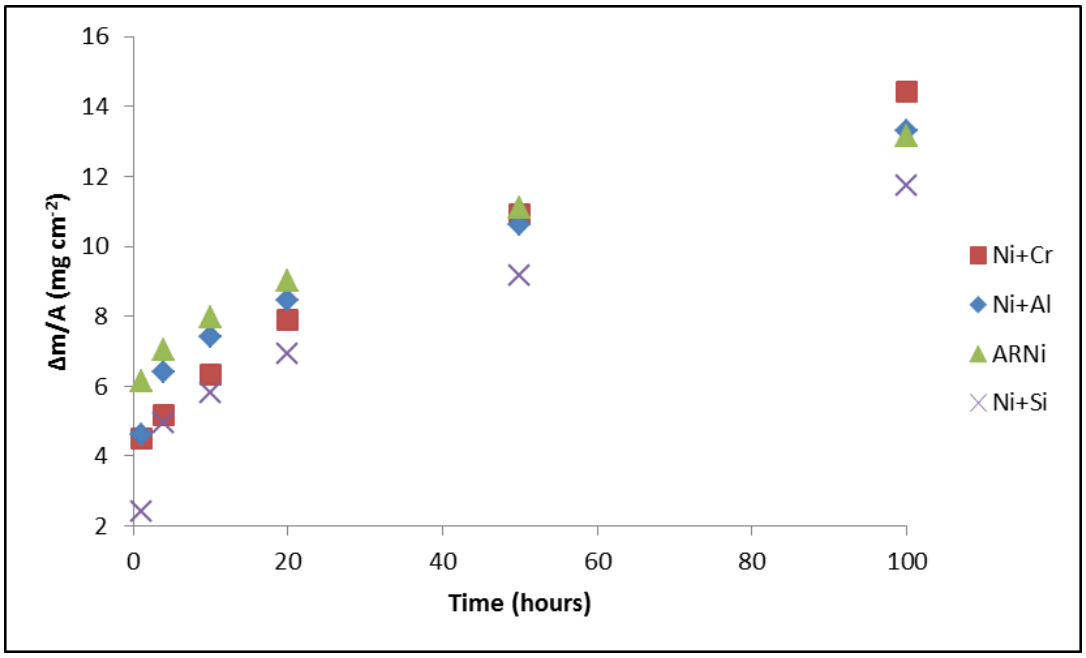

Figure 31: Mass gain per area for samples oxidized in stagnant lab air at 900°C with a Na_2SO_4 deposit

The mass gain data in Figure 31 show significantly increased rates of oxidation for samples with Na_2SO_4 deposits when compared to samples without. At 900°C, the temperature at which these samples are oxidized is above the 884°C melting point of pure Na_2SO_4. Though addition of contaminants can significantly alter the melting point of a deposit, it is unlikely that under the given experimental conditions the melting point would be significantly raised[2]. The presence of molten Na_2SO_4 on the sample surface allows for the development of a gradient to develop satisfying the Rapp-Goto criterion[2]. Additionally, reaction of the dissolved metal ions at the melt-gas interface could maintain the gradient[2]. It is likely that such a process would result in basic rather than acidic fluxing of metal ions due to the lack of $SO_{3\,(g)}$[2,46,47]. The slight leveling off of data at the 100 hour interval indicates that after this amount of time the melt has potentially been

isolated from the atmosphere, resulting in the collapse of the Rapp-Goto gradient and the cessation of hot corrosion.

In general, mass gain data suggests that applied coatings significantly altered the rates of mass gain for the Ni-201 samples. The relative rates of oxidation when no Na_2SO_4 deposit is present correlate well with kinetic predictions [4]. In the case of samples deposited with Na_2SO_4 both the rates of mass gain and the differences between the elemental coatings diminishes.

3.2 Calculated Rate Constants:

Rate constants were then calculated based upon data from gravimetric analysis. The calculated rate constants provide some quantitative insight into the differences in oxide growth rate between substrate coatings and exposure conditions. The majority of oxidized samples followed the parabolic rate law as described by Wagner's Theory. However, the oxidation rates of some samples were more accurately modeled by logarithmic rate law. Rate constants of those samples well described by parabolic kinetics are presented for comparison in Table 6.

Table 6: Experimentally Calculated Parabolic Rate Constants

Samples Obeying Parabolic Rate					
700°C Stagnant	k' [$mg^2 cm^{-4} hr^{-1}$]	**700°C + SO_2**	k' [$mg^2 cm^{-4} hr^{-1}$]	**900°C**	k' [$mg^2 cm^{-4} hr^{-1}$]
ARNi	7.70E-03	**ARNi**	3.14E-02	**ARNi**	9.74E-01
ARNi + Na_2SO_4	6.40E-03				
Ni + Al	7.00E-04	**Ni + Al**	9.78E-01	**Ni + Al**	3.08E-01
Ni + Al + Na_2SO_4	1.30E-03				
		Ni + Cr	9.86E-01	**Ni + Cr**	1.14
Ni + Cr + Na_2SO_4	1.90E-03			**Ni + Cr + Na_2SO_4**	9.40E-01
Ni + Si	1.50E-03	**Ni + Si**	9.77E-01	**Ni + Si**	3.97E-01
Ni + Si + Na_2SO_4	1.00E-03				

Effective modeling of the observed oxidation behavior by parabolic rate law suggests that under the described conditions the samples are well described by Wagner's Theory.

The experimentally determined constants for the samples that were more accurately described by logarithmic rate law are presented in Table 7.

Table 7: Experimentally Calculated Logarithmic Rate Constants

Samples Obeying Logarithmic Rate					
700°C Stagnant	k'_{log} [mg/(cm^2 log(hr))]	**700°C + SO_2**	k'_{log} [mg/(cm^2 log(hr))]	**900°C**	k'_{log} [mg/(cm^2 log(hr))]
		ARNi + Na_2SO_4	1.68E-01	**ARNi + Na_2SO_4**	1.78
				Ni + Al	1.02
		Ni + Al + Na_2SO_4	1.20E-01	**Ni + Al + Na_2SO_4**	1.50
Ni + Cr	8.24E-02				
		Ni + Cr + Na_2SO_4	1.51E-01		
		Ni + Si + Na_2SO_4	8.50E-02	**Ni + Si + Na_2SO_4**	1.91

The calculated rate constants reveal that, with the exception of the 700°C stagnant exposures and Ni + Cr at 900°C, oxidation in the presence of a deposit of Na_2SO_4 leads to logarithmic behavior. Finally, the growth of oxide on Ni + Al at 900°C without a deposit of Na_2SO_4 is described well with both parabolic and logarithmic equations.

The differences in kinetic behavior may be attributed to the greatly increased initial rates of corrosion within molten deposits, either above the melting point of Na_2SO_4 or via ternary melts, on the sample surface. The subsequently lower rates may be due to either saturation of the melt with dissolved oxide species or formation of a protective scale as oxidation progresses. Alternatively, the observe behavior could simply

be due to rapid ionic diffusion at, and subsequent removal of, grain boundaries, pores, and dislocations[6]. Due to the poorly understood nature logarithmic behavior, this area remains an intriguing avenue for further research.

3.3 Surface Morphology/EDS:

Comparisons of coupon surfaces and EDS spectra following oxidation at 700°C and 900°C for 1 and 100 hours are presented in the following section. Firstly, figures presenting data for samples oxidized at 700°C with and without Na_2SO_4 are presented to establish oxidation behaviors within the experimental environments in the absence of hot corrosion. Secondly, figures in which samples were deposited with Na_2SO_4 will be presented in order to clearly demonstrate that hot corrosion phenomena are observed when the approprate experimental conditions are developed. Finally, results for samples oxidized at 900°C both with and without Na_2SO_4 deposits will be presented. The results are discussed in the context of observing oxide formation, recrystalization of oxide into larger grain sizes, and the appearances of stress releif mechanisms such as fractures over the course of sample oxidation.

Figures 32 and 33 present the surface morphology and EDS chemical analysis of each of the coatings in stagnant lab air and flowing air/2ppm $SO_{2\,(g)}$ at 700°C for 1 hour. These images and EDS spectra are used to determine scale formation and adhearance under given experimental conditions. EDS data also provides some qualitative information about the presence of elements that can be used to infer the development of compounds such as oxides and sulfur containing species.

Surface morphology and EDS results for the ARNi and Ni + Al samples oxidized at 700°C in stagnant lab air and air/$SO_{2\ (g)}$ are presented in Figure 32.

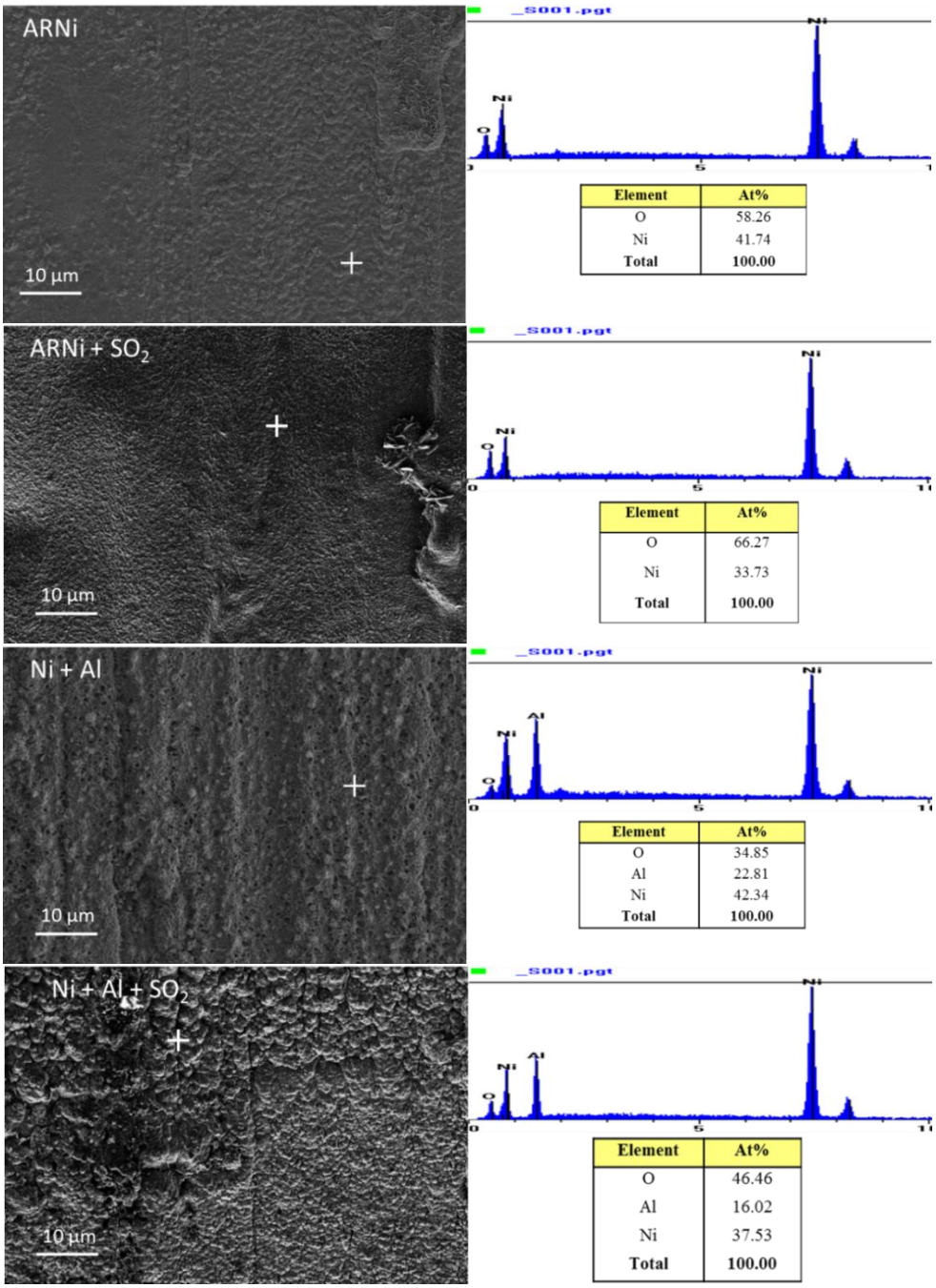

Figure 32: Surface morphology and EDS data for ARNi and Ni + Al samples oxidized for 1 hour at 700°C in stagnant lab air and air/$SO_{2\ (g)}$

The EDS data presented in Figure 32 illustrates that it is likely that the progression of uncoated nickel into nickel oxide (NiO) on the uncoated samples has occurred. Significantly different grain structure is also observed between samples exposed to $SO_{2\,(g)}$ and those oxidized in stagnant lab air.

Surface morphology and EDS results for the Ni + Cr and Ni + Si samples oxidized at 700°C in stagnant lab air and air/$SO_{2\,(g)}$ are presented in Figure 33.

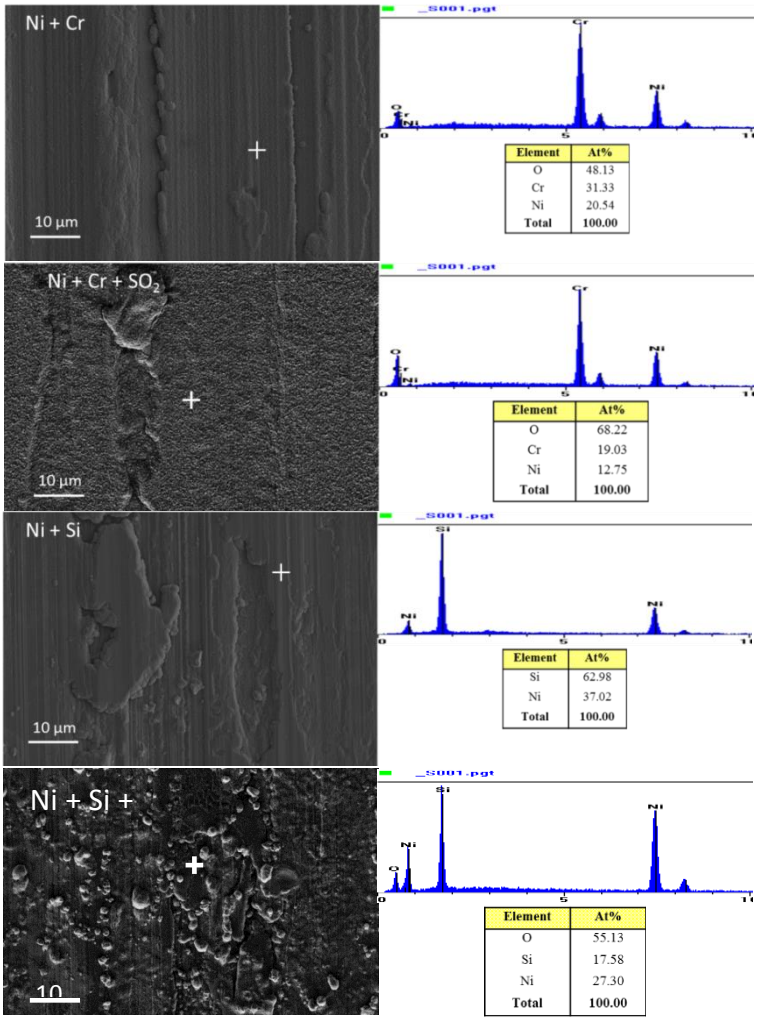

Figure 33: Surface morphology and EDS data for Ni + Cr and Ni + Si samples oxidized for 1 hour at 700°C in stagnant lab air and air/$SO_{2\,(g)}$

The EDS data in Figures 32 and 33 also suggests the progression of each of the elemental coatings into their well-known oxide species, namely chromium into Cr_2O_3, aluminum into Al_2O_3, and silicon into SiO_2[6]. At this point in oxidation, the scales appear well adhered to the substrate surfaces with no appearance of stress relief mechanisms. The spectrum of Cr, Figure 33 is devoid of Ni in comparison to the other coating elements exposed to the same conditions. This finding agrees with previous studies of Ni-Al-Cr systems in which inter-diffusion of Ni and Al along concentration gradients occurs more quickly than inter-diffusion of Ni and Cr[70]. The differences in morphology between the samples oxidized in lab air and those in flowing air/$SO_{2\,(g)}$ could be due to competition between oxidation and the formation of sulfide and sulfate species similar to that described by the phase diagram for Al, presented in Figure 15. However, the lack of a signal for sulfur in EDS spectra suggests that this difference in morphology could simply be an effect of flowing rather than stagnant atmosphere.

Figures 34 and 35 present the surface morphology and EDS data for those samples oxidized for 100 hours at 700°C. Figure 34 presents the data for ARNi and Ni + Al samples. The results are used to determine scale resilance under these conditions, as well as changes to grain structure over the course of oxidation.

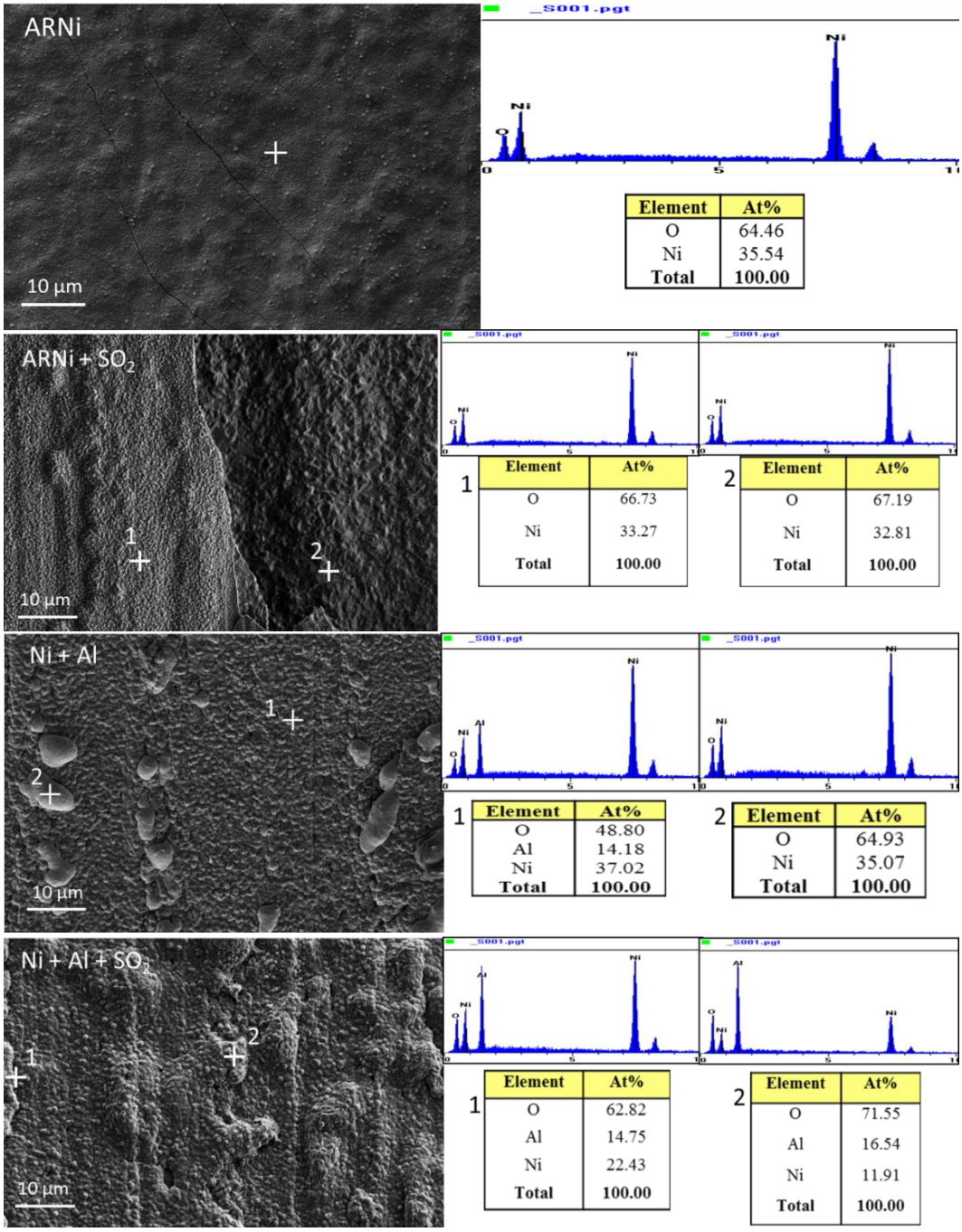

Figure 34**:** Surface morphology and EDS data for ARNi and Ni + Al samples oxidized for 100 hours at 700°C in stagnant lab air and flowing air/$SO_{2\,(g)}$.

Figure 35 presents the data for Ni + Cr and Ni + Si samples. Results are used to evaluate scale resilance and changes to grain structure over the course of oxidation.

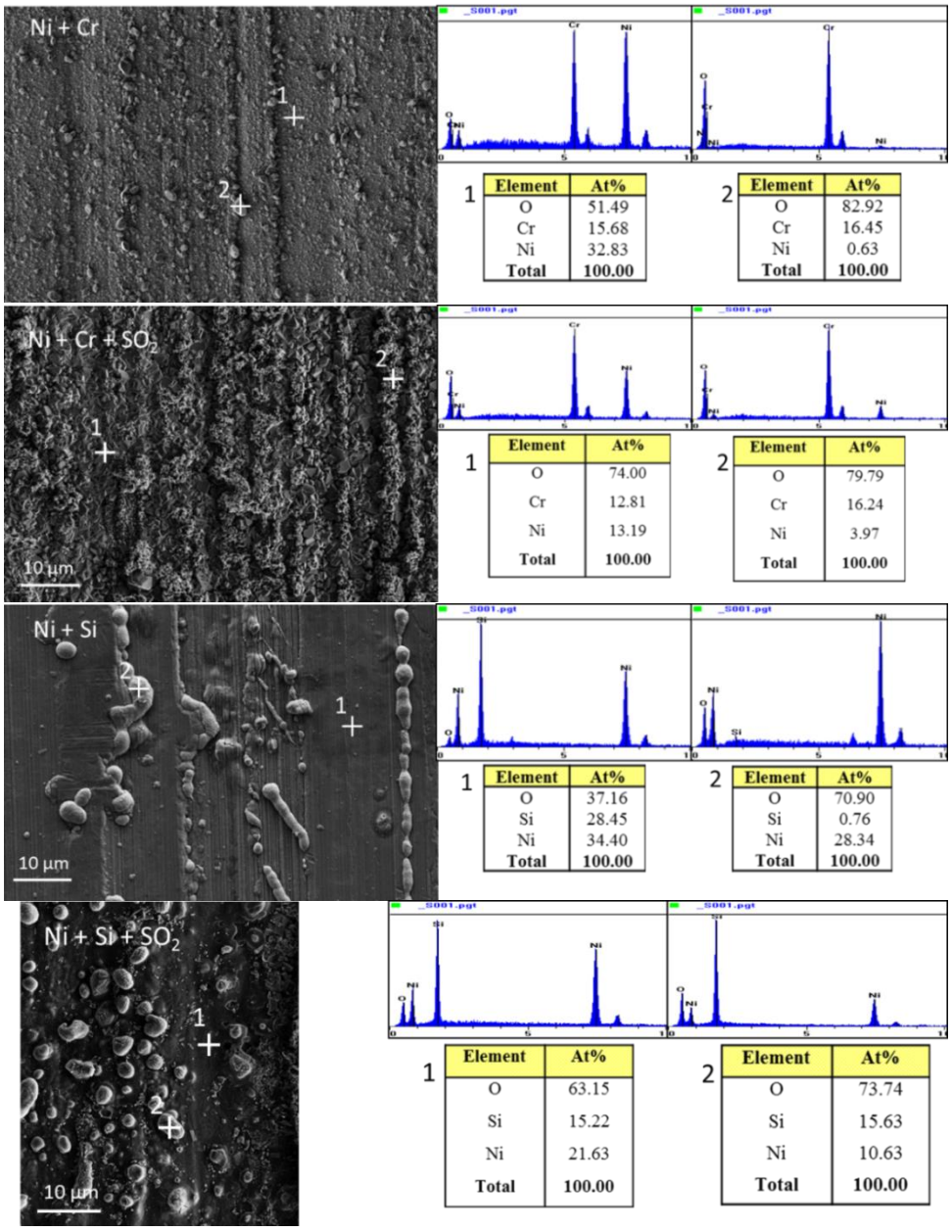

Figure 35: Surface morphology and EDS data for Ni + Cr and Ni + Si samples oxidized for 100 hours at 700°C in stagnant lab air and flowing air/$SO_{2\,(g)}$.

Following oxidation for 100 hours at 700°C samples appear to have formed larger grain structures than the samples oxidized for only 1 hour. The formation of larger grain structures is associated with the transition from oxidation reactions dominated by rapid diffusion of gasses at grain boundaries to the slower lattice diffusion oxidation as

outlined in Wagner's theory[2,6]. The appearance of some signs of stress releif, namely cracks, on the bare Ni-201 and Cr coated Ni indicates that either compressive stresses or stresses due differnces in thermal coefficients of expansion such as those discussed previously are developed over the course of oxidation[2]. Surface morphology comparisons also show that smaller grain sizes appear to form on samples exposed to $SO_{2\,(g)}$. This could indicate that formation of sulfide and sulfate species is again competeing with oxidation when $SO_{2\,(g)}$ is introduced. Alternatively, it could also be due to the differences between a stagnant and a flowing atmosphere. The only exception to these morphological changes is in Ni + Si samples, which appear to have similar grain structure following oxidation in both environments.

Figures 36-39 present the surface morphology and EDS data for samples oxidized at 700°C in stagnant lab air and flowing air/$SO_{2\,(g)}$ with deposits of Na_2SO_4 for 1 hour. These are examined using the same techniques outlined previously. Images and EDS spectra describe the effects of exposure under given conditions in regards to the formation of ternary melts and other hot corrosion phenomena. First the data for ARNi samples oxidized at 700°C in stagnant lab air and flowing air/$SO_{2\,(g)}$ mixture for 1 hour are presented in Figure 36.

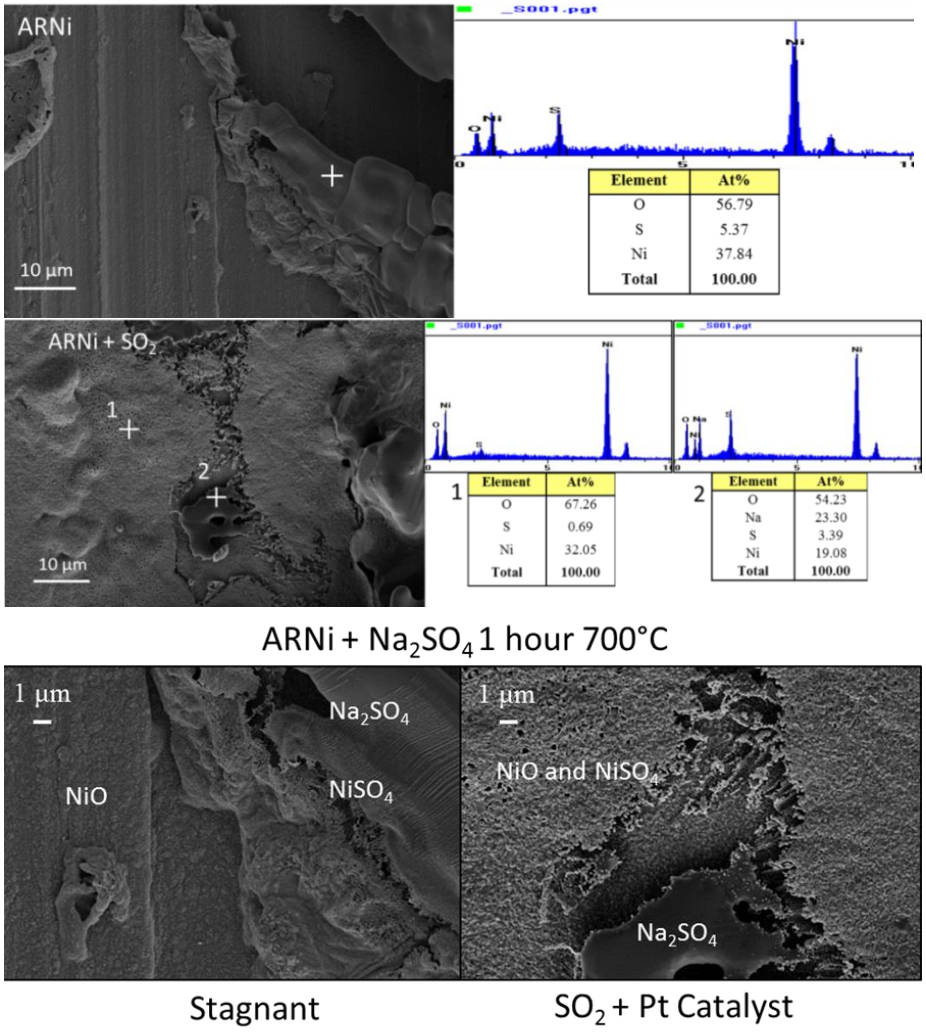

Figure 36: As received Ni-201 oxidized with a deposit of Na_2SO_4 for 1 hour at 700°C in stagnant lab air and flowing air/$SO_{2\ (g)}$.

Figure 36 shows that following oxidation in the presence of Na_2SO_4 deposits for one hour some surface interaction between the deposit and the Ni-201 appears to have occurred in both environments. The effects appear to be much more widespread in the environment with flowing $SO_{2\ (g)}$, which is likely due to more sulfur being available for reaction to form metal sulfates. Figure 36 also demonstrates that grain size differences noted between the two atmosphers appears when the deposit is introduced.

Figure 37 presents surface images and EDS data for Ni + Al samples oxidized at 700°C in stagnant lab air and flowing air/$SO_{2\ (g)}$ mixture for 1 hour.

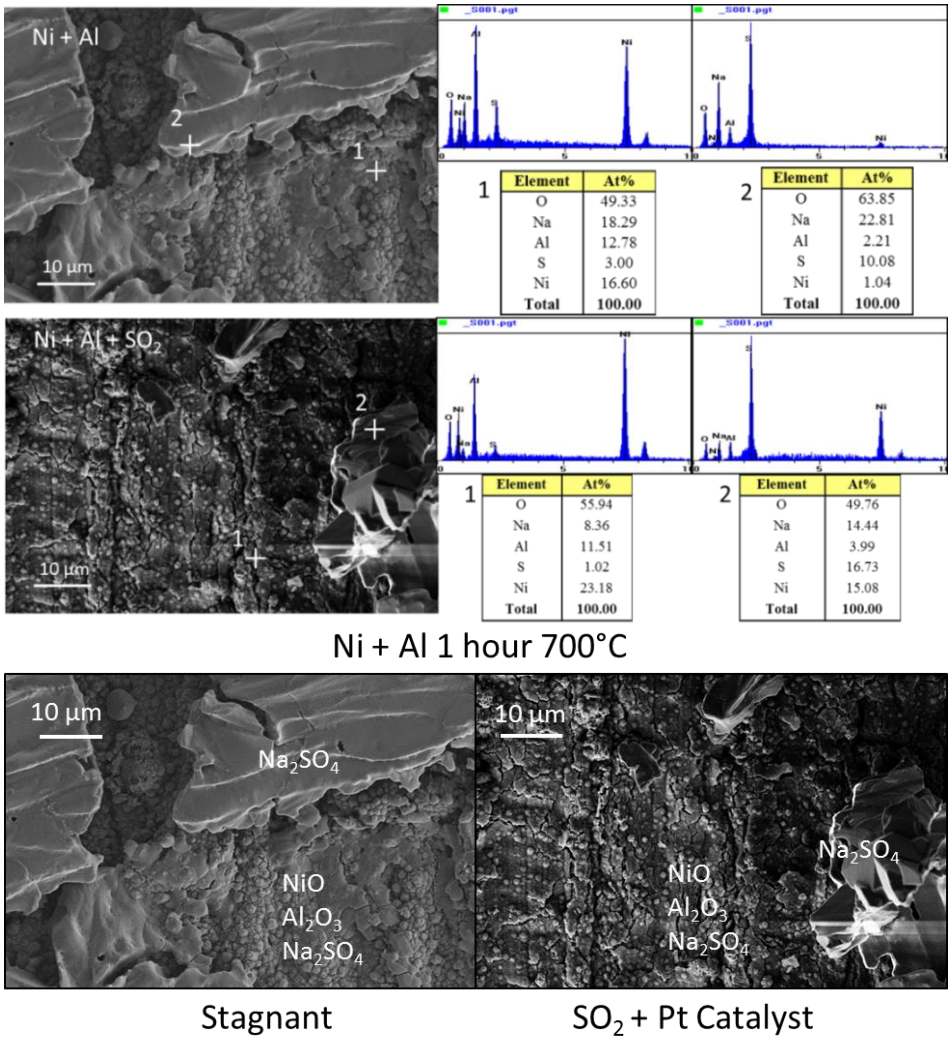

Figure 37: Ni-201 coated in Al and oxidized with a deposit of Na_2SO_4 for 1 hour at 700°C in stagnant lab air and flowing air/$SO_{2\ (g)}$.

Less morphological differences appear between the Al coated Ni-201 samples oxidized in $SO_{2\ (g)}$ and in stagnant lab air. Additionally, EDS spectra indicate widespread presence of Na_2SO_4 elements across the sample surface for samples oxidized in both atmospheres.

Thin deposits of Na_2SO_4 potentially provide small barriers to reactive gasses that could become molten providing the components necessary for hot corrosion initiation.

Figure 38 presents surface images and EDS data for Ni + Cr samples xidized at 700°C in stagnant lab air and flowing air/$SO_{2\ (g)}$ mixture for 1 hour.

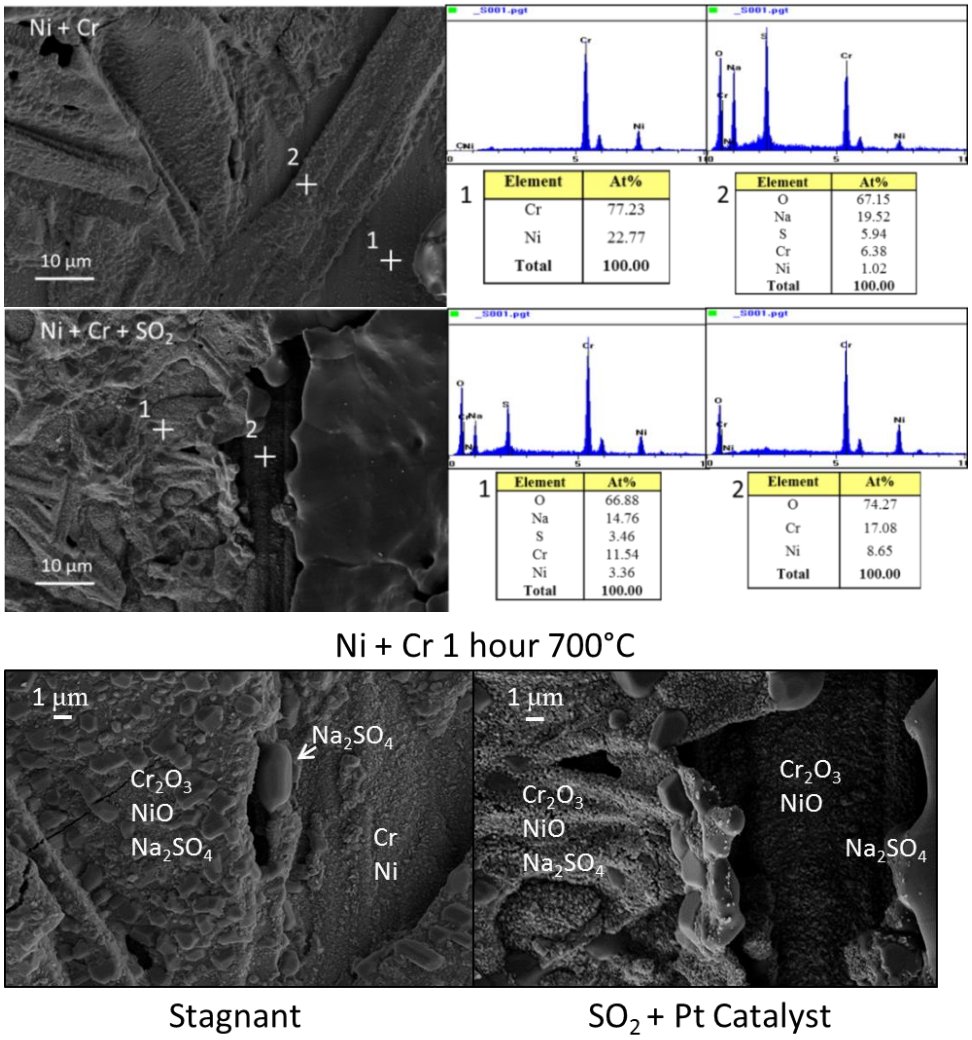

Figure 38: Ni-201 coated in Cr and oxidized with a deposit of Na_2SO_4 for 1 hour at 700°C

Samples of Ni + Cr show EDS and morphological evidence for ternary melt development in both regimes when oxidized in the presence of a Na_2SO_4 deposit, Figure 38. Similar to

the samples coated in Al, the effects appear more widespread and to exhibit smaller grain size for the samples oxidized in the presence of $SO_{2\,(g)}$. While not definitive, this suggests different chemistry, namely sulfide and sulfate formation, may be occurring with the addition of the flowing atmosphere.

Figure 39 presents surface images and EDS data for Ni + Si samples oxidized at 700°C in stagnant lab air and flowing air/$SO_{2\,(g)}$ mixture for 1 hour.

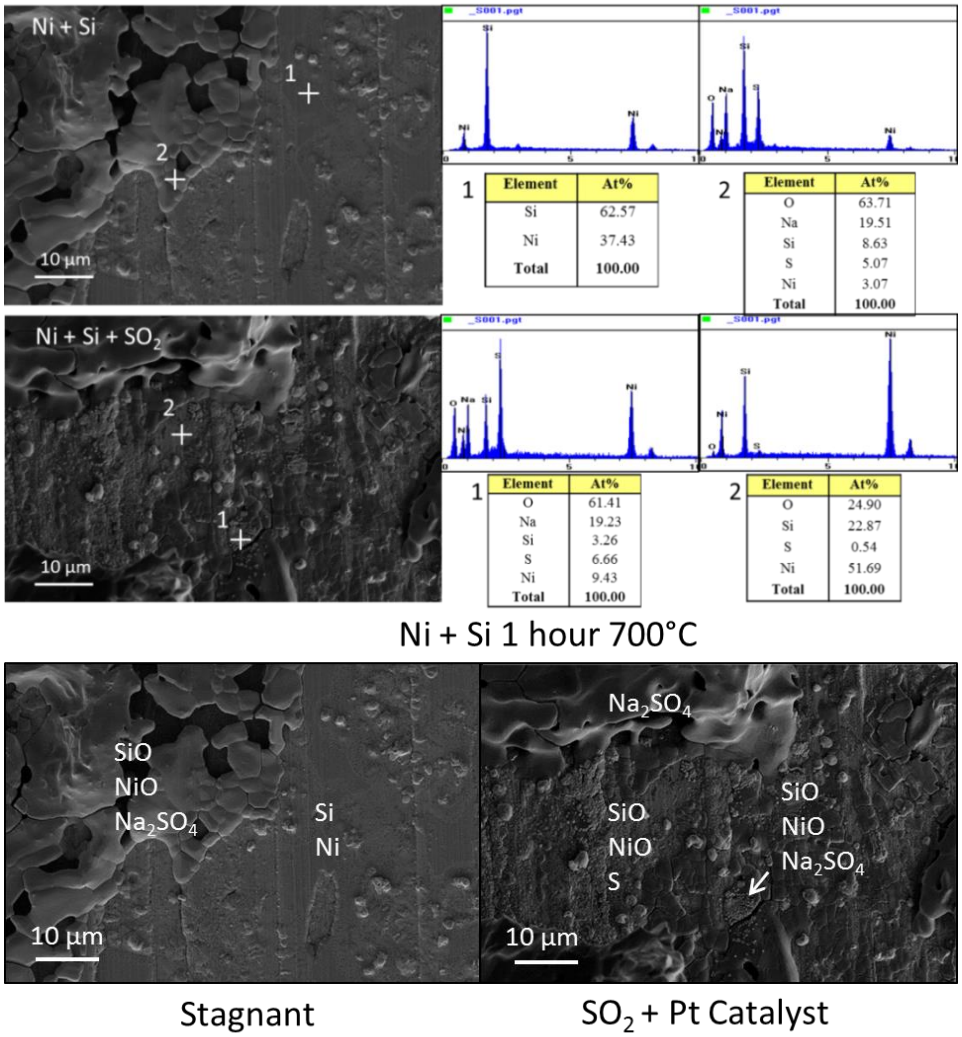

Figure 39: Ni-201 coated in Si and oxidized with a deposit of Na_2SO_4 for 1 hour at 700°C

Figure 39 shows limited differences occur between samples oxidized in the presence of a Na_2SO_4 deposit for Ni-201 coated in Si. Due to the lack of a ternary melt for the Ni-S-Si system the findings are consistent with previous studies that indicated SiO_2 dissolution is a physical rather than chemical process[57]. Some evidence for stress relief mechanisms does appear in samples oxidized in $SO_{2\ (g)}$, this result could indicate that grain boundary diffusion is occurring similarly to that described for NiO[2].

Figures 36-39 presents evidence of larger amounts of surface deformation on samples with salt deposits. The formation of large cracks, likely due to the development of stress on the oxide layer, for samples with Na_2SO_4 deposits further indicates that spallation of surface material may have occurred selectively in the presence of salt deposits. This phenomenon may be occuring in this instance as Ni-201 contains some sulfur impurity as denoted in Table 3[65]. Linescan analysis could provide information regarding any build-up sulfur beneath the developed coatings.

Next samples exposed to the same conditions for 100 hours are presented in Figures 40-43. These images provide insight in regards to scale formation and stabillity for each coating as well as observing the progress of hot corrosion phenomena for this set of conditions. Figure 40 presents the surface image and EDS data for ARNi samples oxidized at 700°C in stagnant lab air and flowing air/$SO_{2\ (g)}$ mixture for 100 hours.

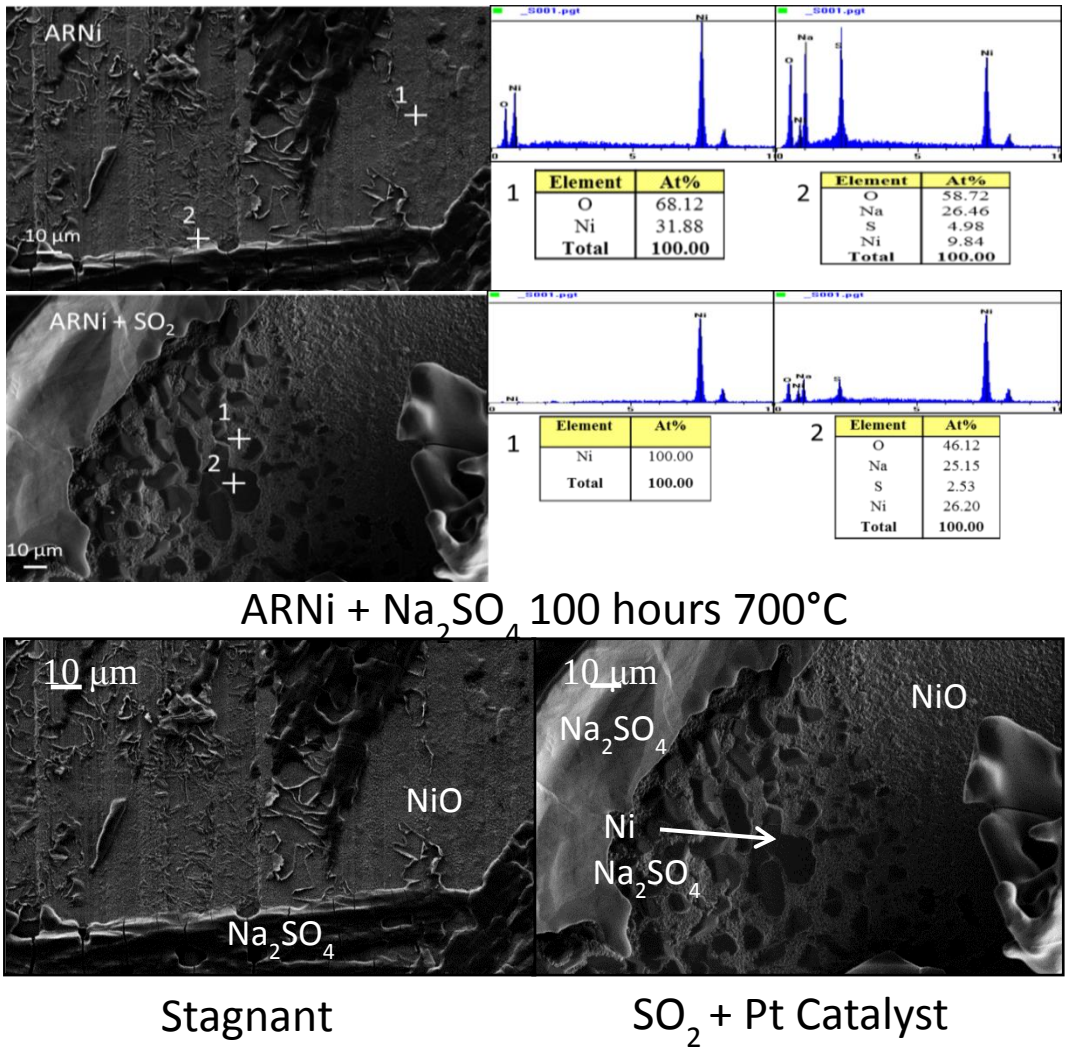

Figure 40: Ni-201 oxidized with a deposit of Na_2SO_4 for 100 hours at 700°C

Figure 40 morphology and EDS spectra support the possible formation of the reported $NiSO_4$-Na_2SO_4 ternary melt for the sample exposed to $SO_{2\,(g)}$[62]. This finding further supports the occurance of hot corrosion suggested by the increase mass gain observed in the data presented in Figure 29.

Figure 41 presents the surface image and EDS data for Ni + Al samples oxidized at 700°C in stagnant lab air and flowing air/$SO_{2\,(g)}$ mixture for 100 hours.

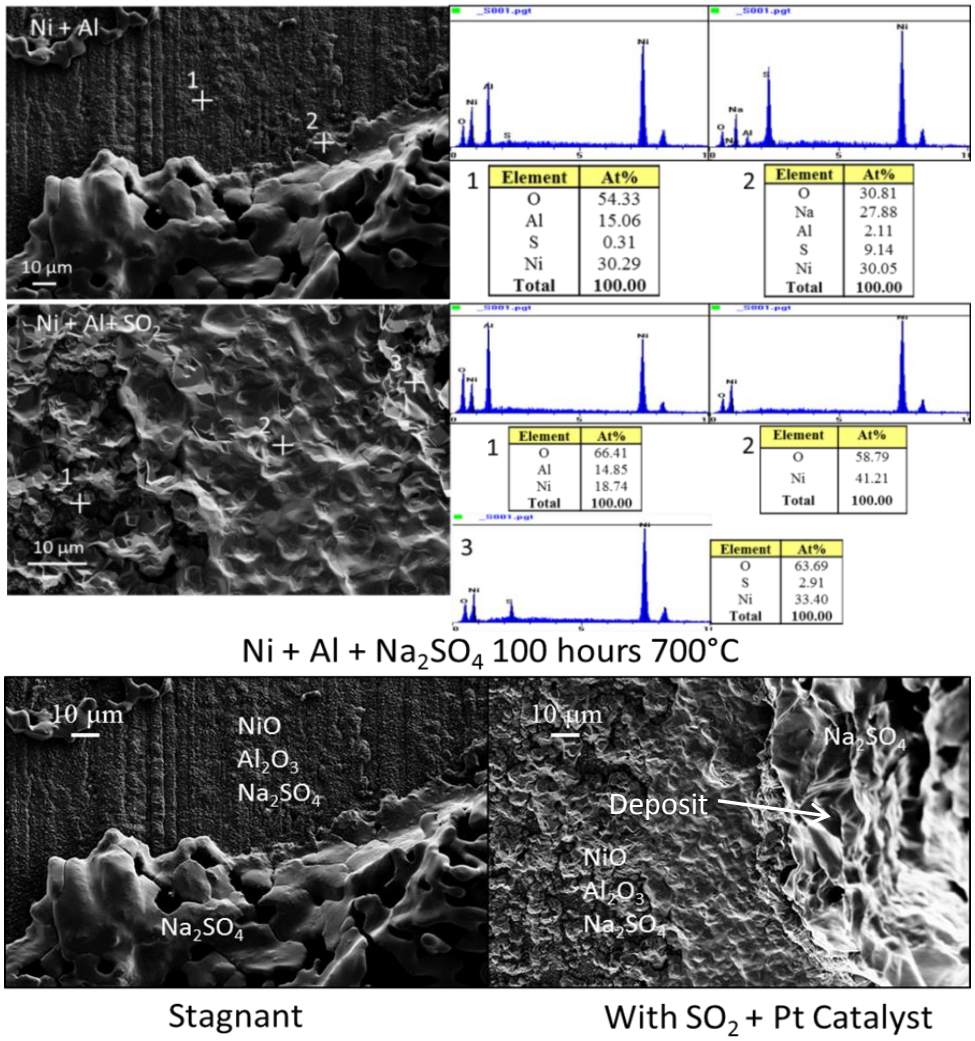

Figure 41: Ni-201 coated in Al and oxidized with a deposit of Na_2SO_4 for 100 hours at 700°C

Figure 41 shows that the samples coated in Al also exhibit morphology and EDS signals that suggest ternary melt formation in samples exposed to $SO_{2\ (g)}$. Specifically the presence of Ni and oxygen signals within the melt like deposit suggests that flux of Ni ions into the salt layer. Finally, the EDS signal for sulfur, Ni, and oxygen near the top of the deposit could indicate that Ni ions dissolved within the melt are reacting with $SO_{3\ (g)}$ and $O_{2\ (g)}$ at the melt-gas interface to form nickel sulfide (NiS_2) and NiO.

Figure 42 presents the surface image and EDS data for Ni + Cr samples oxidized at 700°C in stagnant lab air and flowing air/$SO_{2\ (g)}$ mixture for 100 hours.

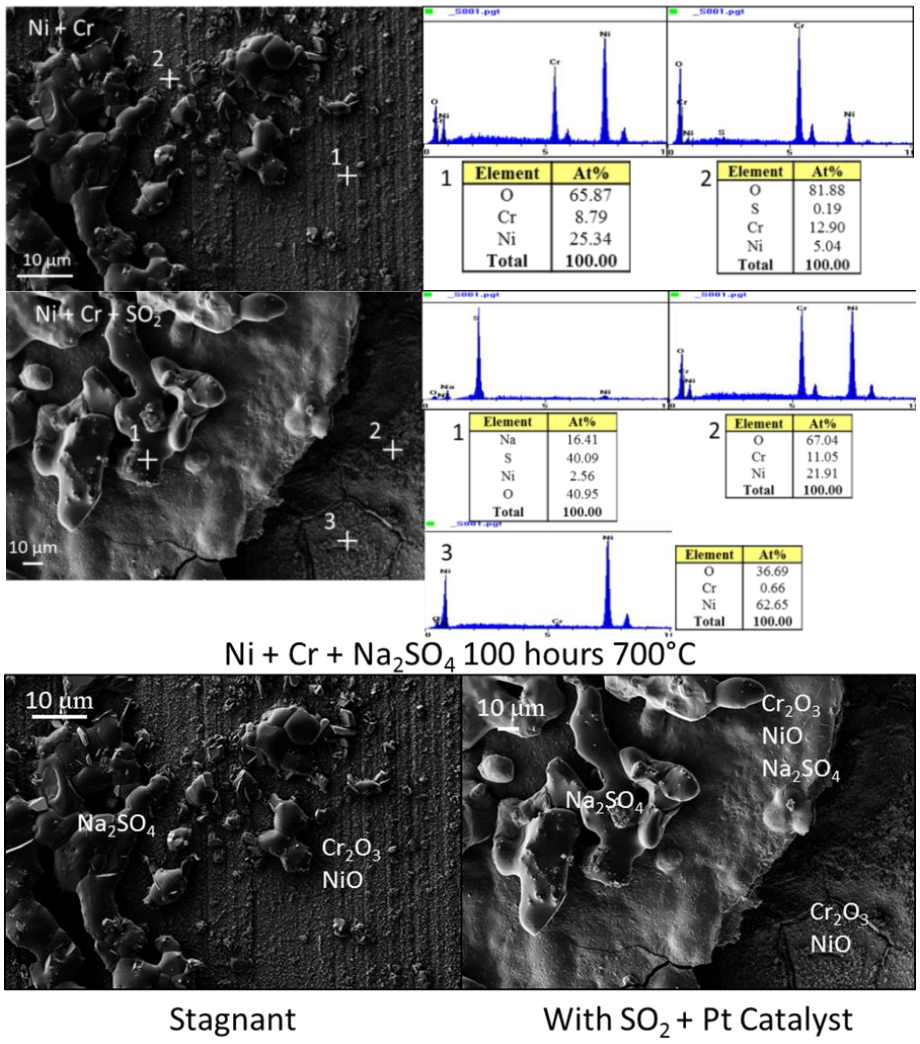

Figure 42: Ni-201 coated in Cr and oxidized with a deposit of Na_2SO_4 for 100 hours at 700°C

Figure 42 illustrates the both the increased evidence for formation of ternary melts and the appearance of stress relief mechanisms for Cr coated Ni-201 that occur with the addition of $SO_{2\ (g)}$, a result consistent with the more pronounced development of stresses for Cr_2O_3 scales[6].

Figure 43 presents the surface image and EDS data for Ni + Si samples oxidized at 700°C in stagnant lab air and flowing air/$SO_{2\ (g)}$ mixture for 100 hours.

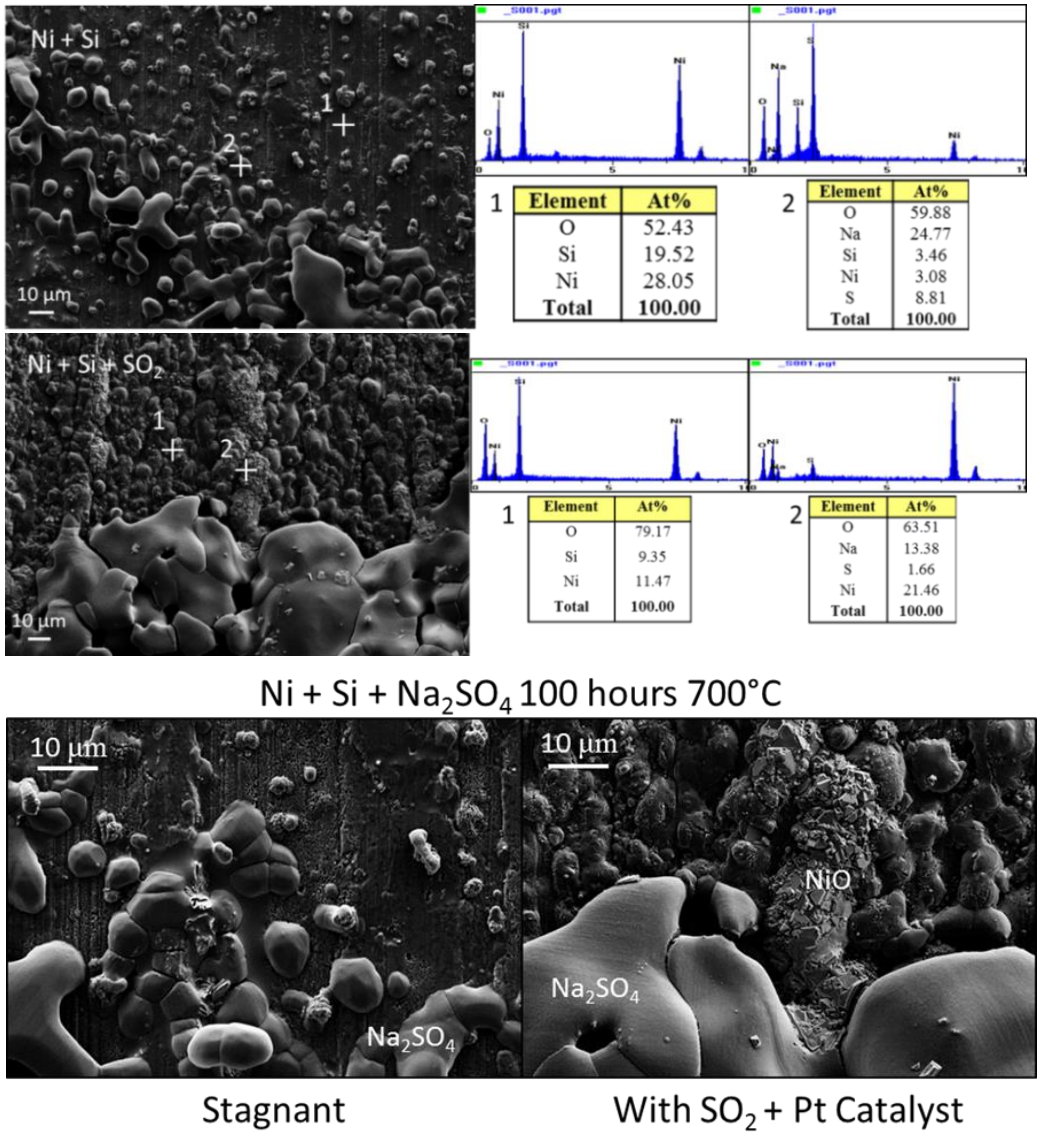

Figure 43: Ni-201 coated in Si and oxidized with a deposit of Na_2SO_4 for 100 hours at 700°C

Figure 43 shows the development of a NiO scale along a surface finishing mark for the Ni + Si sample exposed to $SO_{2\ (g)}$. The formation of this NiO scale is likely due to the

diffusion of reactants within the surface finishing mark, suggesting that preparing substrates with minimal finishing marks could potentially inhibit this type of oxide formation. It is possible that the deformation of grain boundaries at these marks could further increase grain boundary diffusion. As discussed previously, this mechanisms dominates for Ni when temperatures are below about 900°C[2]**.** The more rapidly growing NiO scale present at the finishing marks can place a lateral stress on the slower growing SiO_2[2]. If this stress becomes large enough it can lead to scale delamination and subsequent removal of the Si coating.

Figures 44-47 present the results of oxidation of samples with and without Na_2SO_4 deposits at 900°C for 1 hour. These samples are used to make comparisons between oxide growth and stability at 700°C and 900°C. Figure 44 presents the surface image and EDS data for ARNi samples oxidized at 900°C in stagnant lab for 1 hour with and without Na_2SO_4 deposits.

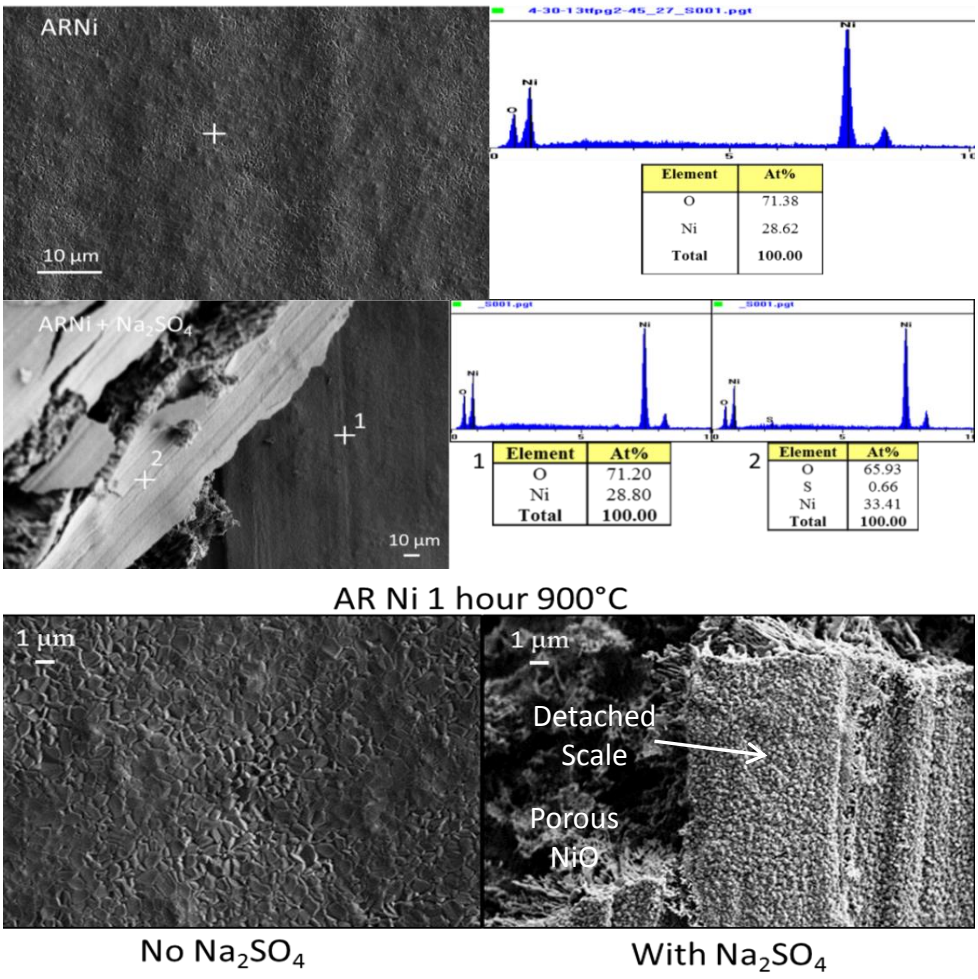

Figure 44: Ni-201 oxidized for 1 hour at 900°C in stagnant lab air.

Figure 44 illustrates that significant differences occur between samples with and without Na_2SO_4 deposits during the oxidation process for Ni-201 at 900°C. Samples with Na_2SO_4 deposits illustrate dramatic scale detachment. The scale deposit could be a result of changing oxidation rates due to action of molten salt species on areas where grain boundaries exist. The salt deposit is more likely to come into contact with these regions when completely molten. As oxidation rates vary across the surface and are perhaps more pronounced at grain boundaries where molten salt is present, the build up of lateral stresses could be responsible for the more aggressive scale delamination. Additonally,

samples appear to contain large deposits of porus NiO deposits. These deposits are consistent with the non-protective metal oxide deposits described as a product of the fluxing process of hot corrosion[2,6,46,47].

Figure 45 presents the surface image and EDS data for Ni + Al samples oxidized at 900°C in stagnant lab for 1 hour with and without Na_2SO_4 deposits.

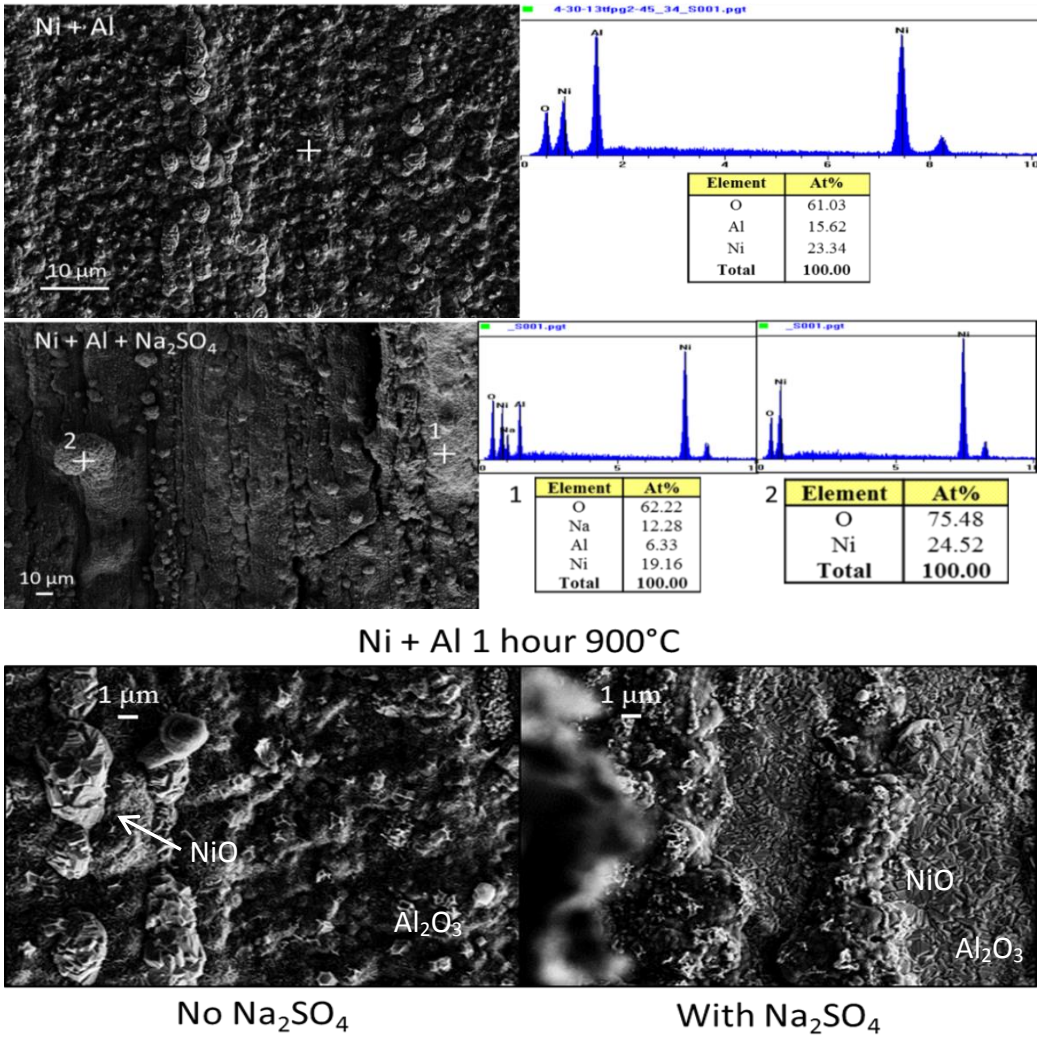

Figure 45: Ni-201 coated in Al and oxidized for 1 hour at 900°C in stagnant lab air.

Images and EDS spectra in Figure 45 of Ni-201 samples coated in Al appear to more clearly illustrate the formation of rapidly growing zones of NiO developing along surface finishing marks during oxidation at 900°C. The effects once again appear more pronounced when Na_2SO_4 deposits are introduced. Evidence of some scale delamination and stress releif mechanisms is also present when Na_2SO_4 deposits are present.

Figure 46 presents the surface image and EDS data for Ni + Cr samples oxidized at 900°C in stagnant lab for 1 hour with and without Na_2SO_4 deposits.

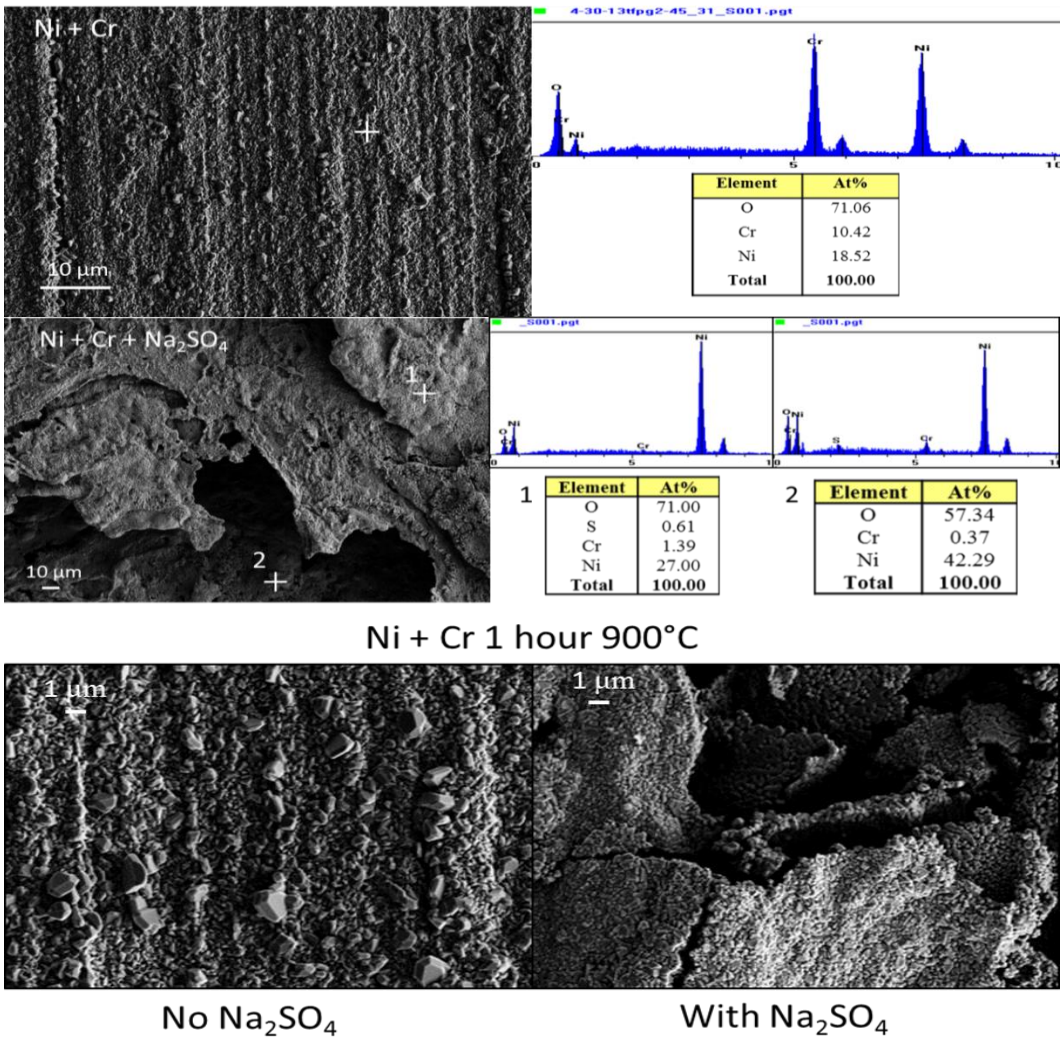

Figure 46: Ni-201 coated in Cr and oxidized for 1 hour at 900°C in stagnant lab air.

Figure 46 presents the EDS and for Ni-201 samples coated in Cr and oxidized at 900°C in stagnant lab air. The data indicates that in the presence of Na_2SO_4 deposits this regime causes scale delamination and the development of surface deformation for Cr coated samples in a similar fashion to the effects observed for Al coated and bare Ni-201.

Figure 47 presents the surface image and EDS data for Ni + Si samples oxidized at 900°C in stagnant lab for 1 hour with and without Na_2SO_4 deposits.

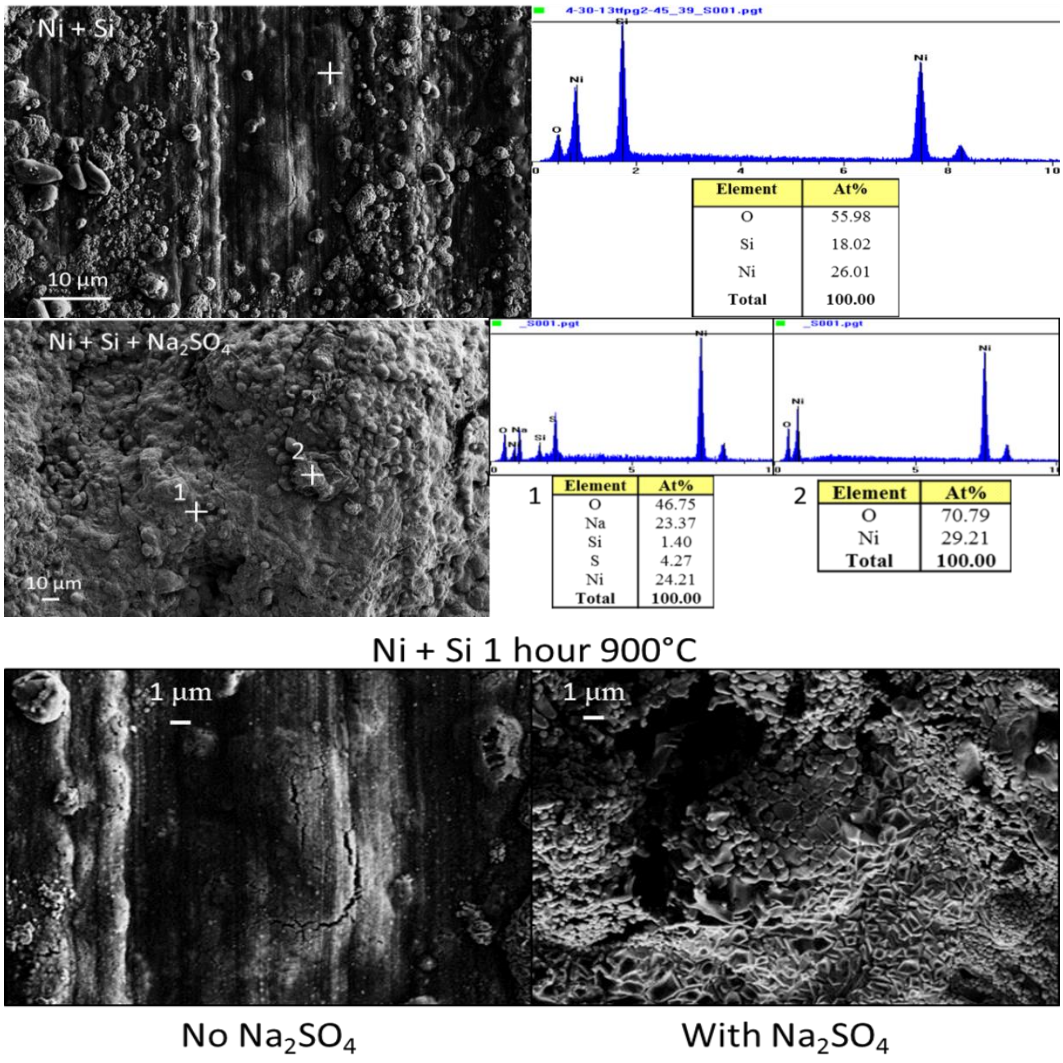

Figure 47: Ni-201 coated in Si and oxidized for 1 hour at 900°C in stagnant lab air.

The data presented in Figure 47 for oxidation of Si coated Ni-201 at 900°C for 1 hour also shows significant differences between samples with deposits of Na_2SO_4 and those without. In contrast the presence of the deposit does not appear to as significantly alter the occurance of surface deformations such as cracks or delaminated scales. However, there does appear to be large differences between the grain structure of the surface species between the different treatments.

Figures 48-51 present the results of oxidation of samples with and without Na_2SO_4 deposits at 900°C for 100 hours. The data is used for comparison of grain size and oxide scale stability over the course of oxidation. Figure 48 presents the surface image and EDS data for ARNi samples oxidized at 900°C in stagnant lab for 100 hours with and without Na_2SO_4 deposits.

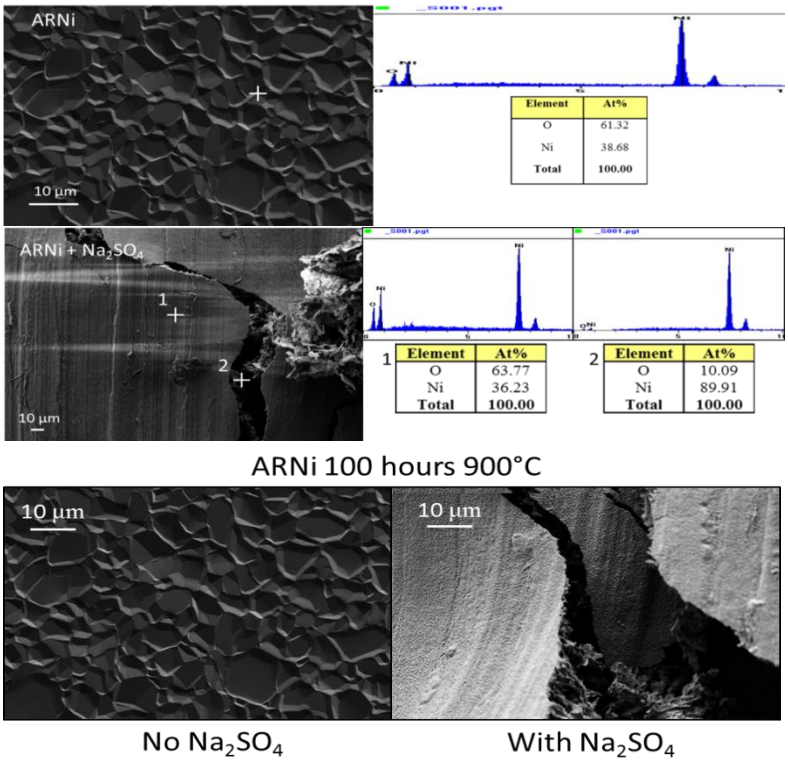

Figure 48: Ni-201 oxidized for 100 hours at 900°C in stagnant lab air.

Figure 48 shows the progression of Ni-201 samples during oxidation at 900°C with and without Na_2SO_4 deposits. Samples without deposits illustrate the growth of NiO into larger grain sizes as previously described[2]. Images and EDS of samples with deposits demonstrate the previously described aggressive scale delamination persits over the course of oxidation.

Figure 49 presents the surface image and EDS data for Ni + Al samples oxidized at 900°C in stagnant lab for 100 hours with and without Na_2SO_4 deposits.

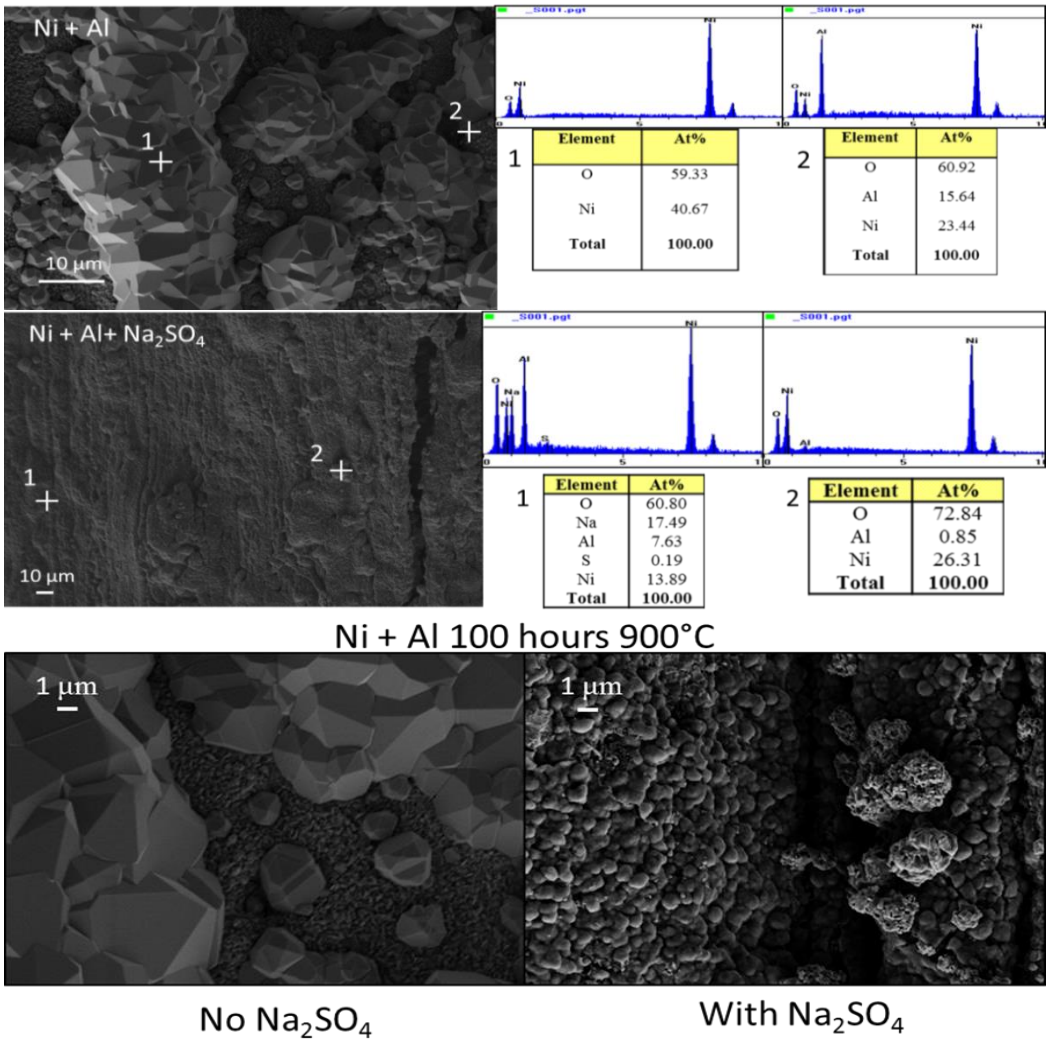

Figure 49: Ni-201 coated in Al and oxidized for 100 hours at 900°C in stagnant lab air.

The samples of Al coated Ni-201 oxidized for 100 hours at 900°C also demonstrate the effects of recrystalization of NiO. For samples without deposits the large NiO crystals appear to dominate regions that were previously grain boundaries. For samples with deposits more surface deformation and scale delamination is present.

Figure 50 presents the surface image and EDS data for Ni + Cr samples oxidized at 900°C in stagnant lab for 100 hours with and without Na_2SO_4 deposits.

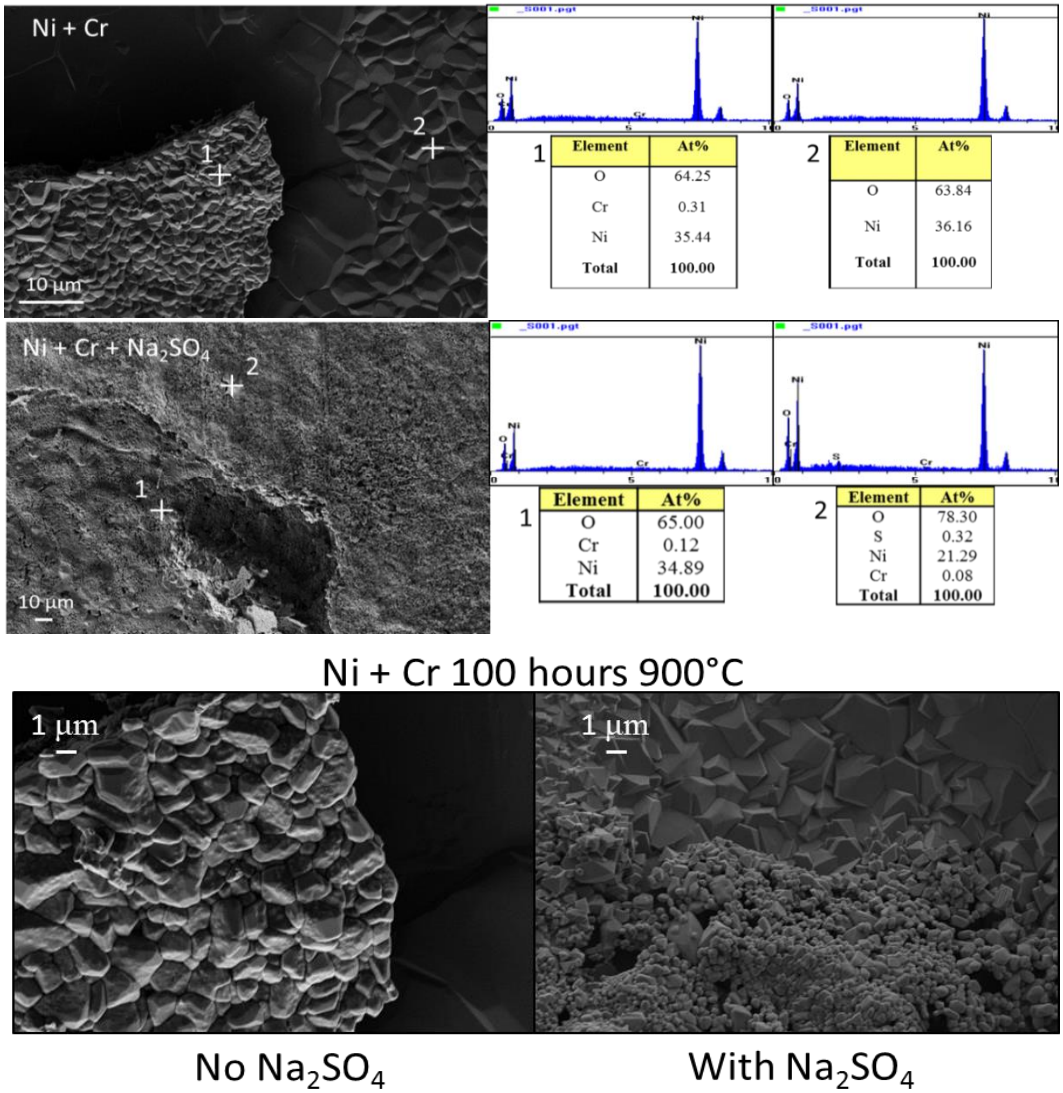

Figure 50: Ni-201 coated in Cr and oxidized for 100 hours at 900°C in stagnant lab air.

In Figure 50 scale delamination for Ni-201 samples coated in Cr appears to have occurred in both samples with and without Na_2SO_4 deposits. This finding is consistent with the noted difficulty in adherance of Cr_2O_3 scales, due to oxide formation at both the metal-scale and scale-gas interface[2].

Figure 51 presents the surface image and EDS data for Ni + Si samples oxidized at 900°C in stagnant lab for 100 hours with and without Na_2SO_4 deposits.

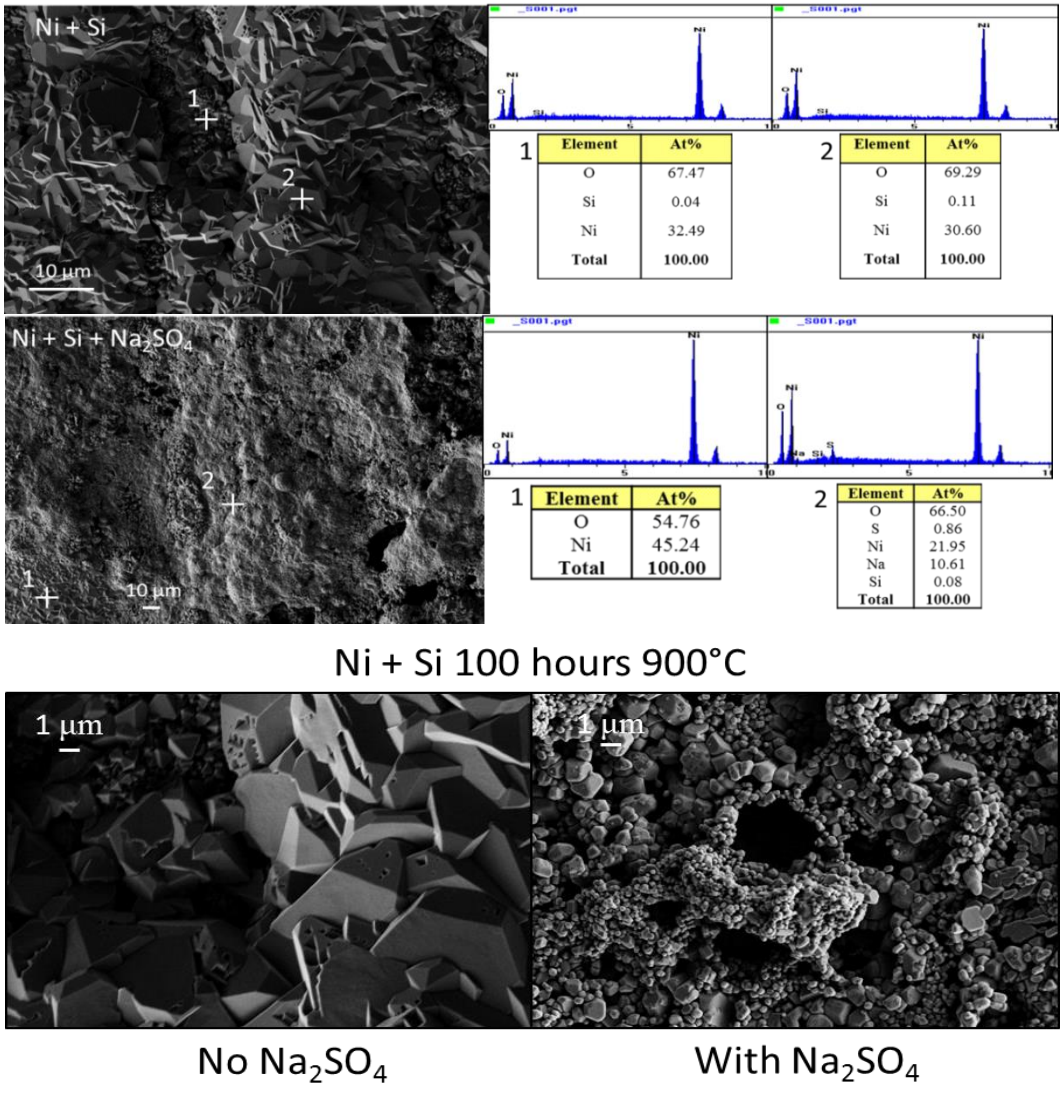

Figure 51: Ni-201 coated in Al and oxidized for 100 hours at 900°C in stagnant lab air.

In the case Ni + Si samples oxidized for 100 hours at 900°C, increased grain structure for NiO is once again observed in the absence of Na_2SO_4 deposits. Additionally, altered surface morphology for those samples with deposits could indicate activity of the molten salt on Ni at grain boundaries lead to stress that has resulted in stress releif mechanisms such as buckling of the surface coating.

The surface morphology and EDS data illustrated that significant differences occur for oxidation reactions with the introduction of Na_2SO_4 deposits and $SO_{2\,(g)}$. These results also found significant evidence for hot corrosion phenomena when the experimental conditions matched those described by literature. Further characterization of the sample was carried out in order to fully characterize the progression of oxidation and hot corrosion.

3.4 Cross Section Data:

Cross section images and linescane EDS analysis was carried out on selected samples to observe the interdiffusion of metal species and to confirm flux of metal species into Na_2SO_4 deposits on samples in which hot corrosion is suspected. Normally, in the temperature regimes tested with ambient laboratory air nickel oxide (NiO) would be expected to form a continuous protective layer[6]. As discussed previously, during the hot corrosion process this layer is dissolved and removed, either chemically or physically, when a molten salt is present. The applied coatings would ideally serve as ion barriers preventing or greatly slowing the diffusion of Ni ions to form NiO. Additionally, the oxidation products of the single element coating are expected to display reduced solubility in molten salt deposits when compared with NiO.

Figure 52 presents cross section data for the coated Ni-201 samples following deposition via sputtering PVD. These are presented to demonstrate the effectiveness of coating techniques in generating elemental coatings ~1 μm thick.

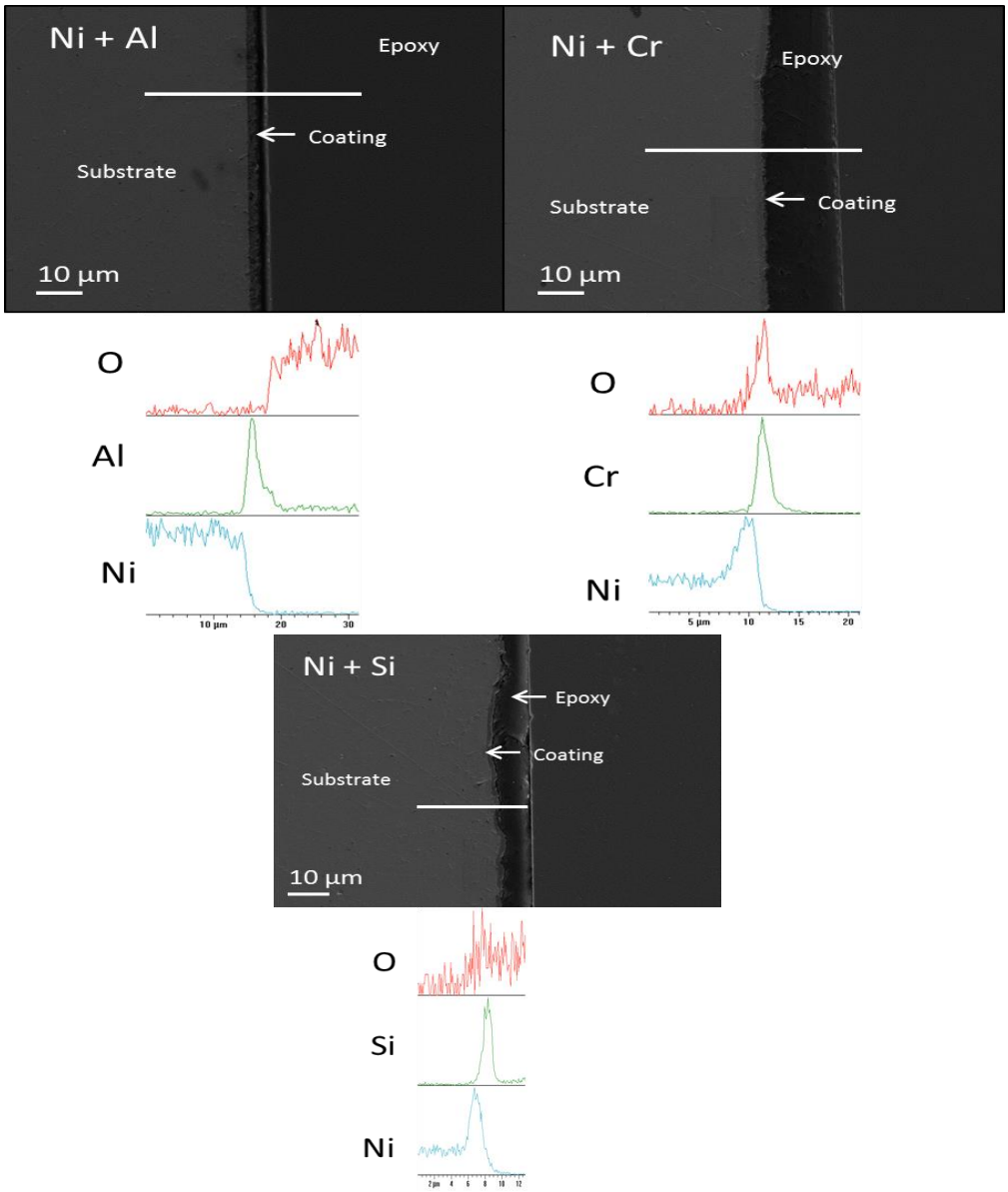

Figure 52: Ni-201 substrates following coating via PVD

The cross sections presented in Figure 52 demonstrate successful application of elemental coatings with a thickness of approximately 1 μm. Successful development of coatings of

the desired thickness illustrates the usefulness of magnetron sputtering PVD for coating development. It also appears that on the Cr coated sample oxide, likely Cr_2O_3 has formed.

Figure 53 presents the cross section data for samples oxidized at 700°C for 1 hour in flowing air/2 ppm $SO_{2\,(g)}$. These cross sections are examined for EDS overlap of metal elements and oxygen and sulfur, which could indicate possible formation of metal oxides, sulfides, or sulfates.

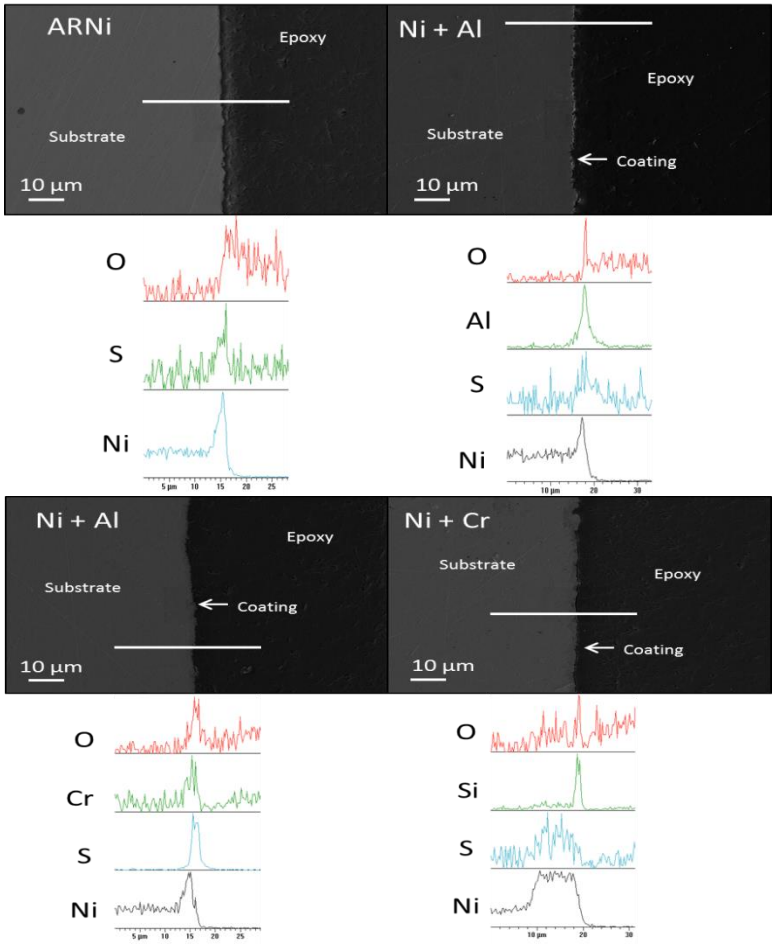

Figure 53: Cross section data for samples oxidized in flowing air/$SO_{2\,(g)}$ at 700°C for 1 hour

Cross sectional EDS scans show narrow zones of inter-diffusion occurring between coating elements and substrate. Over the course of this process intermetallic species such as nickel silicide ($NiSi_3$), chromium nickel (Cr_2Ni_3), and aluminum nickel ($AlNi_3$) may form. Additionally, data supports the likely formation of stable oxide species for Ni, Cr, Al, and Si. The formation of these oxides is predicted by the thermo-kinetic principles outlined earlier[4,6]. Limited evidence for the formation of metal sulfide or even potential sulfate species is presented by the overlap of the spectra of metal, sulfur, and oxygen signals. This suggests that the introduced $SO_{2\,(g)}$ is resulting in the requisite reactions for formation of ternary melts to occur if Na_2SO_4 had been present. The drop off in the EDS signal for Ni observed in each of the line-scans could potentially be due to a change in the energy between Ni compounds and elemental Ni. Alternatively, the reduced signal could simply be due increased distance from the sample due to a slope developed during the polishing process.

Figure 54 presents the cross section data for samples oxidized at 700°C for 100 hours in flowing air/2 ppm $SO_{2\,(g)}$. Samples are examined for evidence of the continuing inter-diffusion of coating and substrate materials as well as formation of oxides and sulfur containing species.

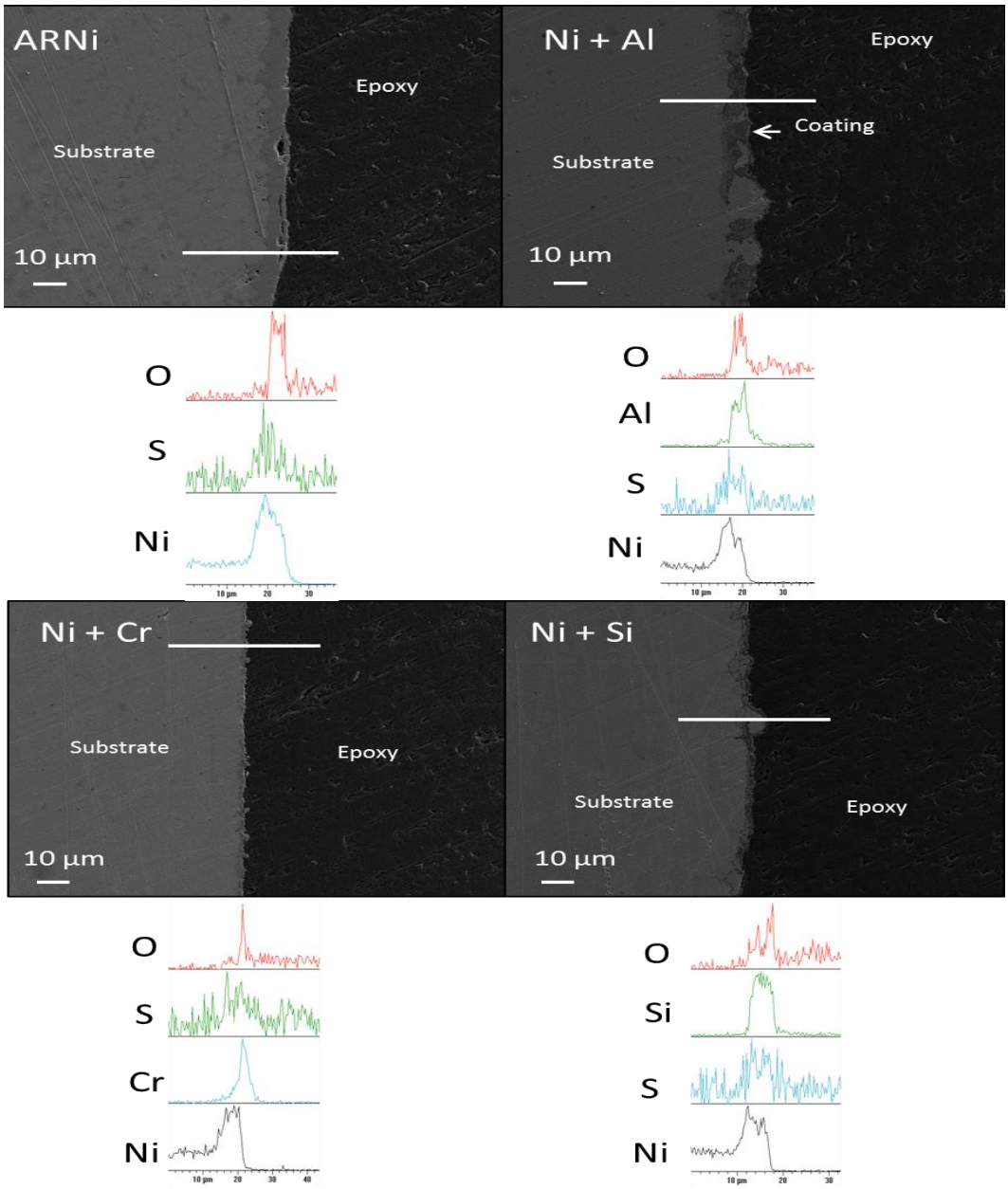

Figure 54: Cross section data for samples oxidized in flowing air/$SO_{2\,(g)}$ at 700°C for 100 hours

Data from Figure 54 indicates that for the described exposure inter-diffusion of metal species occurs. Additionally, data supports the likely formation of oxides and sulfur species as described previously for Figure 53.

Figure 55 presents the cross section data for samples oxidized at 700°C for 1 hour with a deposit of Na_2SO_4 in flowing air/2 ppm $SO_{2\ (g)}$. The additon of salt deposits could induce the formation of ternary melts.

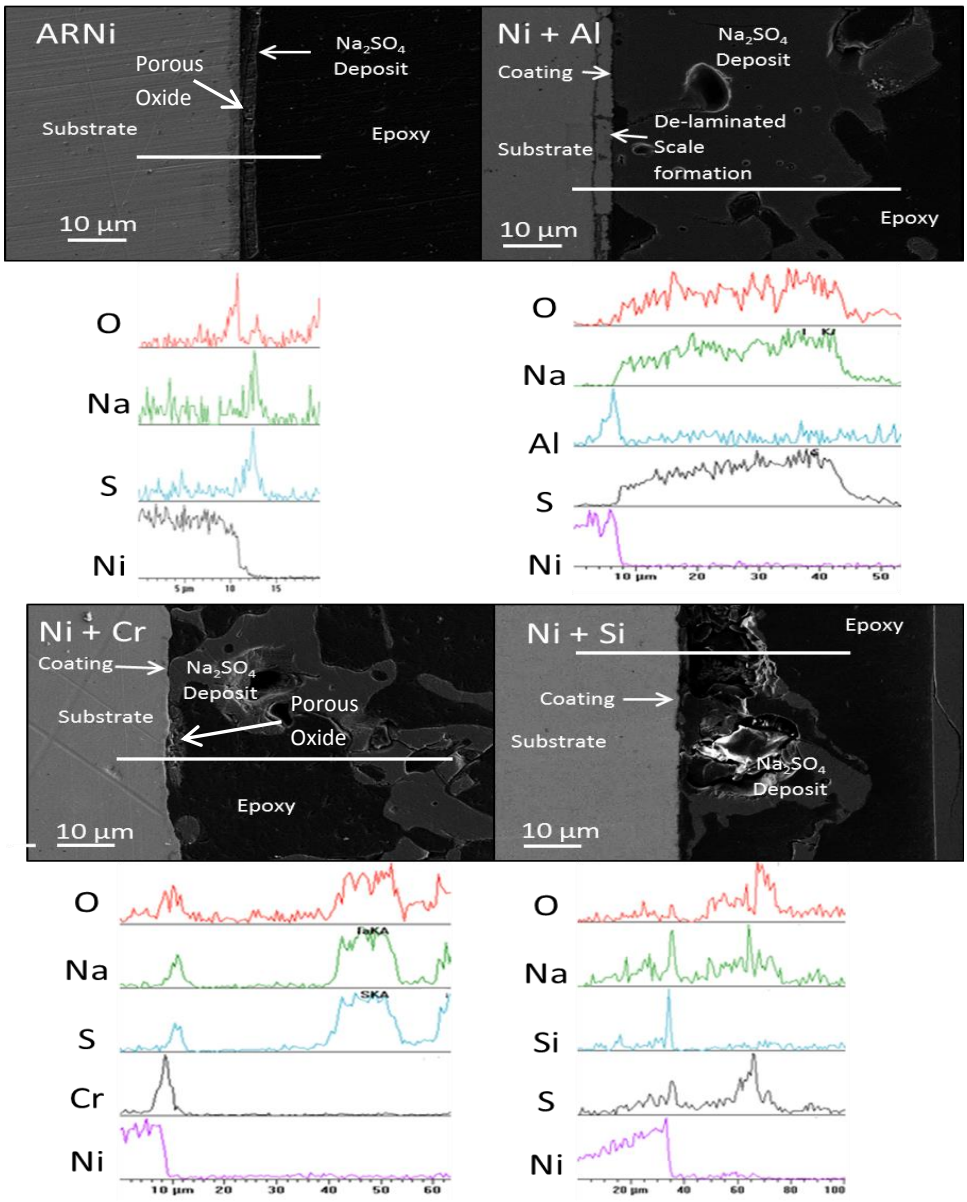

Figure 55: Cross section data for samples oxidized in flowing air/$SO_{2\ (g)}$ at 700°C for 1 hour with deposits of Na_2SO_4

Addition of Na_2SO_4 with $SO_{2\,(g)}$ in air, catalyzed to $SO_{3\,(g)}$, appears to result in the initiation of hot corrosion phenomena after 1 hour of oxidation. Development of metal oxide deposits that appear porous in nature match the description of non-protective oxides developed during hot corrosion[47]. In the case of the Al coating the formation of a delaminated scale could be attributed to the differing rates of oxidation between the elemental Al coating and the uncoated Ni available for reaction with diffusing gas species such as $\frac{1}{2}O_{2\,(g)}$ at grain boundaries[2,6]. As predicted by thermodynamics, Ni oxidizes more readily than Al perhaps inducing stress on the oxide scale[2]. As oxide grows within the grain boundary it induces lateral stress on the scale, which if sufficiently large can cause scale delamination, similar to that seen for the Ni + Al sample in Figure 6[2]. This result seems to reinforce the usefulness of single crystal components to avoid grain boundary effects for engine components such as turbine blades[7].

Figure 56 presents the cross section data for samples oxidized at 700°C for 100 hours with a deposit of Na_2SO_4 in flowing air/2 ppm $SO_{2\,(g)}$. Samples are examined for evidence of the continuing inter-diffusion of coating and substrate materials, formation of the ternary melts, and other effects associated with hot corrosion.

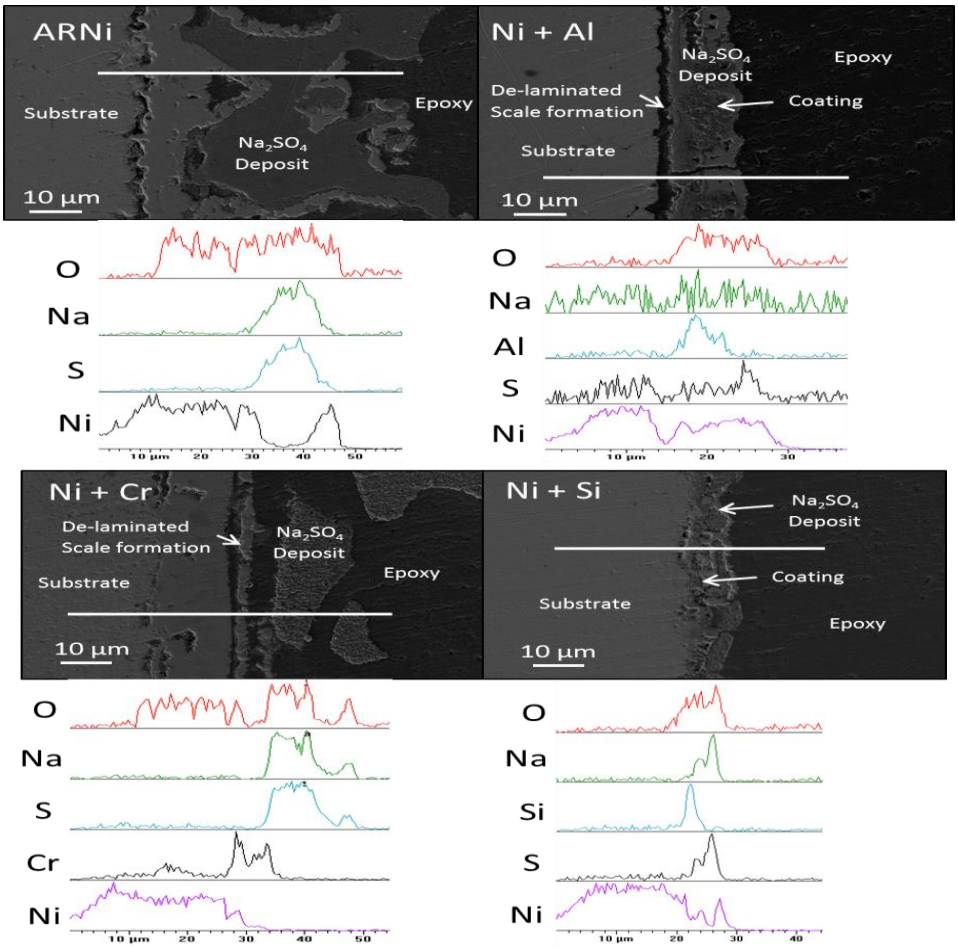

Figure 56: Cross section data for samples oxidized in flowing air/$SO_{2\,(g)}$ at 700°C for 100 hours with deposits of Na_2SO_4

Figure 56 illustrates the formation of porous oxide scales, present for all samples, shows the progression of hot corrosion phenomena [47]. The more widespread development of porous oxide scales over the course of exposure is perhaps due to requisite time for the formation of sulfur species, necessary for ternary melt species needed for hot corrosion [2,6,46]. Additionally, the formation of delaminated scales in all but the case of the Ni + Si samples also shows that the previously described grain boundary effects appear to persist during exposure. Finally, the increased range of coating and substrate elements suggests

that diffusion of these elements also continues. This result supports formation of intermetallic species described in regards to the results presented in Figure 53.

Cross sections for the samples oxidized for 1 hour at 900°C with a salt deposit, along with EDS elemental line scans are provided in Figure 57. Comparisons between cross sections of samples oxidized at 700°C will be drawn in order to observe differences in coating behavior between LTHC and HTHC phenomena.

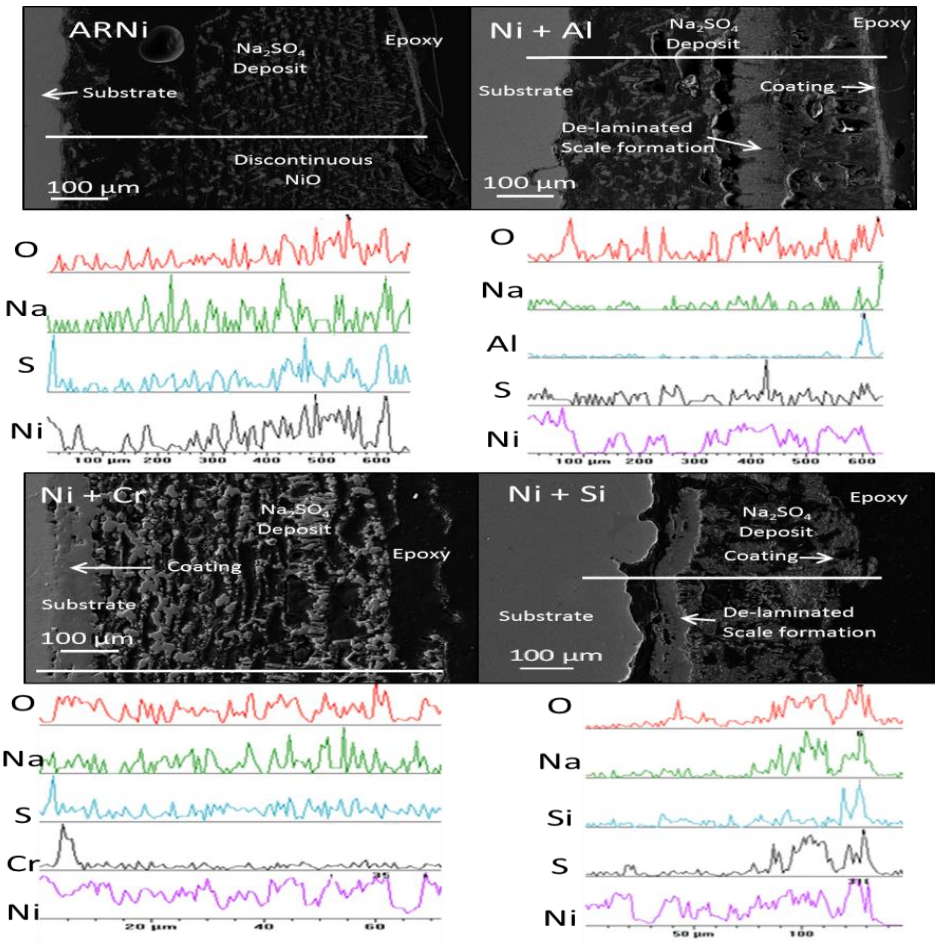

Figure 57: Cross sections for the samples oxidized for 1 hour at 900°C with a Na_2SO_4 deposit

Figure 57 shows that the phenomena observed during exposure at 700°C are again observed at 900°C, though with increased intensity. The increased formation of porous oxide and delamination of scale could be attributed to the higher kinetics associated with increased temperatures. Line scan analysis shows an appreciable amount of nickel on the side of the chromium coating in contact with the salt deposit and atmosphere, an occurrence not observed in other coatings. This result suggests that the chromium coating was ineffective in forming an effective barrier to diffusion of nickel ions through the surface coating and into the salt layer. This may be due to the more rapid inter-diffusion and formation of complexes of the Ni-Al and Ni-Si systems. As previously mentioned it has been observed in Ni-Al-Cr systems that the inter-diffusion of Ni and Al occurs more rapidly [70]. Such movement would likely decrease the concentration gradient between the coatings and substrate perhaps slowing the rate of diffusion from the substrate during hot corrosion.

Cross sections for the samples oxidized for 100 hours at 900°C with a salt deposit in stagnant lab air, along with EDS elemental line scans are provided in Figure 58. Comparisons between cross sections of samples oxidized at 900°C for 1 hour will be drawn in order to observe the progression of HTHC.

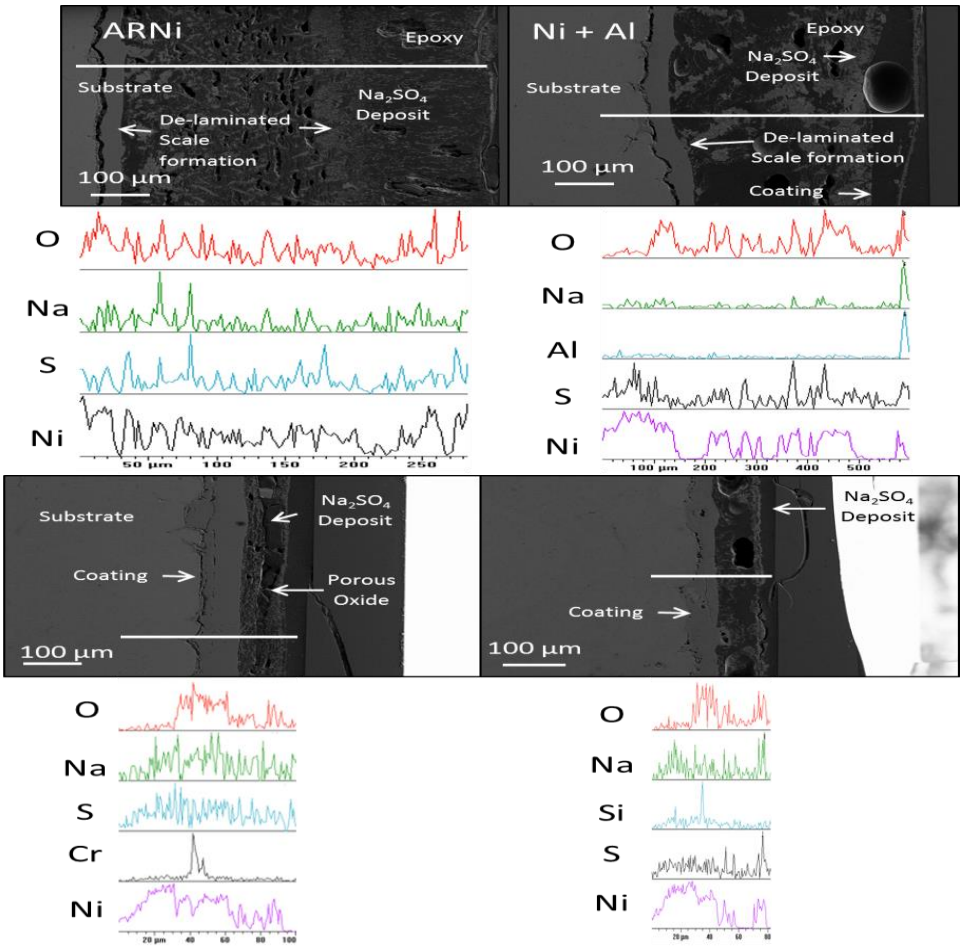

Figure 58: Cross sections for the samples oxidized for 100 hours at 900°C with a Na_2SO_4 deposit

All coatings appear to allow some formation of sulfur-nickel compounds in the underlying substrate, suggesting that at least some diffusion of species is free to occur from the coupon surface-gas interface through the coating and into the underlying substrate. Sulfur accumulation below oxide scales has been observed to correspond to poor scale adherence and in particular spallation [71]. If sulfur is diffusing into a position between the formed scale and the substrate as the line scan data suggests this may explain the instances of spallation. Spallation has been observed primarily on the Al coated samples which don't appear to have a corresponding spike in sub scale sulfur.

Additionally, diffusion of sulfur into contact with the Ni substrate making sulfur ions available for reaction is an important indication that sulfidation based hot corrosion may be occurring [6,46,47]. The signal for sulfur is significantly lower in coated samples when compared to the uncoated nickel, suggesting that resistance to this form of corrosion is also improved by the presence of coatings.

3.5 X-Ray Diffraction:

Phase characterization through XRD analysis can confirm inter-diffusion of substrate and coating elements. During the diffusion process formation of intermetallic compounds occurs that can then be detected by XRD. These patterns are presented for as received Ni-201 and coated Ni-201 in Figure 59.

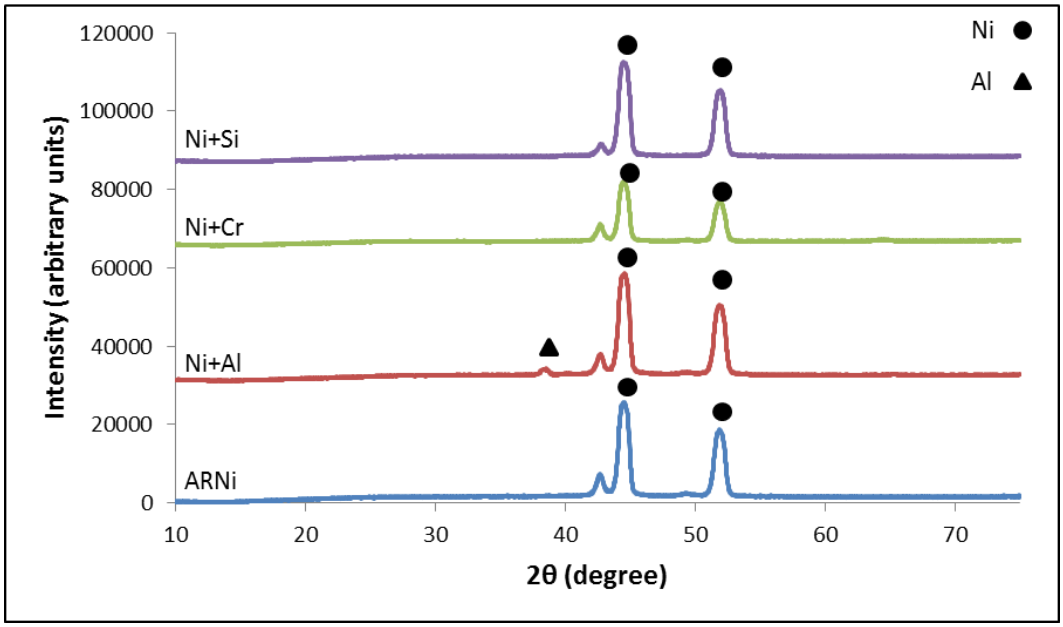

Figure 59: XRD pattern for as coated and uncoated Ni-201 samples

Figure 59 displays the XRD patterns for coated and uncoated samples prior to oxidation. Limited evidence for the coating materials appears in these patterns, confirming that the theoretical penetrance of the beam and validating its utility for observing the formation of intermetallic species formed during inter-diffusion.

The XRD patterns for coated and uncoated Ni-201 samples oxidized for 1 hour in stagnant lab air at 700°C are presented in Figure 60. Note that to reduce clutter the peak labels for elemental Ni, Al, Cr, and Si are not labeled.

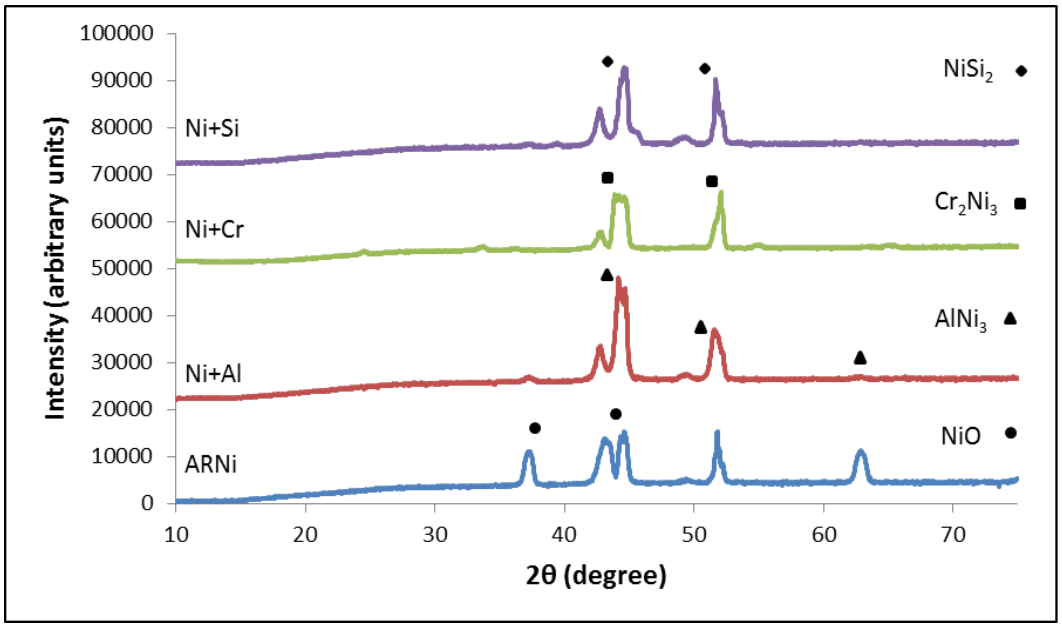

Figure 60: XRD pattern for coated and uncoated Ni-201 samples following oxidation at 700°C for 1 hour

The XRD patterns presented in Figure 60 shows evidence for the formation of the predicted intermetallic species between substrate and coating elements. This result confirms that the coating elements actively diffuse into the substrate concurrent with oxidation. Similar processes have previously been associated with the development of

diffusion coatings[72]. Additionally, the XRD patterns further support inter-diffusion of substrate and coating elements as suggested by the results of the cross section analysis.

Rapid inter-diffusion and formation of intermetallic compounds may decrease the concentration gradient between the coatings and substrate. The lowering of this gradient could perhaps result in a slowing of the rate of lattice diffusion from the substrate to the coating during oxidation. As discussed previously, slowing the rate of ionic diffusion is an important element of corrosion protection[6]. For example, previous studies have indicated that the activation energy for diffusion in Ni-Al systems increases when the mole fractions near 0.5[73]. This effect could be especially pronounced for Al, as it has been observed in Ni-Al-Cr systems that the inter-diffusion of Ni and Al occurs more rapidly than Ni and Cr[70].

The XRD patterns for coated and uncoated Ni-201 samples oxidized for 100 hours in stagnant lab air at 700°C are presented in Figure 61. Note that to reduce clutter the peak labels for elemental Ni, Al, Cr, and Si are not labeled.

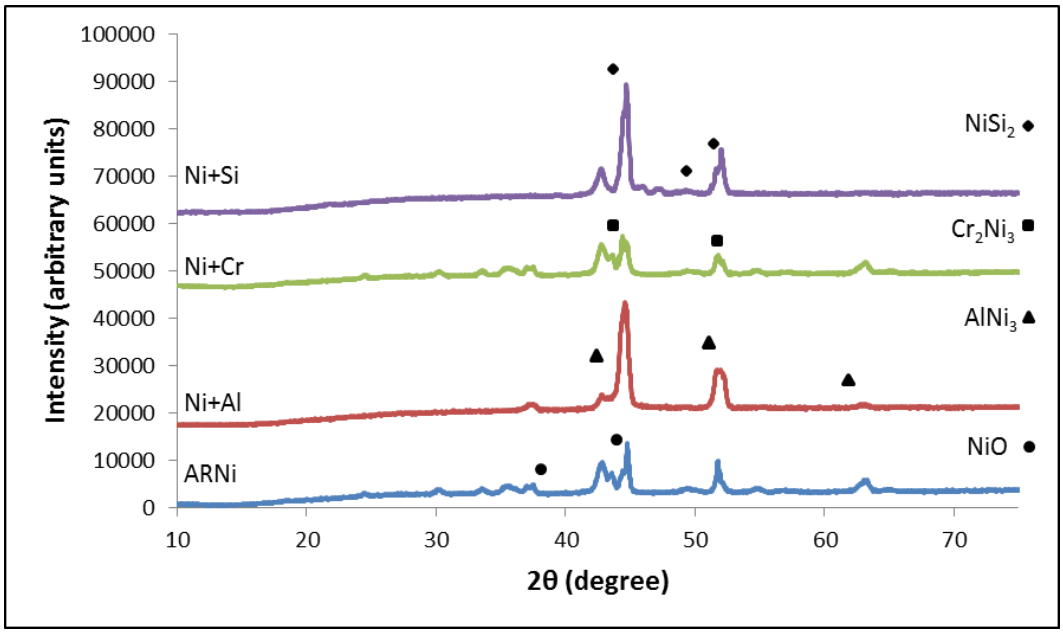

Figure 61: XRD pattern for coated and uncoated Ni-201 samples following oxidation at 700°C for 100 hours

Figure 61 shows evidence for the continuing development of the intermetallic species, namely nickel silicide ($NiSi_3$), chromium nickel (Cr_2Ni_3), and aluminum nickel ($AlNi_3$), following oxidation in stagnant lab air at 700°C for 100 hours. The results imply that either the formation of the intermetallic species occurs over the course of exposure or that the formed species are stable at 700°C.

The XRD patterns for coated and uncoated Ni-201 samples oxidized for 1 hour in flowing air/$SO_{2\,(g)}$ at 700°C are presented in Figure 62. Note that to reduce clutter the peak labels for elemental Ni, Al, Cr, and Si are not labeled.

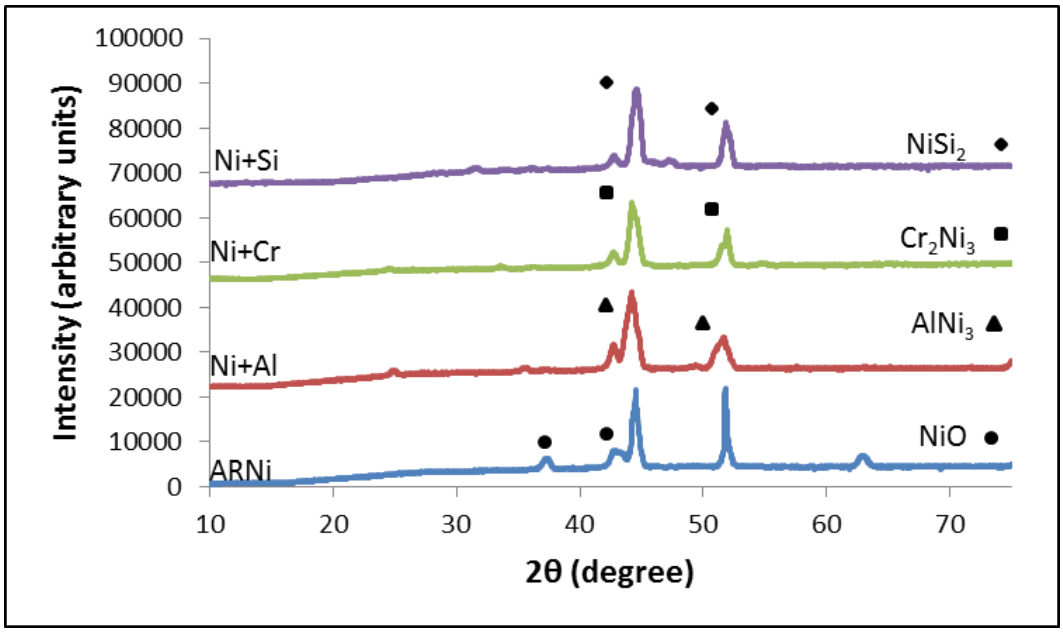

Figure 62: XRD patterns following oxidation at 700°C in flowing air/$SO_{2\,(g)}$ 1 hour

Figure 62 presents further evidence of intermetallic formation. The findings appear to agree with the results presented in Figure 59. Inclusion of $SO_{2\,(g)}$ does not appear to significantly alter the species formed following an hour of exposure.

The XRD patterns for coated and uncoated Ni-201 samples oxidized for 100 hours in flowing air/$SO_{2\,(g)}$ at 700°C are presented in Figure 63. Note that to reduce clutter the peak labels for elemental Ni, Al, Cr, and Si are not labeled.

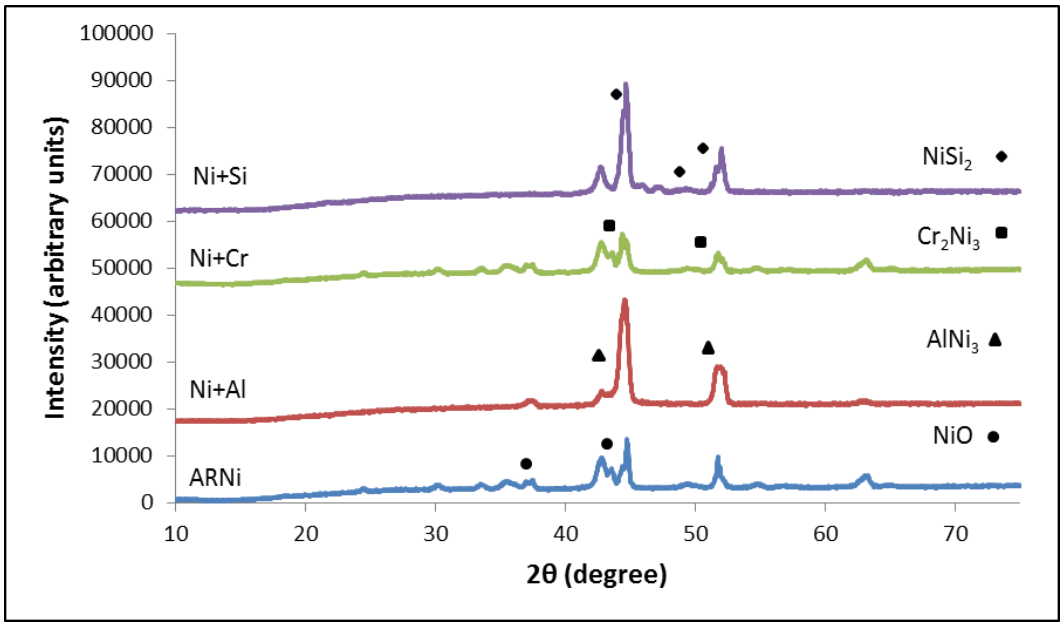

Figure 63: XRD patterns following oxidation at 700°C in $SO_{2\,(g)}$ 100 hours

Figure 63 seems to support previous evidence that formed species either persist or continue to form over the course of exposure. Once again patterns do not indicate any significant difference occurring between samples oxidized in flowing $SO_{2\,(g)}$ and those in stagnant lab air.

The XRD patterns for coated and uncoated Ni-201 samples oxidized for 1 hour in stagnant lab air at 900°C are presented in Figure 64. Note that to reduce clutter the peak labels for elemental Ni, Al, Cr, and Si are not labeled.

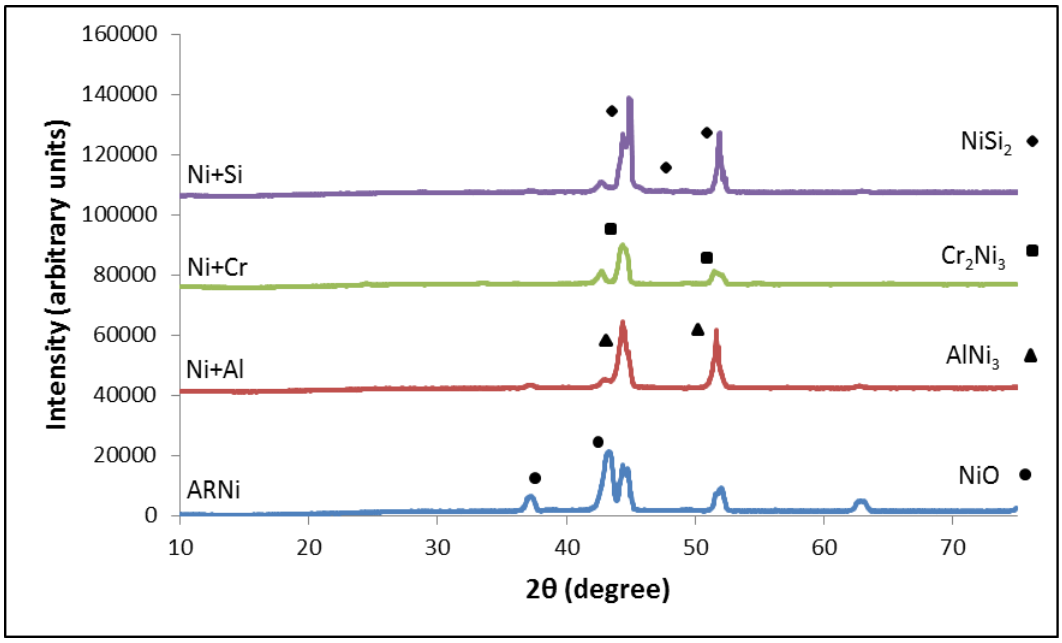

Figure 64: XRD patterns following oxidation at 900°C for 1 hour

Following oxidation in stagnant lab air at 900°C for 1 hour patterns indicating development of intermetallic species are again observed. For Cr and Al coated samples, Cr and Al peak shoulders deviate from those identified on uncoated samples as Ni and NiO revealing species formed by interaction between coating and substrate elements. This result, combined with the EDS data, suggests that the coating elements actively diffuse into the substrate concurrent with oxidation at 900°C similarly to the results for oxidation at 700°C. The species present are also identical, with differences in intensity, to those formed during oxidation at 700°C.

The XRD patterns for coated and uncoated Ni-201 samples oxidized for 100 hours in stagnant lab air at 900°C are presented in Figure 65. Note that to reduce clutter the peak labels for elemental Ni, Al, Cr, and Si are not labeled.

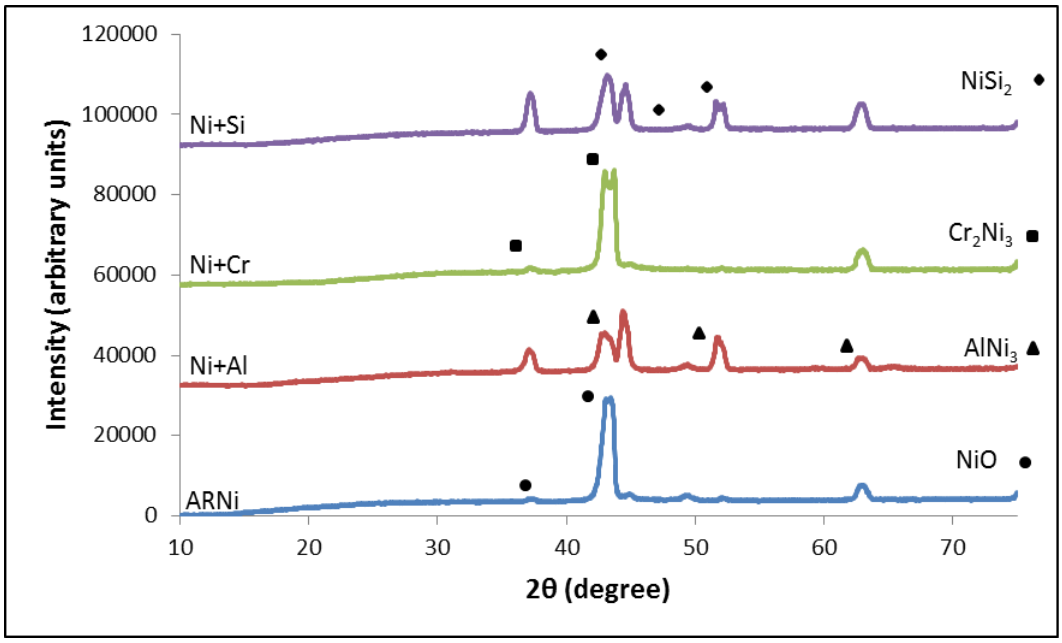

Figure 65: XRD patterns following oxidation at 900°C for 100 hours

The patterns presented in Figure 65 shows that intermetallic compounds are maintained throughout the course of oxidation at 900°C. Once again the presence of intermetallic species if they are stable, suggest that the intermetallic species formed could offer some protection over the course of oxidation at 900°C.

The XRD patterns for coated and uncoated Ni-201 samples oxidized for 1 hour in flowing air/$SO_{2\,(g)}$ at 700°C with a Na_2SO_4 deposit are presented in Figure 66. Note that to reduce clutter the peak labels for elemental Ni, Al, Cr, and Si are not labeled.

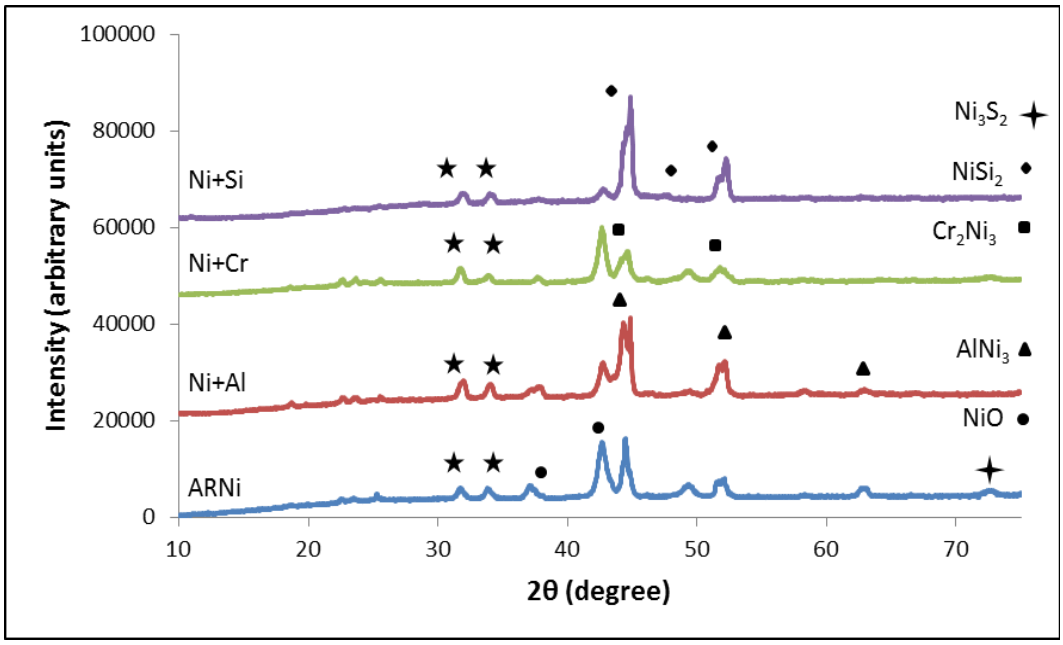

Figure 66: XRD patterns following oxidation at 700°C $SO_{2\,(g)}$ with a Na_2SO_4 deposit 1 hour

Figure 66 shows more evidence for continued formation of intermetallic formation over the course of oxidation at 700°C in $SO_{2\,(g)}$. The signal for nickel sulfide (Ni_3S_2) shows evidence for sulfide formation similar to that described during formation of ternary melts during LTHC[2,6,46,47]. The lack of a signal for this sulfide in samples exposed only to the flowing SO_2 gas without a salt deposit suggests that the presence of the salt is also required for sulfide formation. Formation of these sulfide species could be responsible for the increased mass gain observed during exposure to flowing $SO_{2\,(g)}$. This evidence occurred only on the bare Ni-201 samples indicating that coatings may offer some protection from this reaction.

The XRD patterns for coated and uncoated Ni-201 samples oxidized for 100 hours in flowing air/$SO_{2\,(g)}$ at 700°C with a Na_2SO_4 deposit are presented in Figure 67. Note that to reduce clutter the peak labels for elemental Ni, Al, Cr, and Si are not labeled.

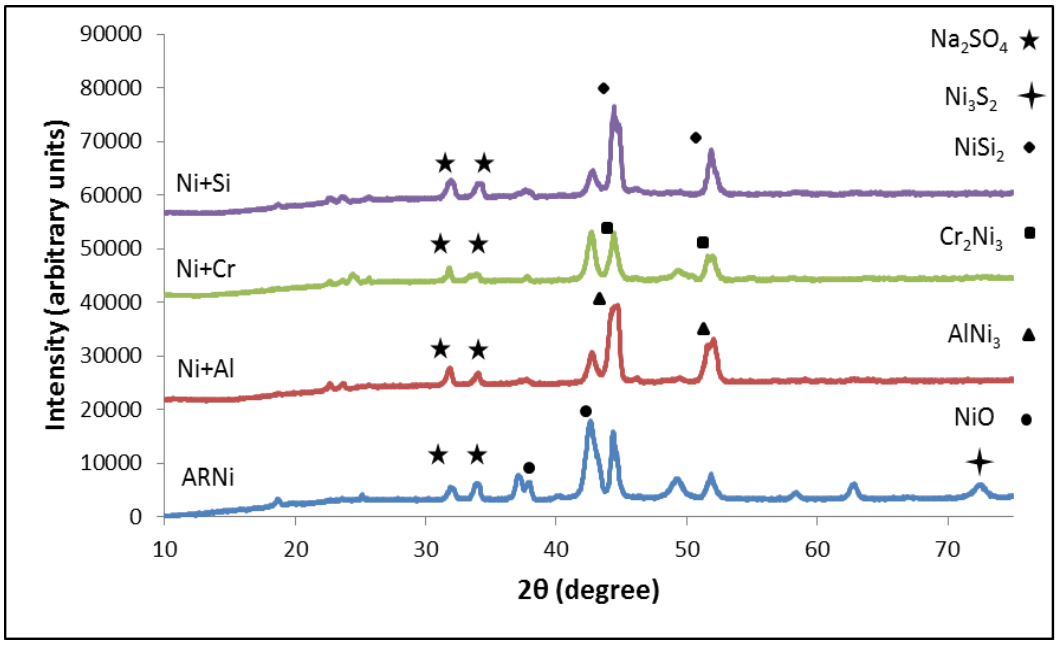

Figure 67: XRD patterns following oxidation at 700°C $SO_{2\,(g)}$ with a Na_2SO_4 deposit 100 hours

Figure 67 again shows the signal for Ni_3S_2 indicating that when $SO_{2\,(g)}$ is introduced along with a Na_2SO_4 deposit the sulfide persists over the course of oxidation.

The XRD patterns for coated and uncoated Ni-201 samples oxidized for 1 hour in stagnant lab air at 900°C with a Na_2SO_4 deposit are presented in Figure 68. Note that to reduce clutter the peak labels for elemental Ni, Al, Cr, and Si are not labeled.

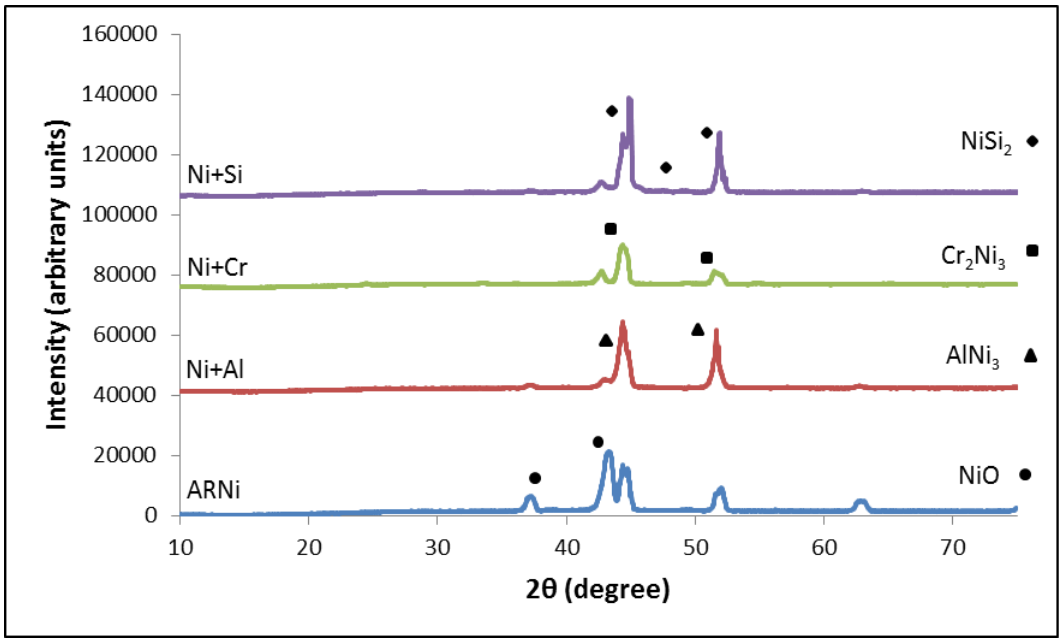

Figure 68: XRD patterns following oxidation at 900°C with a Na_2SO_4 deposit 1 hour

The lack of any signal for Ni_3S_2 at 900°C even when a Na_2SO_4 deposit is introduced implies that $SO_{2\,(g)}$ plays an important role in the formation of the sulfide species.

3.6 Inductively Coupled Plasma Mass Spectroscopy:

The results of analysis by ICP-MS results for samples oxidized at 700°C in stagnant lab air, 700°C in flowing air/SO_2 mixture, and 900°C in stagnant lab air for 10 hours with a 3 mg/cm^2 Na_2SO_4 deposit and prepared per the materials and method section are presented in Tables 8-10. Data for the additional two trials conducted are presented in Appendix A.

Table 8: ICP-MS of samples oxidized at 700°C in stagnant lab air

700°C	Parts Per Million (ppm)			
Sample	Al	Cr	Ni	Si
Ni + Al	125	19	19	12
Ni + Cr	3	2,440	12	12
ARNi	4	29	10	23
Ni + Si	5	12	13	125

Table 9: ICP-MS of samples oxidized at 700°C in flowing air/SO_2 mixture

700°C+SO_2	Parts Per Million (ppm)			
Sample	Al	Cr	Ni	Si
Ni + Al	66	17	13	6
Ni + Cr	5	3,390	185	5
ARNi	2	21	27	10
Ni + Si	1	11	525	201

Table 10: ICP-MS of samples oxidized at 900°C in stagnant lab air

900°C	Parts Per Million (ppm)			
Sample	Al	Cr	Ni	Si
Ni + Al	6,150	214	715,000	465
Ni + Cr	760	3,790	2,430,000	305
ARNi	801	218	723,000	453
Ni + Si	939	655	637,000	8,840

Results indicate significant transport of coating material into the deposited salt layer occurred for all but the Ni + Al sample. The uncoated Ni sample displayed one of the lower concentrations for movement of Ni into the deposited salt. This could be due to the preparation of the samples for analysis. The deposit was removed following oxidation mechanically and then diluted prior to analysis. Samples with lose surface material, such as delaminated scales or spalled material, may have a positive bias in regards to the concentration of metallic species present within the melt. While delaminated or spalled oxide species offer no protection to the underlying metal, the material does not accurately reflect the quantity of species dissolved in the melt.

In the case of samples having coatings with significant differences in thermal coefficients of expansion between coating element, and substrate, such as in the case for Cr the delamination of coating material from the surface during thermal cycling is likely[2]. Lose material consistent with ejected Cr-Ni scale was observed in the material sent for analysis. Varying amounts of delaminated scale collection per sample could be the reason for the poor reproducibility exhibited over the course of the three trials conducted. In the case of Si, the slower rate of oxidation predicted by kinetics could have led to coating removal by scale deformation through the mechanisms discussed previously. The Al coating may have lost material to similar mechanisms but appears to have lost significantly less material to the deposit than the other coatings. Additionally, less Ni was found in the deposit for the Al coated sample, supporting line-scan EDS spectra evidence that the Al thin film may have formed an effective barrier to ionic diffusion.

CONCLUSIONS

Single element coatings of Al, Cr, and Si ~1 μm thick were deposited on Ni-201 using magnetron sputtering PVD. Coated and uncoated samples were then subjected to temperatures up to 900°C in stagnant lab air and flowing air/$SO_{2\,(g)}$. Samples then had Na_2SO_4 deposits added and were subject to identical conditions. These samples were then examined for signs of the phenomena associated with hot corrosion using a variety of analysis techniques. The study also resulted in a methodology for development, exposure to corrosive environments, characterization, and analysis of the corrosion resistance properties of overlay coatings.

Current investigations demonstrate that the described 1 μm coatings of Al, Cr, and Si significantly altered the oxidation behavior of Ni-201 substrates in high temperature environments. Evidence for the formation of ternary melts was observed at 700°C, particularly when $SO_{2\,(g)}$ was introduced. When exposed to temperatures of 900°C it was observed that coatings of Al and Si produced a barrier to the diffusion of Ni to the surface of the sample coupons in the presence of Na_2SO_4, while Cr did not produce a similar effect. This effect could be due to a lowering of the concentration gradient between coating and substrate in the more rapidly inter-diffusing Ni-Al and Ni-Si systems. In support of this concept, XRD data suggested that coating elements diffused readily into the substrate and there formed intermetallic compounds.

Data indicated that ~1 μm coatings are likely too thin for practical applications due to the limited amount of protective material between substrate and environment. Additionally, the effects of oxidation at grain boundaries, frequently resulting in scale

delamination, are unlikely to be prevented by such thin coatings. The primary value of current experiments is demonstration of the utility of the described approach for preparing and analyzing samples within high temperature environments known to promote hot corrosion phenomena. The techniques and capabilities developed facilitate rapid coating development, characterization, exposure, and analysis of behavior under the described conditions.

Expansion of the project could involve determining the cause of the altered surface morphology observed between stagnant lab air and flowing air/$SO_{2\,(g)}$ mixture. Additionally, rates of deposition via magnetron sputtering PVD have been observed to scale nearly linearly with power, allowing for synchronization of deposition rates between materials. Coating substrates using two and three targets depositing simultaneously would result in a "library" of elemental compositions. Multiple element coatings would provide an opportunity to investigate the potentially synergistic effects of elemental composition on corrosion behavior. Studies would expand upon other works examining the use of PVD methods for rapid alloy development[74]. Another line of inquiry could involve exposure of coatings applied to single crystal substrates with a goal of determining if observed scale delamination is a consequence of preferential oxidation occurring at grain boundaries originating in the substrate. Alternatively, repeating current exposures employing an inert substrate with single and multiple element coatings would provide an opportunity to investigate coating behavior independently of the substrate. Finally, coatings applied for practical applications are likely to be pre-oxidized to promote development of protective oxide layers and the intermetallic species[12].

Repeating experiments with pre-oxidation treatments of the coated samples would provide insight into the differences in corrosion behavior between treated and untreated coatings. The results of these experiments could subsequently allow for informed rapid development of heat treated overlay coatings.

REFERENCES CITED

1. Cohen, H., Rogers, G. F. C. & Saravanamuttoo, H. I. H. *Gas Turbine Theory*. (Burnt Mill: Harlow, Essex, England, 1987).

2. Young, D. *High Temperature Oxidation and Corrosion of Metals*. (Elsevier: Oxford, 2008).

3. Eliaz, N., Shemesh, G. & Latanision, R. M. Hot corrosion in gas turbine components. *Engineering Failure Analysis* **9**, 31–43 (2002).

4. Smialek, J. L. & Jacobson, N. S. Oxidation of High Temperature Aerospace Materials. *Corrosion High Temperature Aerospace Materials* Chapter 6 (2012).

5. MacKay, R. A., Gabb, T. P., Smialek, J. L. & Nathal, M. V. *Low-Density, Creep-Resistant Superalloys Developed for Turbine Blades*. (Cleveland, OH, 2007).at <http://www.grc.nasa.gov/WWW/RT/2006/RX/RX02-mackay.html>

6. Birks, N., Meier, G. H. & Pettit, F. S. *Introduction to the High-Temperature oxidation of Metals*. (Cambridge University Press: Cambridge, New York, 2006).

7. Reed, R. C. *The Superalloys: Fundamentals and Applications*. (Cambridge University Press: Cambridge, New York, 2006).

8. Gleeson, B. & Mu, N. Compositional factors affecting the establishment and maintenance of Al2O3 scales on Ni-Al-Pt systems. *Journal of Materials Science* **44**, 1704–1710 (2009).

9. Gleeson, B. & Mu, N. Compositional factors affecting the establishment and maintenance of Al2O3 scales on Ni-Al-Pt systems. *Journal of Materials Science* **44**, 1704–1710 (2009).

10. Opila, E. High Temperature Materials Corrosion Challenges for Energy Conversion Technologies. *The Electrochemical Society: Interface* **22**, 69–73 (2013).

11. Goward, G. . Progress in coatings for gas turbine airfoils. *Surface and Coatings Technology* **108-109**, 73–79 (1998).

12. Guo, H., Xu, H. & Gong, S. A study on gradient thermal barrier coatings by EB-PVD in a cyclic high-temperature hot-corrosion environment. **7**, 5333–5337 (2002).

13. Li, J. J., Li, M. S., Xiang, H. M., Lu, X. P. & Zhou, Y. C. Short-term oxidation resistance and degradation of Cr2AlC coating on M38G superalloy at 900–1100°C. *Corrosion Science* **53**, 3813–3820 (2011).

14. Deodeshmukh, V. & Gleeson, B. Evaluation of the hot corrosion resistance of commercial β-NiAl and developmental γ′-Ni3Al+γ-Ni-based coatings. *Surface and Coatings Technology* **202**, 643–647 (2007).

15. Nicholls, J. R., Hancock, P. & Al Yasiri, L. H. Optimising Oxidation Resistance of MCrAlY Coating Systems using Vapour Phase Alloy Design. *Materials Science and Technology* **5**, 799–805 (1989).

16. Nicholls, J. R., Lawson, K. J., Al Yasiri, L. H. & Hancock, P. Vapour Phase Alloy Design of Corrosion-Resistant Overlay Coatings. *Corrosion Science1* **35**, 1209–1223 (1993).

17. Wang, Q. M. *et al.* Fabrication and oxidation behavior of Cr2AlC coating on Ti6242 alloy. *Surface and Coatings Technology* **204**, 2343–2352 (2010).

18. Wang, Q. M. *et al.* Improving the high-temperature oxidation resistance of a β–γ TiAl alloy by a Cr2AlC coating. *Corrosion Science* **52**, 3793–3802 (2010).

19. Jun, S.-I., Rack, P. D., McKnight, T. E., Melechko, A. V. & Simpson, M. L. Low-temperature solid-phase crystallization of amorphous silicon thin films deposited by rf magnetron sputtering with substrate bias. *Applied Physics Letters* **89**, 022104 (2006).

20. Warnes, B. M., Pettit, F. S. & Meier, G. H. Hot-Corrosion Resistance of Ni-Cr-Al-Y and Ni-18% Si Alloys in Sulfate Eutectic and Sulfate Plus Vanadate Melts at 973 K. *Oxidation of Metals* **58**, 487–498 (2002).

21. Mattox, D. M. *Handbook of Physical Vapor Desposition (PVD) Processing*. (Elsevier: 2010).

22. Ohring, M. *Materials Science of Thin Films*. (Elsevier: San Diego, 2002).

23. Brassine, C. & Prignon, Y. Nanomateriaux: depots sous vide et realisation de foils metalliques. *Metallurgie et Science des Materiaux* (2006).at <http://www.metaux.ulg.ac.be/metaux/index.php?page=nanomateriaux>

24. Ohring, M. *Materials Science of Thin Films*. (Elsevier: San Diego, 2002).

25. Vossen, J. L. & Cuomo, J. J. Glow Discharge Sputter Deposition. *Thin Film Processes* Section II–1 (1978).

26. Jun, S.-I., Rack, P. D., McKnight, T. E., Melechko, A. V. & Simpson, M. L. Direct-current substrate bias effects on amorphous silicon sputter-deposited films for thin film transistor fabrication. *Applied Physics Letters* **87**, 132108 (2005).

27. Tester, J. W. & Modell, M. *Thermodynamics and Its Applications*. (Prentice Hall PTR: Upper Saddle River, New Jersey, 1997).

28. Kofstad, P. *Nonstoichiometry, diffusion, and electrical conductivity in binary metal oxides*. (Wiley-Interscience: 1972).

29. Benard, J. *Oxydaion des Meteaux*. (Gautier-Villars: Paris, 1962).

30. Mott, N. F. No Title. *Trans. Faraday Soc.* **36**, 472 (1940).

31. Hauffe, K. & Ilschner, B. Z. No Title. *Elektrochem.* **58**, 382 (1954).

32. Evans, U. R. *The Corrosion and Oxidation of Metals*. (Edward Arnold: London, 1960).

33. Perrow, J. M., Smeltzer, W. W. & Embury, J. D. No Title. *Acta Metallurgica* **16**, 1209–1218 (1968).

34. Stolyarova, V. L., Lopatin, S. I. & Shugurov, S. M. Thermodynamic properties of gaseous salts formed by Nickel(II) oxide. *Doklady Physical Chemistry* **406**, 27–29 (2006).

35. Prescott, R. & Graham, M. J. The Formation of Alumium Oxide Scales on High-Temperature Alloys. *Oxidation of Metals* **38**, 233–254 (1992).

36. Bose, S. *High Temperature Coatings*. (Elsevier: Boston, 2007).

37. Opila, E. J. & Myers, D. L. Alumina Volatility in Water Vapor at Elevated Temperatures. **1705**, 1701–1705 (2004).

38. Carter, P., Gleeson, B. & Young, D. J. Rapid Growth of SiO 2 Nanofibers on Silicon-Bearing Alloys. *Oxidation of Metals* **56**, (2001).

39. Pilling, N. B. & Bedworth, R. E. The Oxidatin of Metals at High Temperatures. *Institute of Metals* **29**, 529–591 (1923).

40. Young, D. J. *High Temperature Oxidation and Corrosion of Metals*. (Elsevier: Oxford, 2008).

41. Srolovitz, D. J. & Ramanarayanan, T. a. An elastic analysis of growth stresses during oxidation. *Oxidation of Metals* **22**, 133–146 (1984).

42. Tylecote, R. F. Factors influencing the adherence of oxides on metals. *J. Iron Steel Inst.* **196**, 135–141 (1960).

43. Robertson, J. & Manning, M. I. Limits to adherece of oxide scales. *Mater. Sci. Technol.* **6**, 81–91 (1990).

44. Tien, J. K. & Davidson, J. M. No Title. *Adv. Corros. Sci. Technol.* **7**, (1980).

45. Tada, H. *et al.* Thermal expansion coefficient of polycrystalline silicon and silicon dioxide thin films at high temperatures. *Journal of Applied Physics* **87**, 4189 (2000).

46. Pettit, F. Hot Corrosion of Metals and Alloys. *Oxidation of Metals* **76**, 1–21 (2011).

47. Rapp, R. A. Hot corrosion of materials : a Fluxing mechanism ? *Corrosion Science* **44**, 209–221 (2002).

48. Luthra, K. L. Kinetics of the Low Temperature Hot Corrosion of Co-Cr-Al Alloys. *Journal of The Electrochemical Society* **132**, 1293 (1985).

49. Stringer, J. Hot corrosion of high-temperature alloys. *Annual Review of Materials Science* 477–509 (1977).at <http://www.annualreviews.org/doi/pdf/10.1146/annurev.ms.07.080177.002401>

50. Kohl, F. J., Stearns, C. A. & Fryburg, G. C. *Sodium Sulfate: Vaporization Thermodynamics and Role in Corrosive Flames*. *Technical Paper for the Electrochemical Society* (Toronto, Canada, 1975).

51. Park, C. O. & Rapp, R. A. Electrochemical Reactions in Molten Na2SO4at 900 ~. **05**, 1636–1641 (1986).

52. Park, C. O. & Rapp, R. A. Electrochemical Reactions in Molten Na2SO4at 900 ~. **05**, 1636–1641 (1986).

53. Lawson, M. G., Pettit, F. S. & Blachere, J. R. Hot corrosion of alumina. *Journal of Materials Research* **8**, 1964–1971 (1993).

54. Gupta, D. K. & Rapp, R. A. The Solubilities of NiO, Co O4, and Ternary Oxides in Fused Na SO at 1200~. 2194–2202 (1980).

55. Jose, P. D., Gupta, D. K. & Rapp, R. A. Solubility of α-Al2O3 in Fused Na2SO4 at 1200K. *Journal of The Electrochemical Society:Solid-State Science and Technology*. **132**, 735–737 (1985).

56. Zhang, Y. S. Solubilities of Cr2O3 in Fused Na2SO4 at 1200K. *Journal of the Electrochemical Society: Solid-State Science and Technology* **133**, 655–657 (1986).

57. Shi, D. & Rapp, R. A. The solubility of SiO2 in Fused Na2SO4 at 900°C. *The solubility of SiO2 in Fused Na2SO4 at 900°C* **133**, 849–850 (1986).

58. Rapp, R. A. & Goto, K. S. Molten Salts. *Molten Salts* 159 (1981).

59. Otsuka, N. & Rapp, R. A. Hot Corrosion of Preoxidized Ni by a Thin Fused Na2S04 Film // Acidic. **137**, 46–52 (1990).

60. Otsuka, N. & Rapp, R. A. Hot Corrosion of Preoxidized Ni by a Thin Fused Na2S04 Film // Acidic. **137**, 46–52 (1990).

61. Lillerud, K. P. & Kofstad, P. Sulfate-Induced Hot Corrosion of Nickel. *Oxidation of Metals* **21**, (1984).

62. Bol'shakov, K. A. & Fdorov, P. I. No Title. *Russian Journal of Organic Chemistry* **3**,

63. Wu, W. T., Rahmel, A. & Schorrt, M. Role of Platinum in the Na2SO4-Induced Hot Corrosion Resistance of Aluminum Duffusion Coatings. **22**, 59–81 (1984).

64. ISO/WD17224 *Corrosion of Metals and Alloys-Test method for high-temperature corrosion testing of metallic materials by application of a deposit of salt, ash, or other substances*. (2012).

65. Allegheny Technologies Incorporated Properties *Technical Data Sheet*. 2 (2012).

66. Imaging and Chemical Analysis Laboratory. (2011).at <http://www.physics.montana.edu/ical/home/index.asp>

67. Imaging and Chemical Analysis Laboratory. (2011).

68. Morales, F. *Applications Lab Report*. (Rancho Dominguez, 2013).

69. Morales, F. *Applications Lab Report*. (Rancho Dominguez, 2013).

70. Hou, G. C. *et al.* Interdiffusion in the β phase region of the Ni–Al–Cr system. *Scripta Materialia* **58**, 57–60 (2008).

71. Lee, W. Y., Wright, I. G., Pint, B. a., Zhang, Y. & Liaw, P. K. Effects of sulfur impurity on the scale adhesion behavior of a desulfurized Ni-based superalloy aluminized by chemical vapor deposition. *Metallurgical and Materials Transactions A* **29**, 833–841 (1998).

72. Tu, D. C. & Seigle, L. L. Kinetics of Formation and Microstructure of Aluminide Coatings on Ni-Cr Alloys. *Thin Solid Films* **95**, 47–56 (1982).

73. Wei, H., Hou, G., Sun, X., Guan, H. & Hu, Z. Diffusion mobilities for the B2-b.c.c. phase in the Ni–Al binary system. *Journal of Alloys and Compounds* **454**, 400–405 (2008).

74. Rack, P. D., Fowlkes, J. D. & Deng, Y. Combinatorial RF Magnetron Sputtering for Rapid Materials Discovery: Methodology and Applications. *Microscopy and Microanalysis* **10**, 58–59 (2004).

APPENDIX A

MASS SPECTROSCOPY DATA

Table 11: Data from Second Trial of ICP-MS Experiments

700°C	Parts Per Million (ppm)			
Sample	Al	Cr	Ni	Si
Ni+Al	221	20	43	15
Ni+Cr	5	3610	67	8
ARNi	3	19	70	20
Ni+Si	2	10	107	207

700°C+SO_2	Parts Per Million (ppm)			
Sample	Al	Cr	Ni	Si
Ni+Al	38	10	7	3
Ni+Cr	1	2350	42	11
ARNi	72	401	4450	1890
Ni+Si	4	16	82	86

900°C	Parts Per Million (ppm)			
Sample	Al	Cr	Ni	Si
Ni+Al	6250	265	752000	473
Ni+Cr	923	5040	653000	413
ARNi	865	278	775000	484
Ni+Si	538	1170	49000	3950

Table 12: Data from Third Trial of ICP-MS Experiments

700°C	Parts Per Million (ppm)			
Sample	Al	Cr	Ni	Si
Ni+Al	110	15	17	9
Ni+Cr	0	1600	99	6
ARNi	1	25	50	4
Ni+Si	2	10	107	207

700°C+SO_2	Parts Per Million (ppm)			
Sample	Al	Cr	Ni	Si
Ni+Al	47	22	53	3
Ni+Cr	0	3430	78	1
ARNi	1	56	9	3
Ni+Si	1	15	958	232

900°C	Parts Per Million (ppm)			
Sample	Al	Cr	Ni	Si
Ni+Al	6090	562	738000	487
Ni+Cr	961	7160	735000	400
ARNi	1370	451	1250000	749
Ni+Si	792	1470	600000	9050